LIÈGE université Library

https://lib.uliege.be https://matheo.uliege.be

Mémoire

Auteur : Bouchez, Robin
Promoteur(s) : 32371; Matagne, André
Faculté : Faculté des Sciences
Diplôme : Master en biochimie et biologie moléculaire et cellulaire, à finalité approfondie
Année académique : 2025-2026
URI/URL : http://hdl.handle.net/2268.2/26937

Avertissement à l'attention des usagers :

Tous les documents placés en accès ouvert sur le site le site MatheO sont protégés par le droit d'auteur. Conformément aux principes énoncés par la "Budapest Open Access Initiative"(BOAI, 2002), l'utilisateur du site peut lire, télécharger, copier, transmettre, imprimer, chercher ou faire un lien vers le texte intégral de ces documents, les disséquer pour les indexer, s'en servir de données pour un logiciel, ou s'en servir à toute autre fin légale (ou prévue par la réglementation relative au droit d'auteur). Toute utilisation du document à des fins commerciales est strictement interdite.

Par ailleurs, l'utilisateur s'engage à respecter les droits moraux de l'auteur, principalement le droit à l'intégrité de l'oeuvre et le droit de paternité et ce dans toute utilisation que l'utilisateur entreprend. Ainsi, à titre d'exemple, lorsqu'il reproduira un document par extrait ou dans son intégralité, l'utilisateur citera de manière complète les sources telles que mentionnées ci-dessus. Toute utilisation non explicitement autorisée ci-avant (telle que par exemple, la modification du document ou son résumé) nécessite l'autorisation préalable et expresse des auteurs ou de leurs ayants droit.

KU LEUVEN

LIÈGE université

Department of Life Sciences

Faculty of Sciences – University of Liege

Can Molecular Partners Reshape Amyloid Assembly?

A Reductionist Investigation of the Influence of a TRA2B-Derived Peptide on tau(297-391) Amyloid Fibrils

Robin Bouchez

MSc. BBMC

Academic year: 2025-2026

Thesis submitted in partial fulfillment of the requirements for the degree of Master in

Biochemistry, Molecular and Cellular Biology, Advanced Track

Host laboratory: Switch Lab – VIB-KU Leuven

Supervisor: Rodrigo GALLARDO

Co-promotor: André MATAGNE

Committee: Mireille DUMOULIN, Moreno GALLENI, Arnaud VANDEN BROECK

Acknowledgments:

I would first like to thank everyone at the Switch Laboratory for welcoming me and providing an excellent environment in which to carry out this project. The scientific expertise, resources, and working conditions available within the laboratory were essential to the development of this work. In particular, I would like to thank Joost Schymkowitz and Frederic Rousseau for giving me the opportunity to complete my Master's thesis at SwitchLab, as well as Hannah Wilkinson for her help and support throughout my time in the laboratory. I would also like to acknowledge André Matagne, my co-promotor at the University of Liège, for his academic role in this master's thesis.

I am particularly grateful to Rodrigo Gallardo, who supervised me throughout this project. His guidance was invaluable both in the laboratory and during the preparation of this thesis. He supported me in planning and interpreting experiments, helped me work through experimental difficulties, and always took the time to provide advice, explanations, and alternative perspectives. I am also very thankful for his careful feedback on my written work, which helped me improve the clarity, structure, and scientific precision of this thesis. His support throughout the project allowed me to progressively gain independence in the laboratory and develop a more critical approach to experimental research.

I would also like to thank all the members of SwitchLab for their availability, kindness, and willingness to share their knowledge. From the beginning of my internship, I was fortunate to work in an environment where people were always willing to answer questions, explain their work, discuss experimental problems, or provide advice when needed. I am especially grateful to those who took the time to guide me through unfamiliar techniques and accompany me during experiments while I was learning the different methods used throughout this project.

I would also like to thank my friends from the master's program**,** Alex, Aveline, Laura, Maeva, and Remi, for their friendship and support throughout these years. Sharing the different moments of the master's program, both the difficult ones and the more enjoyable ones, made the whole experience much easier and more memorable.

I would like to thank my family, and especially my parents, for their constant support throughout my studies. They have always encouraged me, including during the more difficult periods, and provided me with the stability and conditions that allowed me to pursue my studies and reach this stage. Their support has been an important part of this journey.

Finally, I would like to thank Perrine, who has been by my side throughout much of this journey. We shared many hours of studying, as well as the stressful periods and important moments that came with it. She has always supported me, encouraged me, and believed in me throughout these years. She also helped me maintain some balance during the busiest periods by making sure that work did not completely take over and that I occasionally took the breaks I needed.

I am grateful to everyone who contributed, in one way or another, to this project and to the years of study that led to it.

Table of Contents

1. Introduction ..... - 1 -

1.1. From neurodegenerative disease to molecular pathology ..... - 1 -

1.2. From soluble proteins to amyloid assemblies: molecular mechanisms of aggregation ..... - 1 -

1.3. Amyloid fibril architecture and structural polymorphism ..... - 4 -

1.4. Tau: from physiological protein to Alzheimer's disease amyloid ..... - 6 -

1.5. Beyond Tau: associated proteins with patient-derived Tau assemblies ..... - 9 -

1.6. TRA2B as a candidate modulator of Tau pathology ..... - 10 -

1.7. Reductionist strategy to test the TRA2B / Tau interaction ..... - 11 -

2. Objectives of the project ..... - 13 -

3. Materials and Methods ..... - 14 -

3.1. Expression and Purification of tau(297-391) ..... - 14 -

3.1.1. Tau(297-391) construct and properties ..... - 14 -

3.1.2. Protein Expression ..... - 14 -

3.1.3. Cell Lysis ..... - 15 -

3.1.4. Nickel Affinity Chromatography (IMAC) ..... - 15 -

3.1.5. 6×His–SUMO Tag Cleavage and Dialysis ..... - 16 -

3.1.6. Reverse-Phase HPLC Purification ..... - 16 -

3.1.7. SDS-PAGE analysis of protein expression and purification ..... - 16 -

3.1.8. Protein identity, quality control, and storage ..... - 17 -

3.2. P12 Peptide Preparation and handling ..... - 17 -

3.2.1. Preparation of tau(297-391) aggregation mixtures and buffer exchange ..... - 17 -

3.2.2. Solid-phase peptide synthesis (SPPS) ..... - 18 -

3.3. Biophysical characterization ..... - 19 -

3.3.1. Liquid Chromatography–Mass Spectrometry ..... - 19 -

3.3.2. Thioflavin T assay ..... - 19 -

3.3.3. Sedimentation assay ..... - 19 -

3.3.4. Preparation of tau(297-391) fibril seeds ..... - 20 -

3.4. Electron microscopy ..... - 20 -

3.4.1. Negative-stain TEM ..... - 20 -

3.4.2. Morphometric analysis and classification of PHF-like fibrils ..... - 21 -

3.4.3. Dual-size nanogold labeling ..... - 21 -

3.4.4. Cryo-EM grid preparation and vitrification ..... - 22 -

3.4.5. Cryo-EM grid screening ..... - 22 -

4. Results ..... - 23 -

4.1. Recombinant production and validation of tau(297-391) ..... - 23 -

4.1.1. Recombinant expression of His-SUMO-tau(297-391) ..... - 23 -

4.1.2. Purification and validation of tag-free tau(297-391) ..... - 23 -

4.2. Establishment of initial aggregation conditions for tau(297-391)/P12 system ..... - 27 -

4.2.1. ThT-based screening of aggregation conditions ..... - 27 -

4.2.2. Tau(297-391) and P12 solubility across the pH 7.4 screening conditions ..... - 28 -

4.3. P12 modulates tau(297-391) aggregation kinetics in NaCl conditions ..... - 29 -

4.3.1. P12 concentration reshapes tau(297-391)-associated ThT kinetics ..... - 29 -

4.3.2. Preformed P12 assemblies promote tau(297-391) aggregation ..... - 31 -

4.4. TEM reveals fibrillar assemblies with limited suitability for further structural investigation - 32 -

4.4.1. Morphological characterization of NaCl-derived fibrils ..... - 32 -

4.4.2. Published $MgCl_2$-based PHF-like conditions initially fail in the current system ..... - 34 -

4.5. Buffer chemistry explains and resolves the failure to generate PHF-like fibrils ..... - 35 -

4.5.1. Phosphate/$MgCl_2$ incompatibility alters the aggregation environment ..... - 35 -

4.5.2. Buffer optimization restores PHF-like Tau fibril morphology ..... - 36 -

4.6. Optimized $MgCl_2$ conditions provide a PHF-like context for reassessing P12 effects ..... - 37 -

4.6.1. Stepwise adaptation of the optimized conditions to lower tau(297–391) concentration ..... - 37 -

4.6.2. Generation and TEM validation of fibril-derived tau(297-391) seeds ..... - 39 -

4.6.3. P12 alters tau(297-391) aggregation kinetics under optimized $MgCl_2$ conditions in a concentration-dependent manner. - 39 -

4.6.4. Morphological heterogeneity of tau(297-391), P12, and tau(297-391)–P12 assemblies under optimized $MgCl_2$ conditions - 41 -

4.7. Preliminary cryo-EM evaluation of tau(297-391) and tau(297-391)–P12 fibrillar samples - 43 -

4.7.1. Screening of grid supports and vitrification parameters using tau(297-391) fibrils - 43 -

4.7.2. Identification of a tau(297-391)–P12 grid suitable for future data collection - 45 -

4.8. Development of a dual-size nanogold strategy to investigate tau(297-391)–P12 spatial organization within fibrillar assemblies - 46 -

4.8.1. Synthesis and functional validation of biotinylated P12 derivatives - 46 -

4.8.2. Optimization of nanogold labeling for spatial analysis of tau(297-391)–P12-derived peptide fibrillar assemblies - 48 -

5. Discussion - 50 -

5.1. P12 is a condition-dependent modulator of tau(297-391) assembly - 50 -

5.2. The assembly state of P12 may contribute to promotion of tau(297-391) aggregation - 52 -

5.3. P12 associates with fibrillar material, but its molecular location remains unresolved - 52 -

5.4. The reaction environment shapes tau(297-391) fibril morphology and the manifestation of the P12 effect - 54 -

5.5. A working mechanistic model for the tau(297-391) –P12 interaction - 55 -

5.6. Biological relevance and limitations of the reductionist tau(297-391)/P12 system - 57 -

5.7. Future directions: discriminating between the remaining mechanistic models - 58 -

5.8. General conclusion - 59 -

6. Artificial intelligence tools utilization declaration - 61 -

7. Bibliography - 62 -

8. Supplementary Information - 67 -

8.1. Supplementary Figures - 67 -

8.2. Supplementary Tables - 75 -

8.3. Supplementary Notes - 78 -

Summary

Thesis title : **Can Molecular Partners Reshape Amyloid Assembly? A Reductionist Investigation of the Influence of a TRA2B-Derived Peptide on tau(297–391) Amyloid Fibrils**

Student : Robin Bouchez

Academic year: 2025–2026

Host laboratory : SwitchLab, VIB–KU Leuven

Supervisor : Rodrigo Gallardo

Co-promotor : André Matagne



Tau protein aggregation into amyloid fibrils is a major feature of Alzheimer's disease. This process can be influenced by the molecular environment of Tau, including interactions with other proteins. Previous work from SwitchLab using a cell-based screening assay identified TRA2B as a potential modulator of Tau aggregation and showed that P12, a TRA2B-derived peptide, can influence this process.

This study aimed to characterize the effects of P12 on the assembly of the tau(297–391) fragment using a reductionist *in vitro* system combining kinetic, biochemical, and microscopic analyses. P12 modified the aggregation profiles of tau(297–391)-containing reactions under different experimental conditions, while preformed P12 assemblies also promoted thioflavin T-positive responses in the presence of tau(297–391). Both tau(297–391) and P12 were simultaneously depleted from the soluble fraction, consistent with their partitioning into sedimentable material. Following optimization of the aggregation conditions, tau(297–391) fibrils displaying a twisted morphology resembling that of Tau filaments observed in Alzheimer's disease were obtained. Co-incubation with P12 was associated with a different distribution of fibrillar morphologies compared with the individual controls, while nanogold labeling provided preliminary indications of P12 association with fibrillar material.

Taken together, these results indicate that P12 can modulate the aggregation behavior and fibrillar morphology of tau(297–391). However, they do not establish whether P12 is incorporated into the same fibrils as tau(297–391) or directly alters the underlying tau(297–391) fold.

Keywords: Tau, tau(297–391), TRA2B, P12, amyloid fibrils, heterotypic interactions, amyloid polymorphism, paired helical filaments, Alzheimer's disease.

Résumé

Titre du mémoire : **Can Molecular Partners Reshape Amyloid Assembly? A Reductionist Investigation of the Influence of a TRA2B-Derived Peptide on tau(297–391) Amyloid Fibrils**
Étudiant : Robin Bouchez
Année académique : 2025–2026
Laboratoire d'accueil : SwitchLab, VIB–KU Leuven
Superviseur : Rodrigo Gallardo
Co-promoteur : André Matagne

L'agrégation de la protéine Tau en fibrilles amyloïdes constitue une caractéristique majeure de la maladie d'Alzheimer. Ce processus peut être influencé par l'environnement moléculaire de Tau, notamment par ses interactions avec d'autres protéines. Des travaux antérieurs du SwitchLab, utilisant un test de criblage cellulaire, ont identifié TRA2B comme un modulateur potentiel de l'agrégation de Tau et montré que P12, un peptide dérivé de TRA2B, peut influencer ce processus.

Cette étude visait à caractériser les effets de P12 sur l'assemblage du fragment tau(297–391) à l'aide d'un système réductionniste *in vitro* combinant des analyses cinétiques, biochimiques et microscopiques. P12 a modifié les profils d'agrégation des réactions contenant tau(297–391) dans différentes conditions expérimentales, tandis que des assemblages préformés de P12 ont également favorisé des réponses positives à la thioflavine T en présence de tau(297–391). Les quantités de tau(297–391) et de P12 ont diminué simultanément dans la fraction soluble, ce qui est compatible avec leur transfert vers une fraction sédimentable. Après optimization des conditions d'agrégation, des fibrilles de tau(297–391) présentant une morphologie torsadée semblable à celle des filaments de Tau observés dans la maladie d'Alzheimer ont été obtenues. La co-incubation avec P12 a été associée à une distribution différente des morphologies fibrillaires par rapport aux contrôles individuels, tandis que le marquage aux nanoparticules d'or a fourni des indications préliminaires d'une association entre P12 et le matériel fibrillaire.

Dans leur ensemble, ces résultats indiquent que P12 peut moduler le comportement d'agrégation et la morphologie fibrillaire de tau(297–391). Ils ne permettent toutefois pas d'établir si P12 est incorporé dans les mêmes fibrilles que tau(297–391) ou s'il modifie directement le repliement sous-jacent de tau(297–391).

Mots-clés : Tau, tau(297–391), TRA2B, P12, fibrilles amyloïdes, interactions hétérotypiques, polymorphisme amyloïde, filaments hélicoïdaux appariés, maladie d'Alzheimer.

Abbreviation List

2N4R : Tau isoform containing two N-terminal inserts and four microtubule-binding repeats

6×His–SUMO–tau(297–391) : Recombinant fusion protein comprising a hexahistidine tag, a SUMO tag, and the tau(297–391) fragment

a.u. : Arbitrary units

AD : Alzheimer’s disease

AI : Artificial intelligence

APR : Aggregation-prone region

APR1 : First TRA2B aggregation-prone region, comprising residues 137–142 and the sequence VFSKYG

APR2 : Second TRA2B aggregation-prone region, comprising residues 147–152 and the sequence VSIVYD

BL21(DE3) : *Escherichia coli* strain used for recombinant protein expression

BSA : Bovine serum albumin

C18 : Octadecyl-bonded stationary phase used for reversed-phase chromatography

C-ter : C-terminus

cryo-EM : Cryo-electron microscopy

CV : Column volume

Cy3 : Cyanine 3 fluorescent dye

Cys322 : Cysteine residue at position 322 of Tau

Da : Dalton

DCM : Dichloromethane

dGAE : Alternative designation for the tau(297–391) fragment

DMF : N,N-Dimethylformamide

DNase : Deoxyribonuclease

DTT : Dithiothreitol

eCFP : Enhanced cyan fluorescent protein

EDTA : Ethylenediaminetetraacetic acid

EM : Electron microscopy

ESI : Electrospray ionization

ExPASy : Expert Protein Analysis System

eYFP : Enhanced yellow fluorescent protein

FL : Full-length

Fmoc : 9-Fluorenylmethoxycarbonyl

Fmoc-AA-OH : Fmoc-protected amino acid bearing a free carboxyl group

FRET : Förster resonance energy transfer

HATU : O-(7-Azabenzotriazol-1-yl)-N,N,N′,N′-tetramethyluronium hexafluorophosphate

HBTU : O-(Benzotriazol-1-yl)-N,N,N′,N′-tetramethyluronium hexafluorophosphate

HEPES : 4-(2-Hydroxyethyl)-1-piperazineethanesulfonic acid

HPLC : High-performance liquid chromatography

IMAC : Immobilized metal affinity chromatography

IPTG : Isopropyl β-D-1-thiogalactopyranoside

LC–MS : Liquid chromatography–mass spectrometry

LLPS : Liquid–liquid phase separation

MAPT : Microtubule-associated protein tau gene

$MgCl_2$: Magnesium chloride

MN423 : Monoclonal antibody recognizing the Tau epitope ending at Glu391

mRNA : Messenger ribonucleic acid

MTBE : Methyl tert-butyl ether

N-ter : N-terminus

NFT : Neurofibrillary tangle

NMM : N-Methylmorpholine

P12 : TRA2B-derived peptide spanning residues 133–156 and containing APR1 and APR2

P12-2x Linker PEG_Biotin : P12 derivative designed to contain two PEG2 linkers and a biotin moiety

P12-Biotin : Biotinylated P12 derivative

P12-Linker PEG-Biotin : P12 derivative designed to contain one PEG2 linker and a biotin moiety

P12-XX-Biotin : Biotinylated P12 derivative containing an additional four-residue TRA2B-derived sequence

PAGE : Polyacrylamide gel electrophoresis

PAM4 : Tau aggregation-prone motif located in repeat R4, comprising residues 350–362 and the sequence VQSKIGSLDNITH

PB : Phosphate buffer

PBS : Phosphate-buffered saline

PEG2 : Polyethylene glycol linker containing two ethylene glycol units

pET-24(+) : Bacterial expression vector used for recombinant protein production

PHF : Paired helical filament

PHF-like : Fibrillar morphology resembling that of paired helical filaments

PHF6 : Tau amyloidogenic hexapeptide motif located in repeat R3, comprising residues 306–311 and the sequence VQIVYK

PHF6* : Tau amyloidogenic hexapeptide motif located in repeat R2, comprising residues 275–280 and the sequence VQIINK

PMSF : Phenylmethylsulfonyl fluoride

ProtParam : ExPASy tool used to predict protein physicochemical properties

PTM : Post-translational modification

PVDF : Polyvinylidene fluoride

R2/1 : Holey cryo-EM grid support with approximately 2 μm holes and 1 μm spacing

R2/2 : Holey cryo-EM grid support with approximately 2 μm holes and 2 μm spacing

RP-HPLC : Reversed-phase high-performance liquid chromatography

rpm : Revolutions per minute

RRM : RNA recognition motif

SDS–PAGE : Sodium dodecyl sulfate–polyacrylamide gel electrophoresis

SF : Straight filament

SPPS : Solid-phase peptide synthesis

tau(297–391) : Recombinant 95-amino-acid Tau fragment comprising residues 297–391 of the human 2N4R Tau isoform

Tau-FL : Full-length Tau

Tau(Q244–K375) : Tau fragment comprising residues 244–375 used in a cellular FRET biosensor

TBST : Tris-buffered saline containing Tween-20

TCEP : Tris(2-carboxyethyl)phosphine

TEM : Transmission electron microscopy

TFA : Trifluoroacetic acid

ThT : Thioflavin T

TIS : Triisopropylsilane

TRA2B : Transformer-2 protein homolog beta

ULP1 : Ubiquitin-like-specific protease 1, a SUMO-specific protease

v/v : Volume-to-volume ratio

v/v/v : Volume-to-volume-to-volume ratio

W : Wash fraction

w/v : Weight-to-volume ratio

×g : Relative centrifugal force expressed as a multiple of gravitational acceleration

1. Introduction

1.1. From neurodegenerative disease to molecular pathology

Neurodegenerative diseases represent one of the most challenging categories of human disorders because they progressively compromise the function and survival of neurons, leading to irreversible alterations in cognition, movement, autonomy, and quality of life. Disorders such as Alzheimer's disease, Parkinson's disease, amyotrophic lateral sclerosis, and related conditions affect not only individual patients, but also families, caregivers, and healthcare systems. Despite major advances in clinical diagnosis and symptomatic management, curative or broadly effective disease-modifying strategies remain limited for many of these disorders, in part because the molecular events that initiate and drive neurodegeneration are still incompletely understood. [1; 2]

A central challenge in neurodegenerative disease research is to connect pathological changes observed in patient brains with the molecular mechanisms that produce them. Protein aggregation is not inherently pathological, as certain protein assemblies, including functional amyloids, participate in physiological processes in diverse organisms [3; 4]. However, in several of the disorders mentioned above, the accumulation of misfolded or aggregated proteins in affected regions of the nervous system represents a prominent pathological feature. Although protein aggregation represents only one of several processes associated with neurodegeneration, these assemblies may contribute to disease progression rather than merely serve as passive histological markers. Their precise contribution may depend on the disease context, the proteins involved, and their interactions with the cellular environment. Understanding how proteins convert from soluble states into pathological assemblies may therefore help identify molecular mechanisms involved in aggregation-associated neurodegenerative disorders.[5]

This master's thesis addresses this question through the study of Tau, a protein that accumulates abnormally in Alzheimer's disease and other neurodegenerative conditions collectively known as tauopathies. More specifically, it investigates whether interaction with molecular partners can influence the aggregation of Tau and modify the properties of the assemblies that are formed. The following sections first introduce the general principles of protein aggregation before progressively focusing on Tau and the molecular system investigated in this work.

1.2. From soluble proteins to amyloid assemblies: molecular mechanisms of aggregation

Proteins are often introduced through the classical structure–function paradigm, in which a defined amino acid sequence folds into a native three-dimensional conformation that supports biological function. For many globular proteins, this native state can be viewed, from a thermodynamic perspective, as a dominant accessible minimum within a broader conformational energy landscape [6]. However, this view does not apply uniformly to all proteins. Intrinsically disordered proteins do not adopt a single stable tertiary structure under physiological conditions but instead populate broad and dynamic conformational ensembles [7]. This structural plasticity allows proteins to sample alternative conformations that can expose or shield specific regions, thereby modulating their molecular interactions [8].

These conformational fluctuations can have important consequences for protein folding and aggregation [9]. In particular, partially folded conformations can act as aggregation-prone intermediates and associate through specific intermolecular interactions [10]. This can shift the balance away from isolated monomeric states and promote the formation of larger assemblies through self-association or interactions with other proteins, biomolecules, or surfaces [11]. Depending on protein sequence, molecular environment, and the balance between competing interactions, aggregation can generate a broad range of species, from disordered or amorphous aggregates to more organized supramolecular assemblies [5; 10; 12].

Among these possible outcomes, amyloid fibrils represent a particularly ordered class of protein aggregates. They consist of elongated supramolecular assemblies enriched in β-sheet architecture and stabilized by repetitive intermolecular interactions. In contrast to amorphous aggregates, amyloid fibrils display a high degree of structural organization in which compatible polypeptide conformations stack repetitively along the fibril axis. This organization is schematically illustrated in Figure 1 [13; 14].

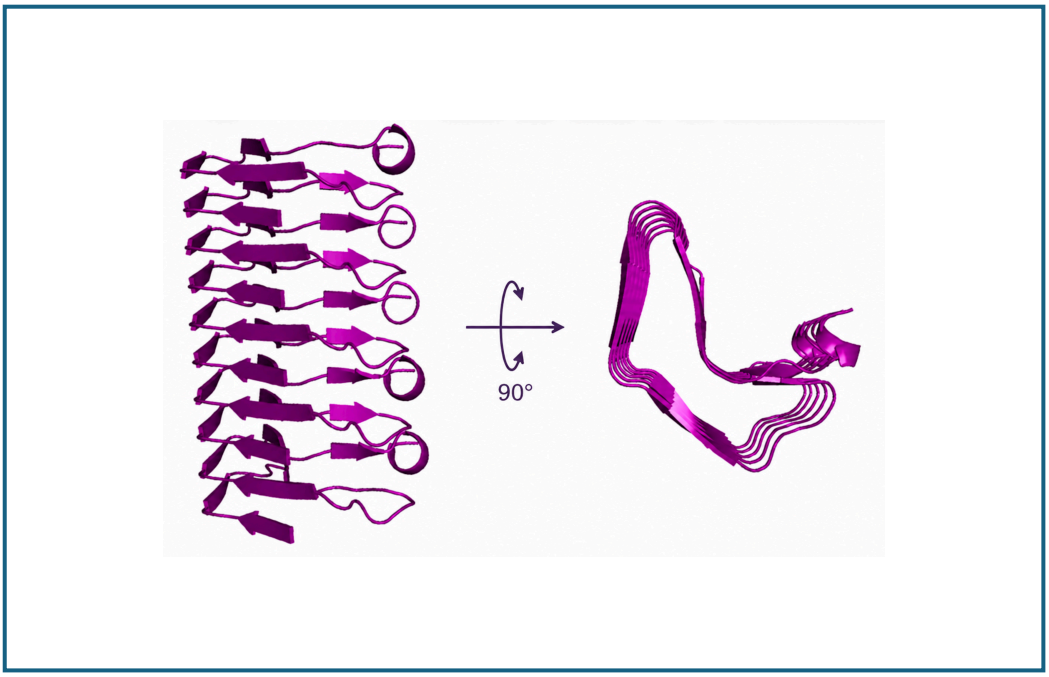


Figure 1. Schematic representation of the same amyloid fibril architecture viewed from two orientations approximately 90° apart.

A key determinant of a protein's amyloid aggregation propensity is the presence of aggregation-prone regions (APRs) within its amino acid sequence [15]. APRs are short sequence segments whose local physicochemical properties favor amyloid-like intermolecular association when they become structurally accessible [16]. They are commonly characterized by sequence features that favor β-sheet formation and intermolecular association, including hydrophobic or aromatic residues and a relative depletion of charged amino acids or residues such as proline that disrupt β-sheet formation. The presence of these residues in the immediate vicinity of APR regions often disrupts β-sheet formation and reduces aggregation propensity by limiting the intermolecular contacts required for amyloid assembly [17], and therefore such residues are often referred to as aggregation gatekeepers. Importantly, the presence of an APR is not sufficient to drive aggregation, as these regions may remain buried, constrained by intramolecular contacts, or protected by their surrounding sequence. Their exposure can arise from intrinsic conformational fluctuations, including partial

unfolding, or from perturbations that reshape the protein conformational ensemble, such as post-translational modification (PTMs), changes in the physicochemical environment, or other factors affecting protein dynamics. Once exposed, these regions can interact with molecular partners and potentially promote aggregation through hydrogen bonding, hydrophobic interactions, steric complementarity, and electrostatic effects [15; 18].

Amyloid formation generally proceeds through a multistep assembly process involving transient intermediate species before the emergence of mature fibrils, as schematically illustrated in Figure 2. Many amyloidogenic proteins aggregate through nucleation-dependent mechanisms, in which the formation of early growth-competent nuclei represents a major kinetic barrier. At the macroscopic level, this process is often associated with a lag phase, although this phase may reflect the combined contribution of several microscopic steps rather than nucleus formation alone. Once growth-competent nuclei or fibril ends are available, elongation proceeds through the templated addition of soluble monomers to fibril ends. Additional amplification mechanisms can further accelerate amyloid formation. Fragmentation generates new fibril ends that support further elongation, whereas secondary nucleation occurs when the surface of pre-existing fibrils catalyzes the formation of new nuclei from soluble monomers. Together, these processes increase the number of aggregation-competent assemblies and can generate complex kinetic profiles [19].

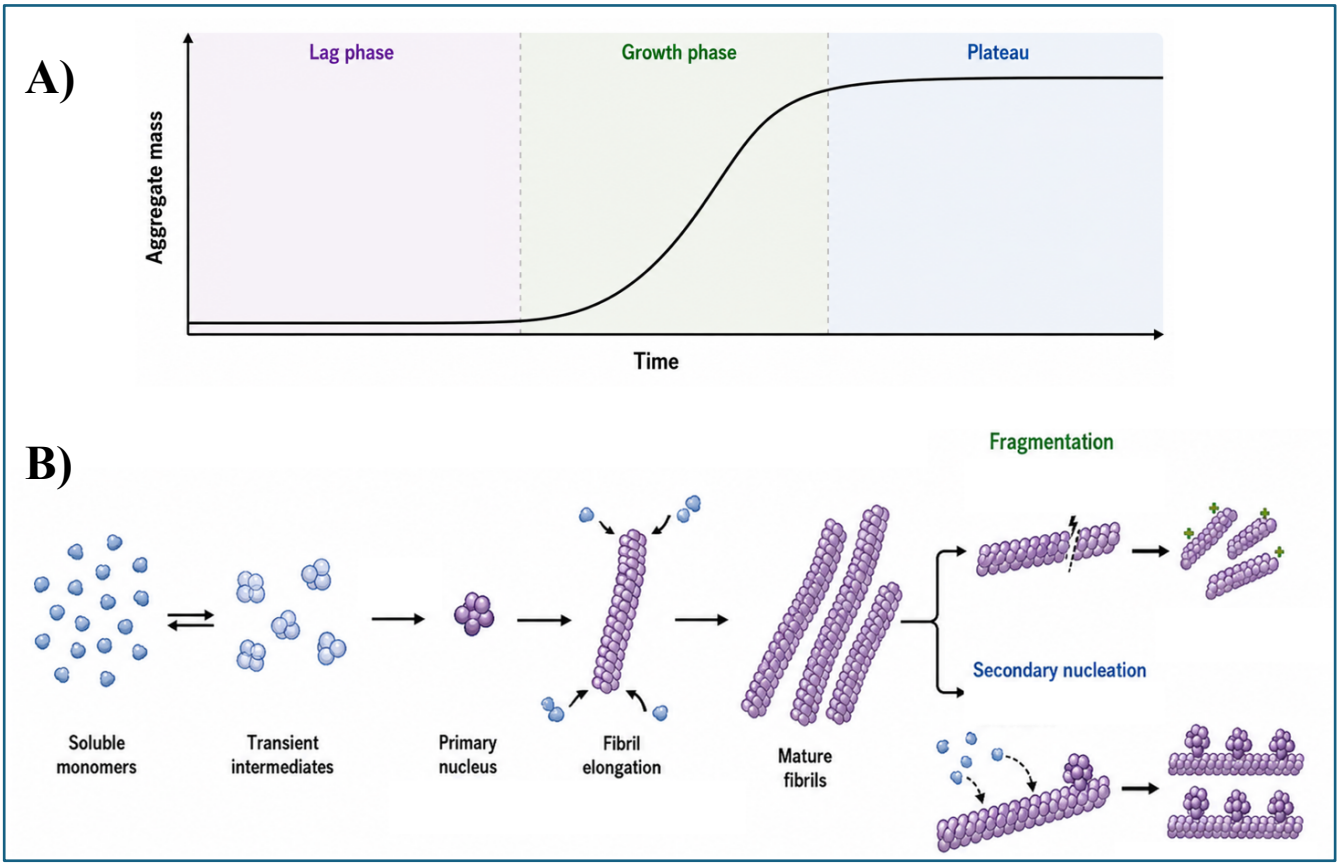


Figure 2. Schematic representation of amyloid aggregation kinetics and underlying mechanisms. A) The sigmoidal curve comprises a lag phase, during which transient intermediates and primary nuclei form, followed by a growth phase driven by fibril elongation and a plateau phase, stabilized as the pool of aggregation-competent monomers becomes depleted. **B)** Schematic representation of the main microscopic processes underlying amyloid fibril formation. Soluble monomers assemble through transient intermediates and primary nucleation, followed by fibril elongation. Mature fibrils can further amplify aggregation through fragmentation and surface-catalysed secondary nucleation.

The ability to form amyloid is not restricted to a small group of pathological proteins but reflects a broader conformational potential of polypeptide chains under permissive conditions [13]. However, the pathological relevance of amyloid formation extends far beyond Tau and the nervous system. Structurally unrelated proteins can undergo analogous transitions toward highly ordered amyloid assemblies, yet their deposition occurs in distinct cellular compartments and tissues and is associated with markedly different clinical outcomes. For example, α-synuclein and huntingtin form pathological assemblies in neurodegenerative disorders, whereas amyloid deposition involving islet amyloid polypeptide, immunoglobulin light chains, or transthyretin occurs in pancreatic, systemic, or organ-specific contexts. Thus, amyloid formation represents a common molecular endpoint that can arise from diverse protein sequences and underlie a broad spectrum of diseases [12; 13].

Whether and how this intrinsic aggregation propensity is expressed depends strongly on the surrounding physicochemical and molecular environment. Parameters such as pH, ionic strength, temperature, protein concentration, redox state, and mechanical stress such as shear force or agitation can alter protein stability, intermolecular interactions, and aggregation kinetics. In biological systems, additional complexity arises from macromolecular crowding, biological interfaces, and biomolecular condensates formed through liquid–liquid phase separation (LLPS). By locally concentrating proteins and other biomolecules within dynamic membrane-free compartments, LLPS can modify intermolecular interactions and potentially influence aggregation pathways [11; 20; 21].

In living systems, protein homeostasis, or proteostasis, is maintained by coordinated networks of molecular chaperones, degradation pathways, and cellular quality-control mechanisms that limit the accumulation of misfolded and aggregation-prone protein species [22]. These protective systems can decline during aging or become impaired in disease, favoring the persistence of aggregated proteins.

Overall, protein aggregation emerges as a dynamic and environmentally sensitive self-assembly process shaped by protein sequence, conformational dynamics, and molecular context. Understanding how these factors collectively influence aggregation pathways is essential for elucidating the molecular basis of amyloid-related diseases.

1.3. Amyloid fibril architecture and structural polymorphism

At the molecular level, amyloid fibrils share a conserved structural organization known as the cross-β architecture. In this architecture, individual β-strands are oriented approximately perpendicular to the fibril axis and assemble into extended β-sheets that run along the direction of fibril growth [23]. The repetitive alignment of peptide backbones generates an extensive network of intermolecular hydrogen bonds, providing a common structural framework for amyloid fibrils formed by otherwise unrelated protein sequences [24].

Within this cross-β framework, fibrils are organized into structural subunits known as protofilaments. These protofilaments are formed by the repetitive stacking of protein or peptide subunits adopting compatible β-sheet-rich conformations. Depending on the amyloid system, mature fibrils may consist of a single protofilament or of several protofilaments associated through complementary intermolecular interfaces. Differences in protofilament number,

orientation, and packing can therefore generate distinct fibrillar morphologies, including thin filaments, twisted ribbons, and more complex helical assemblies [25].

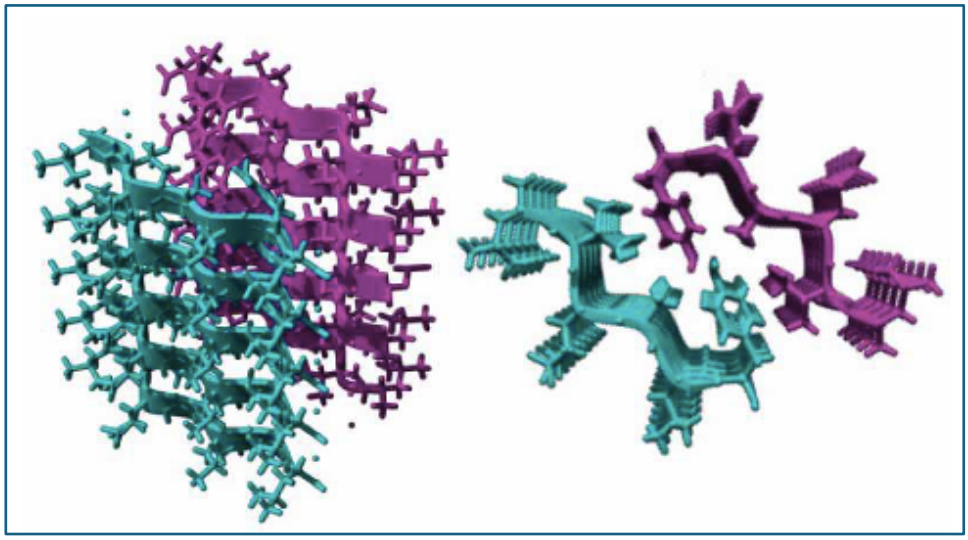


Figure 3. Schematic representation of the same steric-zipper-like interface viewed from two orientations approximately 90° apart. Side chains from the opposing β-sheets interdigitate to form a tightly packed interface. Reproduced from the VIB–KU Leuven SwitchLab website https://switchlab.org/aprs.

A recurring structural feature contributing to amyloid stability is the close packing of opposing β-sheets, in which side chains from facing sheets interdigitate to form densely packed and largely dehydrated interfaces, as schematically illustrated in Figure 3. These highly complementary regions are generally referred to as steric zippers. The close packing and exclusion of water contribute to the stability of the fibril core. Importantly, relatively small changes in side-chain packing, β-sheet registry, or interface geometry can substantially modify fibril architecture and stability [26; 27].

Despite this shared cross-β framework, amyloid formation does not necessarily converge toward a unique final structure. A single protein sequence can generate several structurally distinct fibrillar conformations, known as amyloid polymorphs. These polymorphs arise when the same precursor sequence adopts alternative folds or packing arrangements within the fibril. Consequently, fibrils formed by identical protein molecules can differ in the conformation of their constituent subunits, protofilament organization, intermolecular interfaces, and overall morphology [28].

Structural polymorphism can also be accompanied by differences in biochemical and biological properties. Distinct fibril architectures will most likely differ in molecular surface, and thereby may differ in their seeding activity, mechanical stability, proteolytic resistance, cellular propagation, or cytotoxic effects. These observations underpin the “strain” concept in amyloids, in which structurally distinct fibrils can propagate particular conformational states and, in some systems, be associated with distinct biological phenotypes [28; 29]. Thus, polymorphism is not merely a morphological property but may influence how amyloid assemblies behave and interact with their biological environment. Polymorph selection may begin during the earliest stages of amyloid assembly. During nucleation, transient oligomeric or prefibrillar species can sample alternative conformations, and the emergence of a particular growth-competent nucleus may bias the architecture of the resulting fibril population. During elongation, soluble monomers are recruited onto growing fibril ends and adopt conformations compatible with the pre-existing assembly.

This templated growth can preserve structural features selected during nucleation. Fibrils can subsequently act as seeds by providing pre-existing templates for further monomer recruitment, thereby favoring the continued propagation of the same fibrillar conformation [28; 30].

As introduced in the previous section, amyloid assembly is strongly influenced by its molecular environment. Importantly, these conditions can affect not only whether and how rapidly aggregation occurs, but also which fibrillar architecture is selected. Changes in physicochemical conditions or interactions with cofactors, membranes, nucleic acids, metal ions, and other biomolecules can alter the relative stability of competing nuclei and fibrillar states, thereby favoring particular polymorphs [28; 31]. Amyloid polymorphism therefore reflects an interplay between sequence-encoded structural propensities and the molecular context in which assembly occurs.

Advances in cryo-electron microscopy (cryo-EM) and solid-state nuclear magnetic resonance have enabled amyloid structures to be resolved at near-atomic or atomic resolution. For fibrillar assemblies, cryo-EM structure determination commonly exploits their repetitive helical organization by combining information from multiple overlapping segments along the fibril axis through helical reconstruction. These approaches have revealed substantial structural diversity among fibrils formed by the same protein and have demonstrated that distinct polymorphs occur both *in vitro* and in patient-derived material [28; 29]. In several amyloid diseases, particular fibril architectures are recurrently associated with specific pathological contexts, supporting the concept of disease-associated amyloid folds while avoiding the assumption that fibril structure alone determines disease phenotype [29].

Finally, the structural organization of an amyloid fibril is not necessarily restricted to its ordered core. In many systems, only part of the protein sequence participates in the rigid cross-β structure, whereas flanking regions remain flexible and solvent-exposed. These dynamic peripheral regions are commonly referred to as the “fuzzy coat” [32]. This distinction between an ordered amyloid core and more mobile external regions is particularly relevant for intrinsically disordered proteins, for which substantial portions of the sequence can retain conformational flexibility even after fibril formation. This is the case of Tau, whose amyloid core primarily involves the microtubule-binding repeat domain and adjacent sequences, while much of its N- and C- terminal regions remains flexible and solvent-exposed [33].

Taken together, the cross-β architecture provides a common structural framework for amyloid fibrils, while variations in protein fold, protofilament organization, and intermolecular packing generate substantial structural polymorphism. The architecture that emerges reflects both sequence-encoded structural possibilities and the conditions encountered during assembly, and can in turn influence the biochemical and biological properties of the resulting fibrils. This relationship between amyloid structure, molecular environment, and biological behavior is particularly relevant in disease-associated amyloids, where distinct fibrillar architectures can emerge from the same precursor protein.

1.4. Tau: from physiological protein to Alzheimer’s disease amyloid

Among these disease-associated amyloid systems, Tau represents a particularly relevant example because the same protein that normally contributes to neuronal function can undergo pathological assembly into structurally distinct fibrils. Under physiological conditions, Tau is a microtubule-associated protein that contributes to the organization and

regulation of the neuronal cytoskeleton. Although pathological Tau aggregation occurs across a broad spectrum of tauopathies, the present study focuses on Alzheimer's disease (AD). Consequently, the following section emphasizes the transition of Tau from its physiological state to the disease-associated assemblies characteristic of AD. In Alzheimer's disease, Tau progressively accumulates as filamentous assemblies that constitute the principal structural component of neurofibrillary tangles (NFTs), one of the major neuropathological hallmarks of the disease. The regional distribution and burden of Tau pathology are closely associated with neurodegeneration and cognitive impairment, making Tau aggregation a central feature of AD progression [34].

Despite lacking a stable tertiary structure, Tau displays a modular sequence organization. From the N- to the C-terminus, the protein comprises an N-terminal projection domain, a proline-rich region, a microtubule-binding repeat domain, and a short C-terminal region. Alternative splicing generates six major Tau isoforms in the adult human brain, which differ in the number of N-terminal inserts and in the presence of either three or four microtubule-binding repeats. Inclusion of exon 10 introduces the second repeat, R2, thereby distinguishing 4R Tau isoforms from 3R isoforms. Tau isoforms are commonly designated according to the number of N-terminal inserts (0N, 1N, or 2N) and microtubule-binding repeats (3R or 4R). Accordingly, 2N4R Tau refers to the isoform containing two N-terminal inserts and all four microtubule-binding repeats (R1–R4). The repeat domain mediates much of Tau's interaction with microtubules but also contains the principal sequence elements involved in amyloid formation [35]. The organization of the six Tau isoforms, together with the position of the tau(297–391) fragment used in this study, is illustrated in Figure 4.

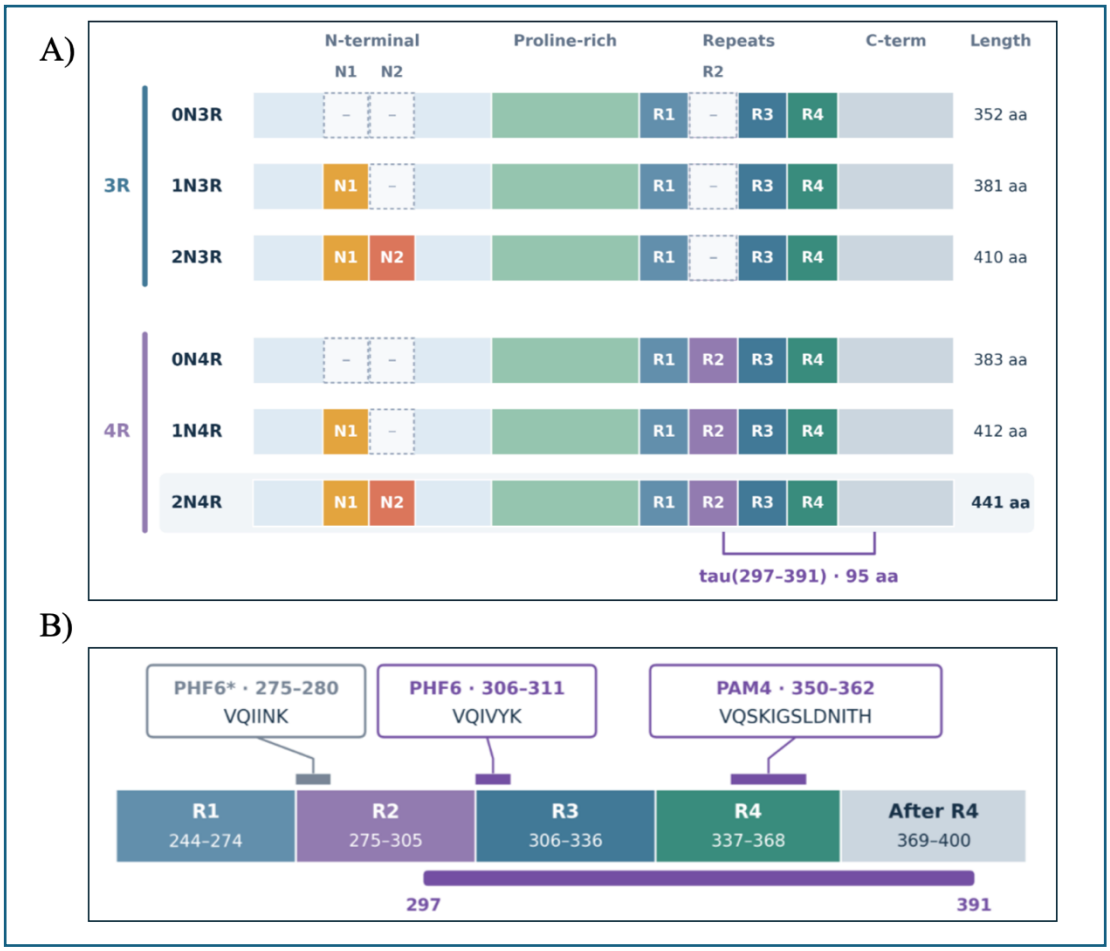


Figure 4. Human Tau isoforms and the tau(297–391) construct. (A) Domain organization of the six adult human brain Tau isoforms. **(B)** Position of tau(297–391) relative to the PHF6*, PHF6, and PAM4 motifs. Residue numbering follows the 2N4R isoform.

As an intrinsically disordered protein, Tau does not maintain these domains in fixed spatial arrangements. Instead, it populates heterogeneous conformational ensembles shaped by transient local structures and long-range intramolecular contacts. Consequently, its amyloidogenic segments are neither permanently buried within a globular core nor continuously accessible to intermolecular interactions. Changes in the conformational ensemble of Tau can increase the accessibility of these regions, thereby facilitating molecular recognition and shifting the protein towards aggregation-competent states [36]. Among the factors capable of reshaping this ensemble, abnormal phosphorylation is particularly relevant in pathological Tau. Specific phosphorylation patterns can alter local conformational preferences and promote states favoring aggregation, providing a potential molecular link between Tau hyperphosphorylation and fibril formation. [37]

The best-characterized amyloidogenic motifs of Tau are located within the microtubule-binding repeat domain. PHF6* (^{275}VQIINK^{280}), located in R2, and PHF6 (^{306}VQIVYK^{311}), located in R3, can adopt β-strand conformations and establish intermolecular β-sheet contacts that promote nucleation and fibril formation. Because PHF6* lies within R2, it is present only in 4R Tau isoforms, whereas PHF6 is shared by both 3R and 4R Tau. A third aggregation-prone region, PAM4 (^{350}VQSKIGSLDNITH^{362}), has more recently been identified within R4 and has been implicated in fibril-core stability and structural polymorphism. Together, these motifs constitute important sequence determinants of Tau assembly, although their contribution depends on their accessibility and on the broader conformational and molecular environment of the protein [38; 39].

Ultrastructural analyses of AD brain tissue identified two major Tau filament morphologies: paired helical filaments (PHFs) and straight filaments (SFs). PHFs are generally the predominant form and display a characteristic periodic twist, whereas SFs appear straighter in projection. The subsequent development of cryo-electron microscopy enabled these filaments to be resolved directly from patient-derived brain material at near-atomic resolution. These studies revealed that AD-derived PHFs and SFs are each composed of two C-shaped protofilaments sharing the same underlying Tau fold but differing in their inter-protofilament interfaces [40].

Comparison with recombinant Tau fibrils generated using conventional heparin-induced protocols showed that such *in vitro* assemblies can differ substantially from patient-derived AD filaments. This discrepancy illustrates the strong influence of aggregation conditions and molecular context on Tau fibril architecture [41]. More broadly, cryo-EM analyses across different tauopathies have identified recurrent disease-associated Tau folds, supporting the view that fibril architecture may contribute to pathological heterogeneity, although structural variation alone is unlikely to account fully for differences in clinical presentation [29].

The identification of disease-associated Tau folds has clarified the architecture of mature fibrils but has not fully resolved the mechanisms governing their formation, propagation, and structural diversification. Tau aggregation occurs within a complex molecular environment in which post-translational modifications, cofactors, and interactions with surrounding biomolecules may influence the assembly pathway. This raises the question of whether components associated with pathological Tau material are merely recruited during disease or can actively influence Tau assembly.

1.5. Beyond Tau: associated proteins with patient-derived Tau assemblies

For many years, neurofibrillary tangles (NFTs) were primarily viewed as deposits composed predominantly of aggregated Tau. This interpretation arose from the observation that Tau constitutes a major structural component of paired helical filaments and straight filaments isolated from Alzheimer's disease brains [42]. However, advances in biochemical fractionation, mass spectrometry-based proteomics, and imaging approaches have progressively revealed that pathological Tau assemblies possess a more complex molecular composition and interactome than initially anticipated [43; 44].

Proteomic analyses of NFTs and Tau-associated pathological material have identified numerous non-Tau proteins, including molecular chaperones, cytoskeletal proteins, components of protein quality-control systems, ribosomal proteins, and proteins involved in RNA metabolism [43; 44]. Among these groups, RNA-binding proteins are of particular interest because they are recurrently detected in Tau-associated material and because many contain intrinsically disordered or low-complexity regions capable of supporting multivalent intermolecular interactions often observed in LLPS [45; 46]. Nevertheless, their presence within pathological material does not, by itself, establish a direct role in Tau aggregation.

The molecular mechanisms underlying the recruitment of proteins identified within the Tau-associated interactome to pathological Tau-containing assemblies remain incompletely understood. Some may become passively sequestered as aggregation progresses, whereas others may be recruited indirectly through interactions with additional components of pathological inclusions. Tau-interactome studies nevertheless suggest that a subset of these proteins may interact more directly with pathological Tau species and potentially influence the aggregation process [43].

These observations support the possibility that pathological Tau assemblies are influenced not only by homotypic interactions between Tau molecules, but also by heterotypic interactions between Tau and distinct molecular partners. Such interactions could stabilize particular conformational states, alter aggregation pathways, or modify fibril architecture. Proteins containing intrinsically disordered regions, low-complexity domains, or aggregation-prone regions are plausible candidates for such effects because these sequence features can facilitate intermolecular association with amyloid-forming regions of Tau [43; 47].

Evidence for sequence-dependent heterotypic recognition has emerged from studies showing that peptides with local similarity to Tau APRs can interact with Tau-derived APR peptides and modify aggregation kinetics and fibril morphology. In cellular models, related interactions can also influence the propagation of aggregation [47]. These findings provide a rationale for moving beyond the descriptive identification of proteins associated with Tau pathology and towards the mechanistic prioritization of candidate modulators. Sequence-based screening approaches can therefore be used to identify proteins containing regions with local similarity to Tau APRs and assess their capacity to alter Tau assembly. Within this framework, Transformer-2 protein homolog beta (TRA2B) emerged as a particularly relevant candidate for investigating sequence-dependent heterotypic interactions with Tau.

1.6. TRA2B as a candidate modulator of Tau pathology

Transformer-2 protein homolog beta (TRA2B) is a serine/arginine-rich RNA-binding protein involved in the regulation of alternative pre-mRNA splicing [48]. Beyond its identification as a potential modulator of Tau aggregation, TRA2B has a pre-existing functional connection to Tau biology through its involvement in the alternative splicing of MAPT exon 10, which regulates the balance between 3R and 4R Tau isoforms [49]. Together with the recurrent detection of RNA-binding proteins in Tau-associated pathological material, this connection made TRA2B a particularly relevant candidate for investigating how molecular partners may influence Tau assembly.

TRA2B was further prioritized through sequence-based screening aimed at identifying proteins containing regions capable of heterotypic recognition with amyloid-forming regions of Tau. This approach was based on the hypothesis that local sequence similarity between aggregation-prone regions could favor specific intermolecular contacts and thereby influence Tau assembly. Within this framework, preliminary work from the SwitchLab identified TRA2B as an enhancer of Tau seeding activity in cellular models, providing functional support for its investigation as a potential modulator of Tau propagation [unpublished data from the SwitchLab].

Analysis of the TRA2B sequence provided a possible molecular basis for this effect. Within its RNA recognition motif (RRM), TRA2B contains two closely positioned aggregation-prone regions. The first, APR1 (^{137}VFSKYG^{142}), displays local sequence similarity to the Tau PHF6 motif (^{306}VQIVYK^{311}), one of the best-characterized amyloid-forming regions of Tau. The second, APR2 (^{147}VSIVYD^{152}), shares local similarity with PAM4 (^{350}VQSKIGSLDNITH^{362}), a Tau segment implicated in fibril-core stability and structural polymorphism. The proximity of these two TRA2B motifs, together with their predicted accessibility, raises the possibility that the TRA2B RRM could engage more than one amyloid-forming region of Tau. [unpublished data from the SwitchLab].

Additional preliminary findings from the host laboratory further support the functional relevance of this sequence-based model. Using a cellular FRET-based Tau biosensor expressing Tau(Q244–K375)-eYFP/eCFP, the laboratory observed that TRA2B enhances Tau seeding activity, with the strongest effects detected for patient-derived Tau preparations exhibiting low baseline seeding activity. Consistent with this cellular phenotype, TRA2B overexpression *in vivo* was also associated with increased accumulation of seeding-competent Tau species. In Alzheimer's disease brain tissue, TRA2B appeared to redistribute from the soluble nuclear pool toward insoluble Tau-associated fractions. Although this redistribution is consistent with an association between TRA2B and Tau-containing pathological material, it does not by itself demonstrate direct co-aggregation or incorporation of TRA2B into the Tau fibril core. Collectively, these observations support a model in which TRA2B may act as a functional modulator or amplifier of Tau aggregation rather than merely serving as a passive marker of pathology [unpublished data from the SwitchLab].

Together, these findings support a working model in which TRA2B may facilitate Tau propagation through interactions involving its aggregation-prone regions, particularly in seeded contexts. However, the molecular nature of this interaction remains unresolved, including whether the proposed APR-mediated recognition can occur directly during Tau fibril assembly.

1.7. Reductionist strategy to test the TRA2B / Tau interaction

To address the unresolved molecular basis of the TRA2B–Tau relationship, a reductionist *in vitro* system was established using tau(297-391) and the TRA2B-derived peptide P12. Cellular and *in vivo* models are essential for establishing the pathological relevance of TRA2B, but they contain numerous factors that may contribute directly or indirectly to the observed phenotype, including compartmentalization, post-translational modifications, cofactors, and additional interaction partners. A simplified reconstituted system therefore provides a controlled framework in which the proposed interaction between Tau and TRA2B-derived aggregation-prone regions can be investigated with reduced molecular complexity.

On the Tau side, this strategy relies on the recombinant fragment tau(297-391), corresponding to a restricted region of the human 2N4R Tau sequence. This fragment retains PHF6 and PAM4, the two amyloid-forming regions of Tau displaying local sequence similarity to the TRA2B aggregation-prone regions described above (APR1 and APR2), while excluding large portions of the flexible N- and C-terminal regions of full-length Tau. Tau(297-391) therefore provides a focused experimental system for studying fibril formation and the influence of heterotypic molecular partners on Tau assembly [38; 39].

tau(297-391) is particularly relevant because previous studies have shown that, under defined *in vitro* conditions, it can assemble into fibrils adopting the Alzheimer's disease paired helical filament (PHF) fold [50]. However, this fragment does not intrinsically or invariably adopt this disease-associated architecture. Its aggregation behavior and fibril architecture remain highly sensitive to protein preparation, buffer composition, ionic environment, protein concentration, and assembly conditions [51]. The structural relevance of fibrils generated from tau(297-391) must therefore be evaluated under the specific conditions in which they are formed rather than inferred solely from the sequence of the construct.

This consideration is particularly important when fibrils are intended for high-resolution structural analysis. Cryo-electron microscopy helical reconstruction exploits the repetitive organization of fibrillar assemblies, and therefore benefits from fibrils that are sufficiently long, regular, well dispersed and structurally homogeneous. Such assemblies provide repeated structural information along the fibril axis that can contribute to reconstruction of the underlying molecular architecture [52]. Consequently, the suitability of an aggregation condition for higher resolution structural studies depends not only on its ability to generate ThT-positive or insoluble material, but also on the morphology and structural quality of the resulting fibrils.

On the TRA2B side, the reductionist system uses a peptide from TRA2B encompassing residues D^{133} to R^{156}, hereafter referred to as P12, a peptide derived from the RNA-recognition motif of TRA2B that encompasses the two aggregation-prone regions described in the previous section. By isolating this dual-APR region from the remainder of TRA2B, P12 provides a minimal molecular system for examining whether these sequence elements are sufficient to associate with tau(297-391) and influence fibrillar assembly.

Previous work from the SwitchLab established the functional relevance of this peptide. P12 was found to modify tau(297-391) aggregation behavior, whereas shorter peptides containing only one of the two APRs, as well as variants in which β-sheet propensity was disrupted by proline substitutions, showed little or strongly reduced activity [unpublished data, SwitchLab]. These observations suggest that the combined presence and organization of the two TRA2B-derived APRs are important for the modulatory effect of P12. Importantly, however, these previous experiments primarily established a kinetic phenotype under conditions that were not optimized for the production of extended fibrils suitable for detailed morphological or structural characterization. The present study therefore does not primarily aim to establish whether P12 can alter tau(297-391) aggregation, but rather to determine whether this effect persists under conditions supporting the formation of extended fibrillar assemblies and how it is manifested at the levels of fibril formation, molecular association, and structural organization.

Together, the tau(297-391)/P12 system provides a controlled experimental framework for moving beyond the functional observation that TRA2B-derived sequences influence tau(297-391) aggregation towards a molecular and structural characterization of this effect. By combining a minimal Tau fragment capable of forming extended fibrillar assemblies with the dual-APR-containing region of TRA2B, this approach makes it possible to investigate whether sequence-encoded heterotypic interactions are reflected in changes in aggregation behavior, co-partitioning into insoluble material, association with fibrillar assemblies, or impose structural reorganization of Tau fibrils that are sufficiently persistent to change the polymorph distribution observed.

2. Objectives of the project

The overall aim of this project was to determine how the TRA2B-derived peptide P12 influences the formation and organization of tau(297-391) fibrils and whether this effect is accompanied by a stable interaction of P12 with tau(297-391) assemblies and a redistribution of tau(297-391) polymorphs observed throughout the aggregation reaction. Building on previous evidence that the dual-APR region of TRA2B modulates Tau aggregation, the present study focused on the molecular and structural manifestations of this interaction in a controlled *in vitro* system.

The first objective was to establish a reproducible experimental workflow for the production, purification, and aggregation of tau(297-391). This required identifying conditions that provided a robust kinetic readout for comparing tau(297-391) and tau(297-391)–P12 reactions, while also developing fibrillation conditions capable of producing fibril samples amenable to cryo-electron microscopy such as paired-helical-filament-like morphologies suitable for structural investigation.

The second objective was to characterize the effect of P12 on tau(297-391) assembly. Thioflavin T fluorescence assays were used to monitor changes in aggregation kinetics. Following sedimentation, LC analysis of the supernatants was used to estimate the fractions of tau(297-391) and P12 remaining soluble from their chromatographic peak areas, while the coupled MS detector was used to confirm the identities of the detected species. Together, these approaches aimed to determine whether P12-dependent changes in aggregation behavior were accompanied by the concomitant depletion of tau(297-391) and P12 from the soluble fraction, consistent with their partitioning into sedimentable material.

The third objective was to assess whether P12 influences tau(297-391) fibril morphology and remains associated with the resulting assemblies. Negative-stain transmission electron microscopy was used to compare fibrillar morphologies and to identify samples suitable for cryo-electron microscopy imaging. In parallel, biotinylated P12 derivatives were generated and functionally evaluated before being used in dual-size nanogold labeling experiments designed to examine the spatial association of P12 with tau(297-391) fibrils.

By integrating kinetic, biochemical, morphological, and labeling-based readouts, this project aimed to distinguish between several non-mutually exclusive scenarios, including transient modulation of aggregation, association of P12 with tau(297-391) fibril surfaces or ends, stable co-assembly within the same tau(297-391) fibrillar material, and remodeling of tau(297-391) fibril morphology or architecture. The study therefore sought to move beyond the functional observation that P12 modifies tau(297-391) aggregation and towards a mechanistic and structural characterization of the tau(297-391)/P12 interaction.

3. Materials and Methods

3.1. Expression and Purification of tau(297-391)

3.1.1. Tau(297-391) construct and properties

For recombinant production, tau(297-391) was expressed as an N-terminal 6×His–SUMO fusion protein. The 6×His tag enabled purification by immobilized metal affinity chromatography, whereas SUMO was used as a solubility-enhancing fusion partner (Figure 5). The tau(297-391) construct was cloned into a pET-24(+)-based SUMO expression plasmid and transformed into chemically competent Escherichia coli BL21(DE3) cells. The predicted molecular masses of the intact fusion protein and cleaved tau(297-391) were 22.4 kDa and 10.2 kDa, respectively. The SnapGene plasmid map, complete amino acid sequences, and calculated physicochemical properties are provided in Supplementary Figure S1 and Supplementary Note 1.

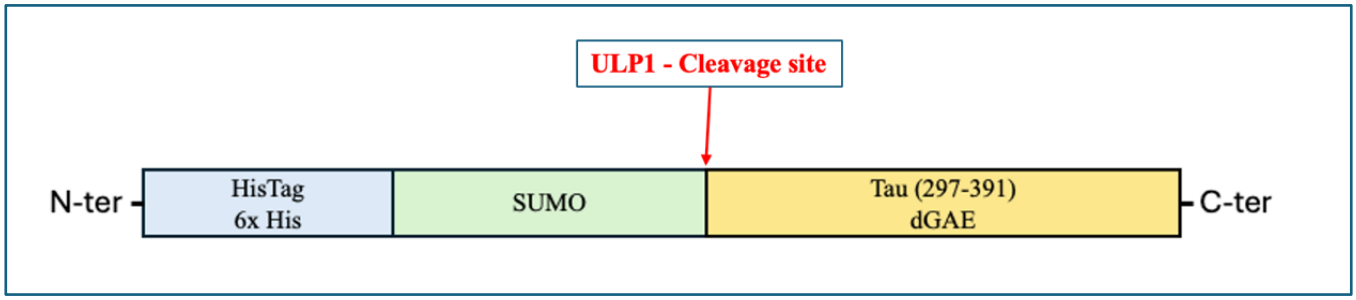


Figure 5. Schematic representation of the His–SUMO–tau(297–391) expression construct. The recombinant construct comprises an N-terminal 6×His affinity tag, followed by a SUMO solubility tag, a ULP1 cleavage site, and the Tau fragment corresponding to residues 297–391 of the human 2N4R Tau isoform. The position of ULP1 cleavage, which releases tag-free tau(297–391), is indicated.

3.1.2. Protein Expression

A starter culture was prepared by inoculating 50 µL of bacterial glycerol stock into 25 mL of lysogeny broth medium supplemented with 50 µg/mL kanamycin. The culture was incubated overnight at 37 °C with shaking at 180 rpm.

The overnight culture was used to inoculate 1 L of lysogeny broth medium containing 50 µg/mL kanamycin in a 2 L baffled flask. Cells were grown at 37 °C with shaking at 135 rpm until an optical density at 600 nm of approximately 1.0 was reached. The culture temperature was then reduced to 20 °C before induction.

Recombinant protein expression was induced by adding isopropyl β-D-1-thiogalactopyranoside to a final concentration of 0.4 mM. The culture was incubated for a further 20 h at 20 °C with shaking at 120 rpm.

Samples were collected immediately before and after induction and analyzed by SDS–PAGE to assess recombinant protein expression. Cells were subsequently harvested by centrifugation at 6,240 × *g* for 25 min at 15 °C using a JLA-8.1000 fixed-angle rotor (Beckman Coulter). The resulting cell pellets were stored at −80 °C until purification.

3.1.3. Cell Lysis

Cell pellets were resuspended in lysis buffer (50 mM 4-(2-hydroxyethyl)-1-piperazineethanesulfonic acid (HEPES), 1 M NaCl, 25 mM imidazole, 0.5 mM $MgCl_2$, 10% (v/v) glycerol, 0.1% (v/v) Triton X-100, 1 mM tris(2-carboxyethyl) phosphine (TCEP), and 1 mM benzamidine with the pH adjusted to 7.2) at a ratio of 6 mL of buffer per gram of cell pellet. For a typical purification, approximately 50 g of cell pellet was resuspended in 300 mL of lysis buffer. EDTA-free protease inhibitor tablets were added at a ratio of one tablet per 50 mL of lysis buffer.

The cell suspension was disrupted by two consecutive passages through an EmulsiFlex-C5 high-pressure homogenizer at 15,000 psi (approximately 103 MPa). The resulting lysate was subsequently sonicated on ice using a Branson 550 Sonifier equipped with a 102C (CE) probe. Sonication was performed using cycles of 5 s ON and 10 s OFF at 70% amplitude, for a cumulative ON time of 15 min. The sample was maintained on ice throughout sonication to limit heating and was processed in 300 mL volume.

Following mechanical disruption, 300 µL of DNase stock solution and a small, non-quantified amount of powdered RNase A (Sigma-Aldrich) were added per approximately 300 mL of lysate. The mixture was incubated for 30 min at room temperature to promote nucleic acid degradation and reduce lysate viscosity.

3.1.4. Nickel Affinity Chromatography (IMAC)

The lysate was clarified by centrifugation at 40,000 × *g* for 45 min at 4 °C using a JA-25.50 fixed-angle rotor (Beckman Coulter). The clarified supernatant was subsequently filtered through a 0.45 µm membrane before chromatographic purification.

Immobilized metal affinity chromatography was performed using three 5 mL HisTrap FF columns (Cytiva) connected in series, corresponding to a total resin volume of 15 mL, hereafter defined as one column volume (CV). The columns were operated on an ÄKTA pure chromatography system maintained at 4 °C. In this protocol, one column volume corresponded to the combined 15 mL resin volume of the three columns.

The compositions of all buffers used during purification are provided in Supplementary Table S1. The columns were equilibrated with 5 CV (75 mL) of IMAC buffer A at a flow rate of 5 mL/min. The filtered lysate was loaded at the same flow rate, after which the columns were washed with 6.6 CV (100 mL) of IMAC buffer A to remove unbound and weakly retained proteins.

Bound proteins were eluted using a linear gradient from 0% to 100% IMAC buffer B over 20 CV (300 mL), corresponding to an increase in imidazole concentration from 25 to 500 mM. This was followed by an isocratic wash at 100% buffer B for 3 CV to elute any remaining strongly bound material. Elution was performed at a flow rate of 5 mL/min and monitored by absorbance at 280 and 214 nm. Fractions of 3 mL were collected throughout the gradient. Selected fractions were analyzed by SDS–PAGE, and those containing the 6×His–SUMO–tau(297-391) fusion protein were pooled for proteolytic cleavage.

3.1.5. 6×His–SUMO Tag Cleavage and Dialysis

The pooled IMAC fractions (~50 mL) were supplemented with 4 mL of ULP1 protease at a concentration of 2 mg/mL and transferred into SnakeSkin regenerated cellulose dialysis tubing with a molecular-weight cut-off of 3.5 kDa. Proteolytic cleavage and dialysis were performed simultaneously overnight at 4 °C against 2 L of dialysis buffer. This step removed imidazole and reduced the NaCl concentration while allowing ULP1-mediated release of tag-free tau(297-391). Cleavage was subsequently verified by liquid chromatography–mass spectrometry (LC-MS) through detection of the expected molecular mass of tau(297-391).

3.1.6. Reverse-Phase HPLC Purification

Cleaved tau(297-391) was further purified by reverse-phase high-performance liquid chromatography using a semi-preparative ZORBAX 300SB-C18 column (9.4 × 250 mm, 5 µm particle size, 300 Å pore size from Agilent Technologies) connected to a Shimadzu HPLC system.

RP-HPLC solvent A consisted of water supplemented with 0.1% trifluoroacetic acid, whereas solvent B consisted of acetonitrile supplemented with 0.1% trifluoroacetic acid. Before injection, the protein sample was filtered through a 0.22 µm membrane.

Because the maximum injection volume was 1.5 mL, the sample was divided across multiple sequential runs. For each run, 1.3 mL was injected onto the column operated at 80 °C throughout all chromatographic runs.

Purification was performed at a flow rate of 4 mL/min. Elution was initiated at 5% solvent B, followed by a linear gradient to 15% B over 12 mL. Solvent B was then increased linearly from 15% to 35% over the subsequent 48 mL. The column was subsequently washed at 100% solvent B for 28 mL to remove strongly retained material. Finally, the column was returned to 5% solvent B and re-equilibrated for 22 mL before the next injection. Elution was monitored by absorbance at 214 and 280 nm. Fractions eluting at the pre-determined retention time of tau(297-391) were collected. Presence of tau(297-391) in these fractions was confirmed by LC–MS analysis (as described in section 3.3.1). Fractions containing tau(297-391) from successive RP-HPLC purification runs were subsequently pooled.

The pooled material was transferred to a round-bottom flask, flash-frozen in liquid nitrogen, and lyophilized overnight (~15 h) using a Christ Alpha LSCplus freeze dryer operated at a pressure of 0.02 mbar and a condenser temperature of −80 °C during the main drying cycle**.** Lyophilized tau(297-391) was stored at −20 °C until use.

3.1.7. SDS-PAGE analysis of protein expression and purification

Protein expression and purification were monitored by sodium dodecyl sulfate–polyacrylamide gel electrophoresis (SDS–PAGE) using 15-well Mini-PROTEAN TGX Any kD precast gels (Bio-Rad). For the analysis of recombinant protein expression, bacterial samples collected directly from lysogeny broth (LB) cultures were diluted tenfold in water. To monitor HisTrap purification, the cell lysate, flow-through (FT), and wash fractions were diluted tenfold, whereas

collected elution fractions were diluted fivefold, all in water. Samples were subsequently mixed with SDS-containing sample buffer and heated at 95 °C for 5 min before loading alongside a molecular-weight marker (PageRuler™ Unstained Protein Ladder, 10-200 kDa from Thermo Scientific). Electrophoresis was performed at 200 V for approximately 35 min using a Bio-Rad electrophoresis system connected to a PowerPac HC power supply. Following electrophoresis, protein bands were visualized using Imperial Protein Stain. The resulting banding patterns were used to assess expression of the 6×His–SUMO–tau(297–391) fusion protein and monitor subsequent purification steps.

3.1.8. Protein identity, quality control, and storage

The identity of purified tau(297-391) was confirmed by LC-MS. The experimentally measured molecular mass was compared with the theoretical mass calculated from the tau(297-391) amino-acid sequence (Supplementary Note S1).

The final protein yield was determined using dry mass and expressed as mg of purified tau(297-391) per liter of bacterial culture. Purified tau(297-391) batches were considered suitable for aggregation experiments when LC–MS analysis confirmed the expected molecular mass and showed no detectable contaminating peaks.

After validation, tau(297-391) was stored in lyophilized form at −20 °C.

3.2. P12 Peptide Preparation and handling

3.2.1. Preparation of tau(297-391) aggregation mixtures and buffer exchange

Aggregation reactions were assembled in a final volume of 100 µL per well from three separately prepared components. The appropriate reaction buffer was first adjusted to the required pH and then supplemented with the salt and reducing agent specified for each experimental condition. Lyophilized tau(297–391) was dissolved directly in this mixture. As 50 µL of the tau(297–391)-containing solution was added per well, tau(297–391), salt, and reducing-agent concentrations were adjusted to twice their intended final concentrations. In contrast, the buffer was maintained at its intended final concentration because all reaction components were prepared in the same buffer.

Where applicable, P12 or a P12-derived peptide was dissolved separately in the same reaction buffer. The peptide and ThT concentrations were adjusted to account for the addition of 30 µL of this solution per well, corresponding to 3.33 times their intended final concentrations. Finally, 20 µL of the appropriate seed preparation was added, corresponding to five times its intended final concentration and bringing the total reaction volume to 100 µL. For peptide-free or seed-free control reactions, the corresponding volume was replaced with the appropriate buffer-containing vehicle.

For experiments requiring buffer exchange, tau(297–391) was first dissolved and subsequently desalted into the corresponding buffer–salt–reducing-agent mixture using 2 mL Zeba Spin Desalting Columns with a 7K molecular-weight cut-off, suitable for sample volumes of 200–700 µL (Thermo Scientific). The columns were equilibrated with the desired exchange mixture, and buffer exchange was performed according to the manufacturer's instructions (*Zeba*

Spin Desalting Columns and Plates, 7K MWCO). Following recovery, the tau(297–391) concentration was adjusted to the required working concentration before assembly of the aggregation reactions.

3.2.2. Solid-phase peptide synthesis (SPPS)

The initial batch of P12 used in this study was synthesized by solid-phase peptide synthesis (SPPS) by R.K., a member of the SwitchLab, before the start of the present project. An additional batch of P12 and several biotinylated P12 derivatives were subsequently synthesized during the project using an automated Fmoc-based SPPS protocol.

Peptide synthesis was performed using an Intavis MultiPep RSI peptide synthesizer equipped with a vortex agitation system. Reactions were conducted at room temperature in 5 mL reactor syringes at a synthesis scale of 0.025 mmol. Unmodified P12 was synthesized using TentaGel R RAM resin with a loading capacity of 0.20 mmol/g. For biotinylated P12 derivatives, peptide assembly was initiated on a resin bearing a preattached biotinylated lysine residue, enabling incorporation of the biotin moiety into the resulting peptide. Before peptide assembly, the resin was preconditioned by washing three times for 1 min with a 1:1 mixture of dimethylformamide (DMF) and dichloromethane (DCM).

Fmoc-protected amino acids and the coupling reagents HATU and HBTU were prepared as 0.5 M stock solutions in DMF. N-methylmorpholine (NMM) was prepared as a 4 M stock solution in DMF, and a 20% piperidine solution in DMF was used for Fmoc deprotection.

Each automated synthesis cycle comprised three successive steps:

1. **Fmoc deprotection:** The resin was treated twice with 600 µL of 20% piperidine in DMF for 5 and 8 min, respectively, followed by washing with DMF (3.6 mL; 7 × 70 s).
2. **Amino acid coupling:** Each amino acid was incorporated using two successive coupling reactions. The first coupling used Fmoc-AA-OH/HATU/NMM at a molar ratio of 5:4.9:10 and proceeded for 15 min. The second coupling used Fmoc-AA-OH/HBTU/NMM at the same molar ratio and proceeded for an additional 15 min. The resin was subsequently washed with DMF (3.6 mL; 1 × 70 s).
3. **Capping:** A capping solution was prepared directly in the reactor syringe by sequentially adding 300 µL of 4 M lutidine in DMF and 300 µL of 4 M acetic anhydride in DMF, resulting in a final concentration of 2 M for each component. The reaction was allowed to proceed for 5 min, followed by washing with DMF (3.6 mL; 7 × 70 s).

Following completion of peptide assembly, the synthesized peptides were cleaved from the resin by treatment for 3 h with a cleavage cocktail composed of trifluoroacetic acid (TFA), triisopropylsilane (TIS), and water (95:2.5:2.5, v/v/v). The released peptides were subsequently precipitated in cold methyl tert-butyl ether (MTBE) and collected as crude peptide material.

The identities of the synthesized peptides were assessed by LC–MS by comparing the experimentally measured molecular masses with their corresponding theoretical values. The complete peptide sequences and calculated molecular masses are provided in Supplementary Table S2. P12 was stored in lyophilized form at −20 °C until use and dissolved in the appropriate buffer before aggregation experiments.

3.3. Biophysical characterization

3.3.1. Liquid Chromatography–Mass Spectrometry

Liquid chromatography–mass spectrometry (LC–MS) was used throughout the study to confirm the molecular identity of tau(297-391) and P12-derived peptides and to quantify the soluble fractions of both components during sedimentation assays.

Analytical LC–MS was performed using a Shimadzu Prominence LC-30 system equipped with a ZORBAX 300 Extend-C18 analytical column (2.1 × 100 mm, 3.5 µm particle size, 300 Å pore size; Agilent Technologies) and a narrow-bore ZORBAX 300 Extend-C18 guard column (2.1 × 12.5 mm, 5 µm particle size; Agilent Technologies). The column was operated at 80 °C throughout the analysis.

LC–MS mobile phase A consisted of water supplemented with 0.1% formic acid, whereas mobile phase B consisted of acetonitrile supplemented with the same 0.1% formic acid.

Chromatographic separation was performed at a flow rate of 0.35 mL/min. Elution was initiated at 5% mobile phase B, which was maintained for 1.5 min. Mobile phase B was then increased linearly from 5% to 95% over the subsequent 8.5 min. The column was subsequently held at 95% B for 3 min before returning to 5% B and being re-equilibrated for 2 min prior to the next analysis.

Samples were diluted five-fold prior to analysis, and 10 µL was injected for each measurement. Elution was monitored using a photodiode array detector at 214 nm. Mass spectra were acquired online using a Shimadzu LCMS-2020 single-quadrupole mass spectrometer equipped with an electrospray ionization (ESI) source operated in positive-ion mode. Data acquisition and analysis were performed using LabSolutions software (Shimadzu).

3.3.2. Thioflavin T assay

Aggregation kinetics were recorded using Thioflavin T (ThT), a fluorescent dye whose emission increases upon binding to amyloid assemblies. Each reaction condition was prepared in 3 technical replicate wells, with 100 µL of reaction mixture per well, using a black, half-area, clear flat-bottom 96-well fluorescence plate. ThT was added to a final concentration of 20 µM. Fluorescence was recorded every 5 min at 37 °C under continuous shaking at 200 rpm using a FLUOstar Omega plate reader, with excitation and emission wavelengths set to 440 and 480 nm, respectively, and a 10 nm bandwidth for each. Fluorescence data were processed and plotted using R through RStudio.

3.3.3. Sedimentation assay

To evaluate the conversion of monomeric tau(297-391) into aggregated form in the absence or presence of P12, a sedimentation assay was conducted. Aggregation reactions were prepared in a 96-well plate following the previously described protocol for measuring ThT aggregation kinetics. Wells were collected at two defined time points: at the start of the experiment (t = 0) and after the corresponding ThT fluorescence profiles had reached a plateau, to assess the fraction of protein remaining soluble. For each time point, the entire 100 µL volume of the corresponding well was

mixed by repeated pipetting to resuspend fibrillar material before transfer to an ultracentrifugation tube. Samples were then centrifuged at 436,000 × g for 1 h at 4 °C using an Optima TL-100 ultracentrifuge equipped with a TLA-100 rotor (Beckman Coulter) to sediment fibrillar and other insoluble assemblies. The resulting supernatant, representing the remaining soluble fraction, was collected and analyzed by LC–MS. The first time point was processed in technical replicate using the same procedure. The LC peak area corresponding to the monomer at t = 0 h was set as 100%, and subsequent changes in peak area were used to calculate the percentage of soluble tau(297-391) or P12.

3.3.4. Preparation of tau(297-391) fibril seeds

For the initial aggregation-screening experiments, previously prepared fibrils generated from 400 µM tau(297-391) in 10 mM phosphate buffer (PB), 150 mM NaCl, and 10 mM DTT were used as seeds. For subsequent experiments, new tau(297–391) seed stocks were prepared under the optimized conditions selected during protocol optimization and described in Section 4.6.2. Briefly, 100 µL reactions containing 100 µM tau(297–391) were prepared in a microplate and incubated for four days using the temperature and agitation settings described in Section 3.3.2.

P12 seeds were generated by incubating 50 µM P12 for three days in 10 mM PB, pH 7.4, containing 150 mM NaCl, 10 mM DTT and 20 µM ThT.

The formation of ThT-reactive amyloid assemblies was monitored by fluorescence throughout the incubation. Immediately before plate preparation, the stored fibril suspension was thoroughly resuspended by repeated pipetting to obtain a homogeneous distribution of fibrillar material. The volume required for each experiment was withdrawn and diluted to the desired working concentration. Seed concentrations were expressed as monomer equivalents based on the starting concentration of tau(297–391) or P12 used to generate each fibril preparation, rather than as an absolute concentration of fibril particles.

The diluted fibril suspension was divided into 100 µL aliquots in 0.2 mL tubes compatible with the Bioruptor sonication system. Samples were sonicated for 15 min using alternating cycles of 30 s ON and 30 s OFF in a water bath maintained at 4 °C. After sonication, all aliquots originating from the same preparation were pooled and mixed to homogenize the resulting seed suspension before addition to the aggregation reactions.

3.4. Electron microscopy

3.4.1. Negative-stain TEM

Fibrillar samples were analyzed by negative-stain transmission electron microscopy (TEM). A 300-mesh copper grid coated with carbon/Formvar-film (Agar Scientific) was glow-discharged for 30 s in vacuum at 50% voltage power using a homemade glow discharger. Immediately after glow discharge, 4 µL of sample was applied to the carbon-coated side of the grid and allowed to adsorb for 2 min.

Excess sample was removed by blotting with filter paper. The grid was then washed three times by contact with ultrapure water, with excess liquid removed after each wash, and subsequently stained by contact with 2% (w/v) uranyl acetate. The grid was incubated with the stain for 1 min, after which excess uranyl acetate was removed by blotting. The grid was allowed to air-dry for 5 min at room temperature and was stored in a grid box until imaging.

Micrographs were acquired using a JEOL1400 operated at an accelerating voltage of 80 kV and equipped with an Olympus Quemesa camera.

3.4.2. Morphometric analysis and classification of PHF-like fibrils

Negative-stain TEM micrographs were examined to assess fibril morphology. For fibrils displaying an apparent periodic twist, the minimum and maximum widths were measured at the narrowest and widest positions, respectively. The crossover distance was defined as the longitudinal distance between successive equivalent points of the periodic width modulation. Fibrils were classified as PHF-like when they displayed a minimum width of approximately 10 nm, a maximum width of approximately 20 nm, and a crossover distance of approximately 75–80 nm, consistent with previously reported criteria for recombinant tau(297–391) fibrils [53]. The n values reported in the figures correspond to individual morphometric measurements (crossover distances or widths), not fibrils or independent replicates This classification was based exclusively on fibril morphology and did not establish the presence of the Alzheimer tau fold.

3.4.3. Dual-size nanogold labeling

Dual-size nanogold labeling was performed to enable the simultaneous visualization of biotinylated P12 and tau(297-391) fibrillar assemblies by transmission electron microscopy. Biotinylated P12 was detected using 15 nm gold nanospheres functionalized with streptavidin and Cy3, whereas tau(297-391) fibrils were labeled using the mouse monoclonal antibody MN423, which recognizes the C-terminally truncated Tau epitope ending at Glu391, followed by a donkey anti-mouse secondary antibody conjugated to 6 nm gold particles.

For the grid preparation, a 4 µL aliquot of fibril-containing sample was deposited and allowed to adsorb for 3 min before excess liquid was blotted away. Grids were subsequently washed three times with Milli-Q water followed by two washes with PBS (pH 7.4).

For P12-Biotin labeling, grids were incubated in a humidity chamber maintained at 25ºC with 20 µL of streptavidin-conjugated 15 nm gold nanoparticles diluted 1:20 for 1.5 h. Excess reagent was then removed by blotting, and the grids were washed three times with TBST.

For tau(297-391) labeling, grids were incubated for 1.5 h with MN423 diluted 1:500 in PBS in a homemade humidity chamber maintained at 25ºC. Following three washes with TBST, grids were incubated for a further 1.5 h with the 6 nm gold-conjugated donkey anti-mouse secondary antibody diluted 1:50 in the same chamber. Grids were subsequently washed three times with TBST and twice with Milli-Q water.

Finally, grids were negatively stained with 2% (w/v) uranyl acetate, air-dried for approximately 5 min, and imaged by transmission electron microscopy

3.4.4. Cryo-EM grid preparation and vitrification

Fibrillar samples containing tau(297-391) alone, tau(297-391) incubated with P12, or P12 alone, when applicable, were prepared for cryo-EM. Before vitrification, samples were examined by negative-stain TEM to assess fibril abundance, morphology, bundling, and overall suitability for cryo-EM screening.

Because grid preparation required optimization, several conditions were evaluated, including the type of holey support grid, glow-discharge parameters, sample concentration, applied volume, blotting conditions, and vitrification-robot settings. For each preparation, approximately 4–5 µL of sample was applied to a glow-discharged grid. Excess liquid was automatically removed by the blotting-robot using filter paper, and then the grid was rapidly plunge-frozen in liquid ethane cooled to –168 ºC using a Leica EM GP2 automated plunge freezer (Leica Microsystems) at the CNL-VIB BioImaging Core Leuven. Vitrified grids were stored in liquid nitrogen until screening.

3.4.5. Cryo-EM grid screening

Vitrified grids were screened at the Cryo-EM Platform of the Rega Institute (KU Leuven) using a 200 kV Glacios cryo-transmission electron microscope (Thermo Fisher Scientific) equipped with a Falcon 4i direct electron detector and a Selectris energy filter operated at 10 eV slit width.

Grid quality was evaluated with particular attention to vitreous ice thickness and distribution, fibril abundance, fibril dispersion within the holes, separation of individual fibrils, and the extent of bundling, stacking, or overlap. Representative regions were imaged during screening to assess the suitability of each specimen for potential subsequent cryo-EM data acquisition.

4. Results

4.1. Recombinant production and validation of tau(297-391)

4.1.1. Recombinant expression of His-SUMO-tau(297-391)

To produce tau(297–391) for subsequent experiments, recombinant expression of the His–SUMO fusion construct was assessed by SDS–PAGE (Figure 6). Following IPTG induction in *Escherichia coli*, a prominent band in the range corresponding to the expected molecular mass was detected in whole-cell samples from all culture flasks but was absent before induction, consistent with successful expression of His–SUMO–tau(297–391).

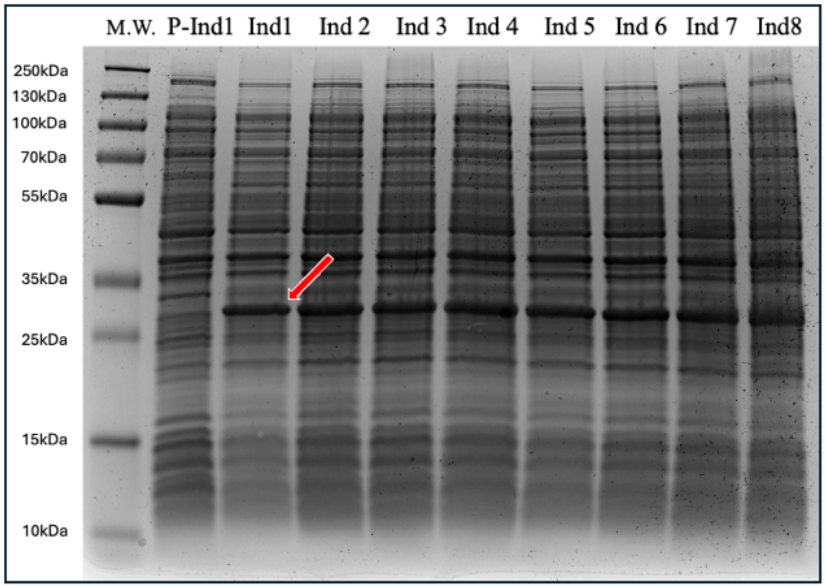


Figure 6. Recombinant expression of His–SUMO–tau(297–391) in *Escherichia coli*. Representative SDS–PAGE analysis of whole-cell lysates collected before and after IPTG induction. Following induction, a prominent band appeared near the 25 kDa molecular-weight markers, at a position consistent with the predicted molecular mass of the His–SUMO–tau(297–391) fusion protein (approximately 22.4 kDa). The position of this band is indicated by the red arrow.

Having confirmed recombinant expression of the fusion construct, the next step was to isolate tau(297-391) and verify the identity of the tag-free fragment.

4.1.2. Purification and validation of tag-free tau(297-391)

Purification of tau(297-391) was initiated by applying the clarified soluble lysate to an immobilized metal affinity chromatography (IMAC) column, exploiting the N-terminal 6×His tag of the fusion construct. The fusion protein was retained on the nickel-affinity column and recovered upon elution (Figure 7 A). SDS–PAGE analysis showed that the elution fractions were strongly enriched in a protein band matching with the expected molecular mass of His–SUMO–tau(297-391), whereas most bacterial proteins were detected in the flow-through (Figure 7 B).

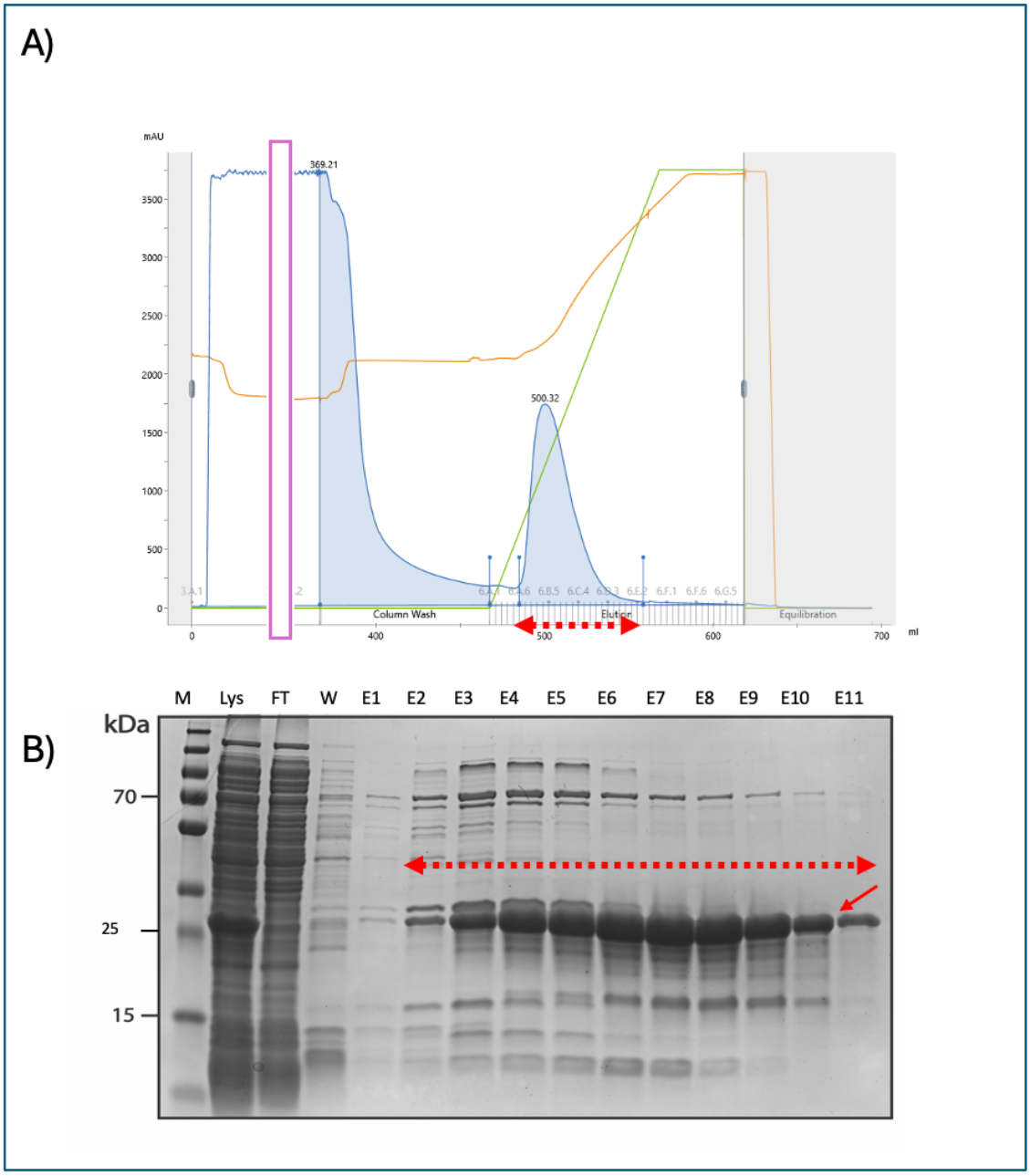


Figure 7. Immobilized metal affinity purification of His–SUMO–tau(297–391). (A) Representative IMAC chromatogram showing the purification of His-tagged SUMO–tau(297–391). The purple box indicates the sample application phase, which is not displayed in full for clarity. The red dashed double-headed arrow indicates the elution fractions collected for further processing. **(B)** Corresponding SDS–PAGE analysis of the molecular-weight marker (M), lysate (Lys), flow-through (FT), wash (W), and elution fractions (E1–E11). The red dashed double-headed arrow indicates the fractions selected following the IMAC, corresponding to those highlighted in panel A, while the red arrow indicates the band corresponding to His–SUMO–tau(297–391).

The His–SUMO tag was subsequently removed by ULP1 protease cleavage to release tag-free tau(297-391). LC–MS analysis performed before and after digestion showed the disappearance of most of the intact fusion-protein signal and the appearance of the cleaved tau(297-391) fragment (Figure 8 A and B). LC–MS analysis confirmed that the

corresponding peak was attributable to tau(297–391), consistent with efficient cleavage of the His–SUMO fusion protein (Figure 8 C).

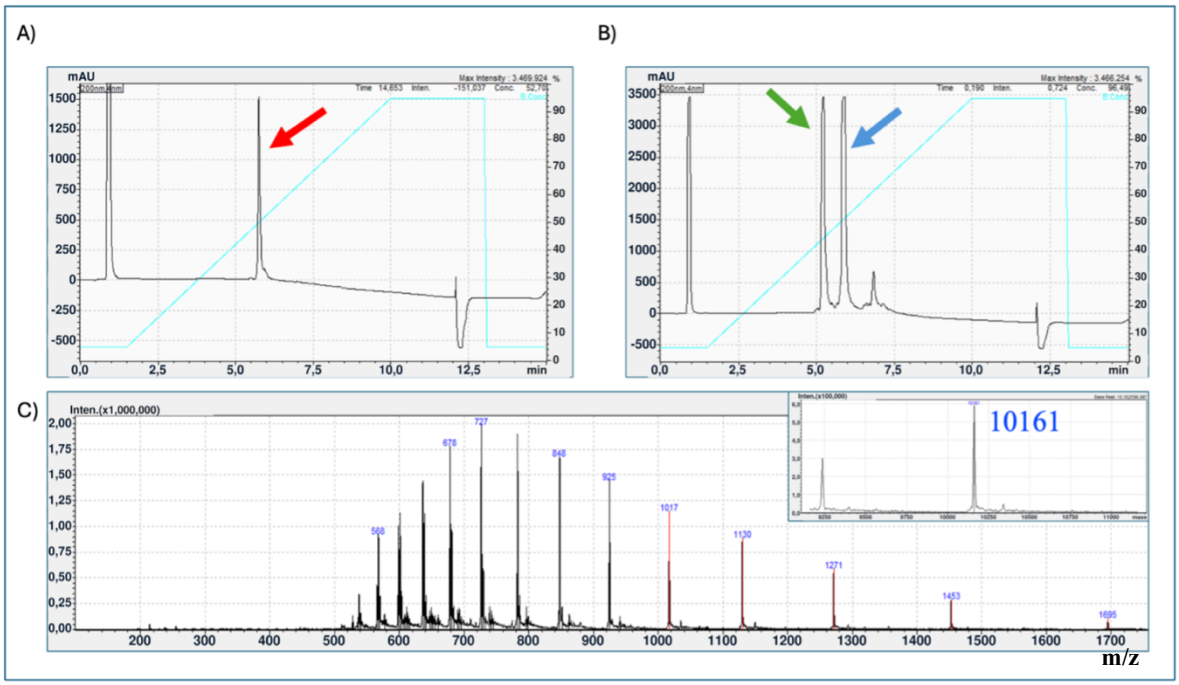


Figure 8. LC–MS analysis of ULP1 cleavage of His–SUMO–tau(297-391). (A) LC–MS chromatogram before ULP1 digestion, with the red arrow indicating uncleaved His–SUMO–tau(297-391). **(B)** Chromatogram after ULP1 digestion, showing tau(297-391) (green arrow) and free His–SUMO (blue arrow). **(C)** Mass spectrum of the tau(297-391)-associated peak highlighted in green in panel B. The upper-right insert shows the deconvoluted mass peak at 10,161 Da, consistent with tag-free tau(297-391).

Following cleavage, the sample was further purified by reverse-phase high-performance liquid chromatography (RP-HPLC) to separate tau(297-391) from the released His–SUMO tag, residual ULP1 protease, and remaining impurities (Figure 9). The chromatographic profile contained a well-defined peak corresponding to tau(297-391), and the associated fractions were collected and pooled. LC–MS analysis of the pooled material determined a molecular mass consistent with that expected for tag-free tau(297-391), thereby confirming the identity of the purified fragment (Supplementary Figure S2).

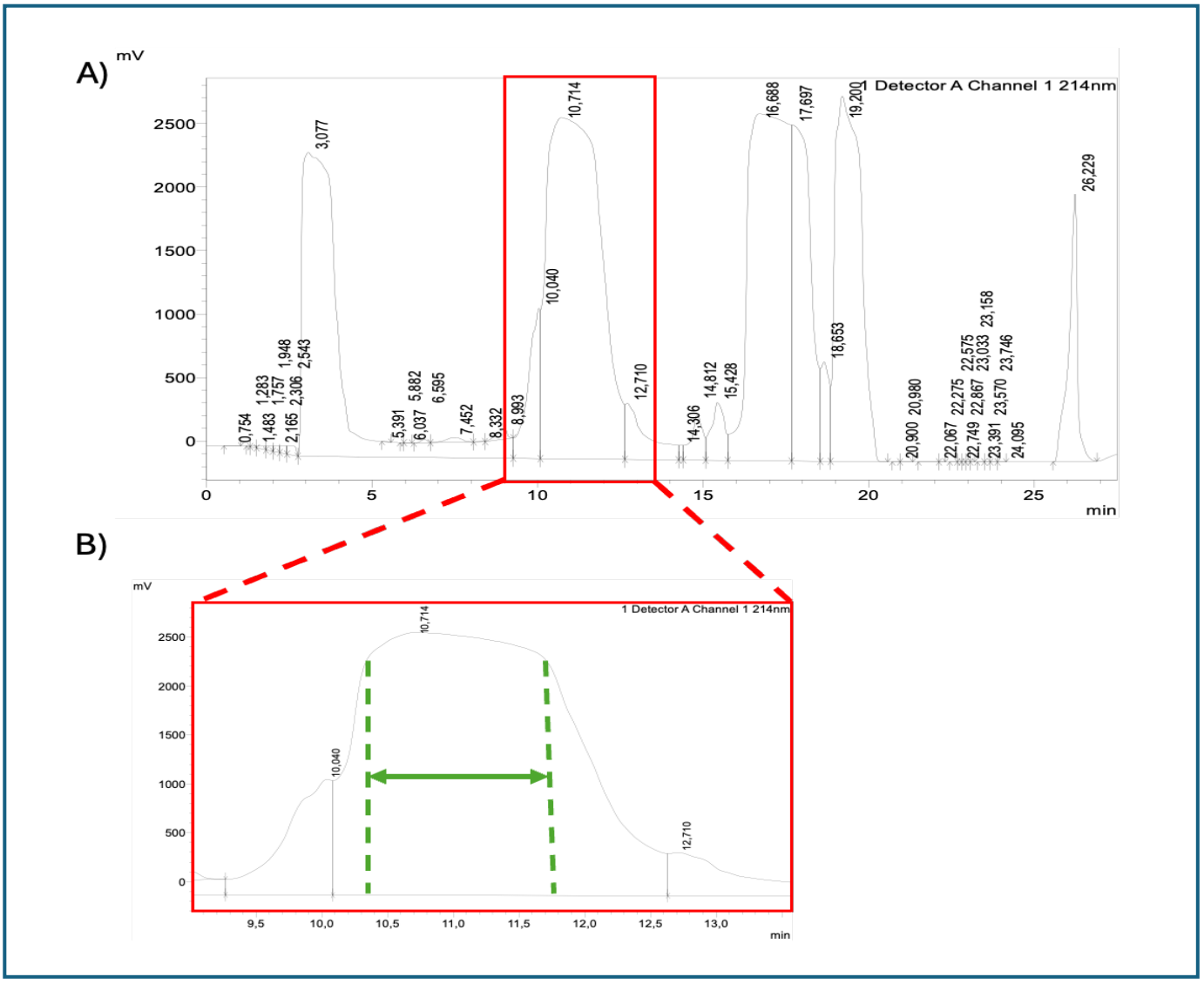


Figure 9. RP-HPLC purification of tau(297-391). The selected RP-HPLC peak is enlarged in the lower-left panel, with the collected fraction indicated by the green dashed limits and arrow. The corresponding LC–MS analysis confirming the expected tau(297-391) molecular mass is shown in Supplementary Figure S2.

The purified tau(297-391) fractions were subsequently pooled, lyophilized, and stored at -20ºC until use. Production yields for each independent tau(297-391) batch are reported in Supplementary Table S3. Together, these results demonstrate the establishment of a reproducible procedure for producing and isolating tag-free tau(297-391) and provided a biochemically validated material for subsequent aggregation experiments.

The effect of P12 on tau(297-391) assembly was then investigated using a combination of ThT fluorescence assays, LC-based solubility measurements, negative-stain TEM, nanogold labeling, and Cryo-EM screening. These complementary approaches were used to assess aggregation kinetics, the partitioning of tau(297-391) and P12 into sedimentable material, fibril morphology, and the association of P12 with fibrillar assemblies.

4.2. Establishment of initial aggregation conditions for tau(297-391)/P12 system

4.2.1. ThT-based screening of aggregation conditions

Because aggregation behavior is highly sensitive to its physicochemical environment, an initial screening was performed to identify conditions providing a clear and reproducible aggregation readout for the tau(297-391)/P12 system. At this stage, the aim was not to establish the molecular nature of the interaction between tau(297-391) and P12, but to identify an experimental window in which potential P12-dependent effects could subsequently be evaluated against appropriate tau(297-391)-only controls.

Aggregation reactions contained fixed concentrations of 28 µM tau(297-391) and 7 µM P12. NaCl was included to provide an environment approaching physiological ionic strength, whereas $MgCl_2$ was selected because $MgCl_2$-based conditions have previously been used to promote the formation of disease-relevant fibrillar conformations by tau(297-391) [50]. Both salts were tested at concentrations of 50, 100, and 150 mM in 10 mM phosphate buffer (PB) adjusted to pH 5.8, 6.4, or 7.4.

In addition, all initial reactions contained 10 mM dithiothreitol (DTT) as a reducing agent to maintain the single cysteine residue of tau(297-391), Cys322, in a reduced state. Reducing conditions were retained because the oxidation state of Cys322 has been shown to strongly influence tau(297-391) assembly and fibril morphology [54]. Each condition was evaluated either in the absence of seeds or in the presence of 1 µM preformed tau(297-391) seeds (Section 3.3.4.). The formation of ThT-reactive assemblies was monitored continuously throughout the incubation period. The complete matrix of tested conditions is presented in Figure 10 B, together with representative fluorescence profiles for the conditions that produced a detectable ThT response. The complete ThT fluorescence profiles for the remaining screening conditions are provided in Supplementary Figure S3.

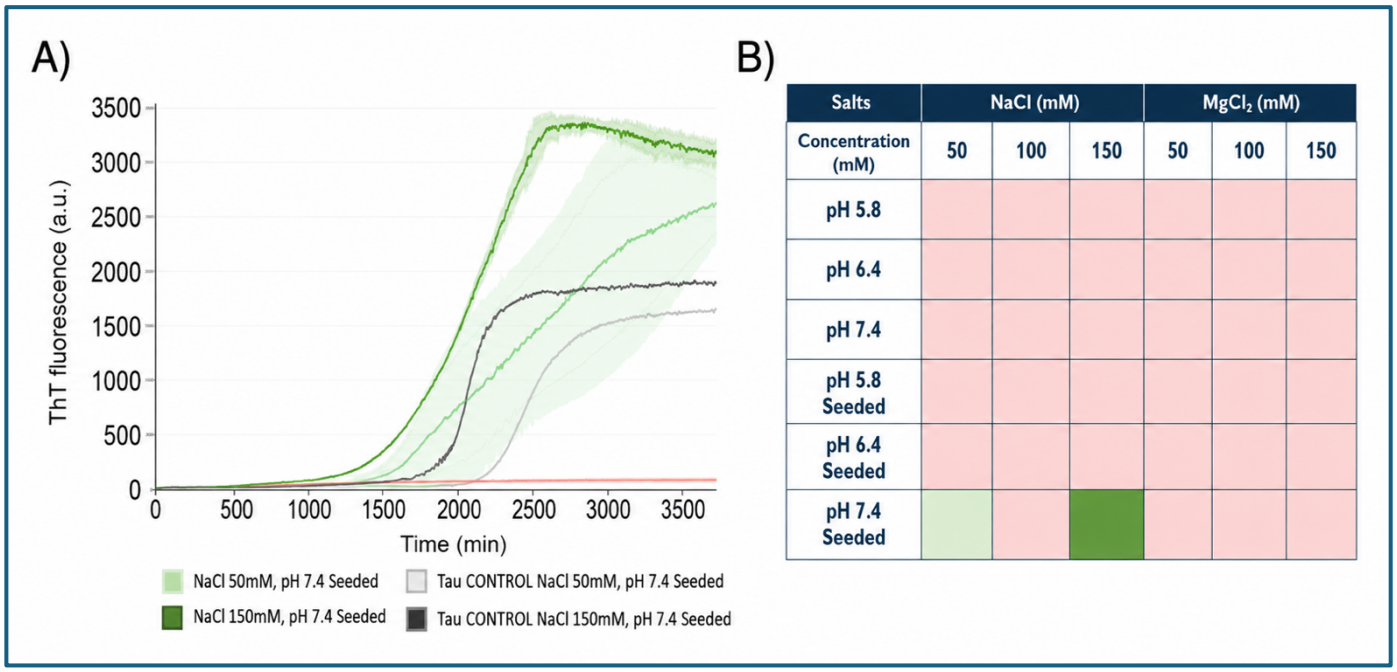


Figure 10. Initial screening of aggregation conditions for the tau(297–391)/P12 system. (A) ThT fluorescence kinetics for the seeded NaCl conditions producing detectable aggregation, using 28 µM tau(297–391), 7 µM P12 and 1 µM preformed tau(297-391) seeds. Corresponding tau(297-391)-only controls are shown in gray. **(B)** Screening matrix of NaCl and $MgCl_2$ concentrations (50–150 mM), pH (5.8–7.4) and seeding conditions in 10 mM phosphate buffer containing 10 mM DTT. Green indicates conditions producing a detectable ThT increase within the observation period; red indicates ThT-negative conditions.

The screening revealed a strong dependence of the aggregation response on both pH and seeding. No detectable increase in ThT fluorescence was observed at pH 5.8 or 6.4 under any of the salt conditions tested. Similarly, non-seeded reactions remained ThT-negative within the experimental observation period, including at pH 7.4. Positive responses were restricted to seeded reactions performed at pH 7.4 in the presence of NaCl, indicating that both a near-neutral pH and preformed tau(297-391) seeds were required to obtain a measurable aggregation response under these initial conditions.

Among the NaCl-containing reactions, both 50 and 150 mM NaCl supported the formation of ThT-reactive assemblies, whereas none of the $MgCl_2$-containing reactions produced a detectable ThT response. At 50 mM NaCl, the two replicate curves differed in the onset of the fluorescence increase, whereas the profiles obtained at 150 mM NaCl were closely superimposed and displayed a pronounced growth phase followed by consistently high final fluorescence.

Based on these kinetic results, seeded reactions containing 150 mM NaCl at pH 7.4 were selected as the initial working condition for investigating the concentration-dependent modulation of tau(297-391) aggregation by P12. The correspondence between the ThT response and the formation of sedimentable material was subsequently evaluated by LC–MS-based solubility measurements.

4.2.2. Tau(297-391) and P12 solubility across the pH 7.4 screening conditions

LC–MS-based solubility measurements were performed to assess the partitioning of tau(297–391) and P12 into sedimentable material under ThT-positive conditions and to verify that comparable losses of solubility did not occur in reactions lacking a detectable ThT response (Figure 11).

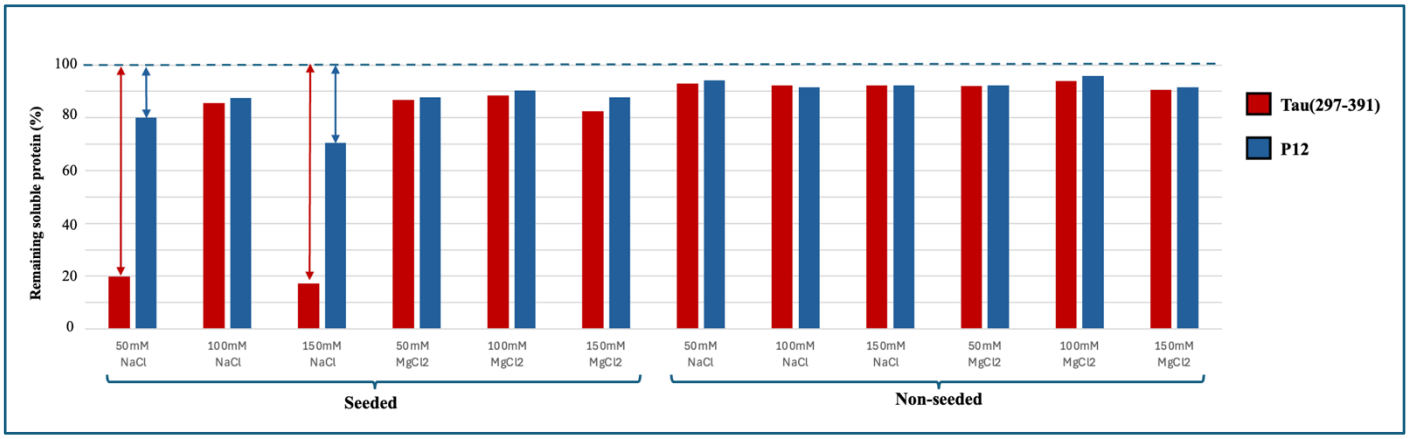


Figure 11. LC–MS-based solubility analysis of Tau(297–391) and P12 under initial screening conditions at pH 7.4. Remaining soluble tau(297–391) (red) and P12 (blue) were quantified after incubation and normalized to their respective levels at $t = 0$ (100%, blue dashed line). Seeded and non-seeded reactions containing 50, 100, or 150 mM NaCl or $MgCl_2$ are shown. Red and blue arrows indicate the depletion of soluble tau(297-391) and P12, respectively.

Under seeded, NaCl-containing conditions that supported amyloid formation, the soluble fraction of tau(297–391) decreased markedly. Soluble P12 also decreased, although to a lesser extent, indicating that both components partitioned into sedimentable material under these conditions.

By contrast, tau(297–391) and P12 remained predominantly soluble in ThT-negative reactions. Neither component therefore underwent substantial sedimentation under conditions that did not support detectable amyloid formation.

These findings supported the selection of seeded reactions containing 150 mM NaCl at pH 7.4 for subsequent tau(297–391)–P12 experiments.

4.3. P12 modulates tau(297-391) aggregation kinetics in NaCl conditions

4.3.1. P12 concentration reshapes tau(297-391)-associated ThT kinetics

Having established seeded aggregation reactions in the presence of NaCl as an initial experimental framework, we next examined whether P12 influenced the aggregation kinetics of tau(297-391) over a broad concentration range under these conditions. Tau(297-391) concentration was maintained at 28 µM throughout the successive titration experiments, while the concentration of P12 was progressively increased. Tau(297-391)-only reactions were included as controls and was subsequently examined to assess whether the peptide independently contributed to the observed ThT fluorescence profiles.

Within the initial concentration range, ThT-positive aggregation events were observed more frequently in samples containing both tau(297-391) and P12 than in the tau(297-391)-only controls, for which only one replicate developed a substantial fluorescence signal. The profiles obtained at 3, 7, and 14 µM P12 did not follow a consistent concentration-dependent response (Figure 12.).

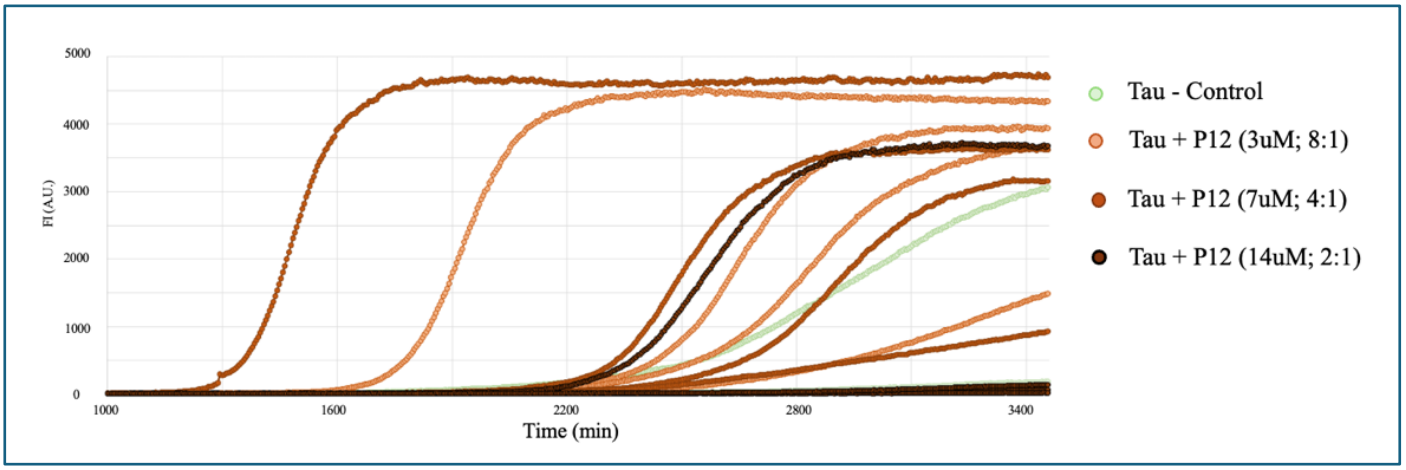


Figure 12. Effect of increasing P12 concentrations on tau(297–391) aggregation kinetics. ThT fluorescence profiles of tau(297–391) alone or in the presence of 3, 7, or 14 µM P12, corresponding to the indicated tau(297-391):P12 molar ratios. Fluorescence intensity is shown as a function of incubation time, with individual traces displayed for each replicate.

A second titration extended the P12 concentration range from 14 to 56 µM. At 14 µM P12 all replicate curves displayed a later increase in ThT fluorescence than the tau(297-391)-only control (Figure 13). At 28 µM P12, the fluorescence transition occurred slightly earlier than in the control, although the profiles remained partly overlapping. By contrast, 56 µM P12 produced a distinct early fluorescence increase followed by an earlier main transition. Together, these results indicate that P12 concentration reshaped the tau(297-391)-associated ThT response, ranging from a delayed onset at 14 µM to modest and pronounced acceleration at 28 and 56 µM, respectively.

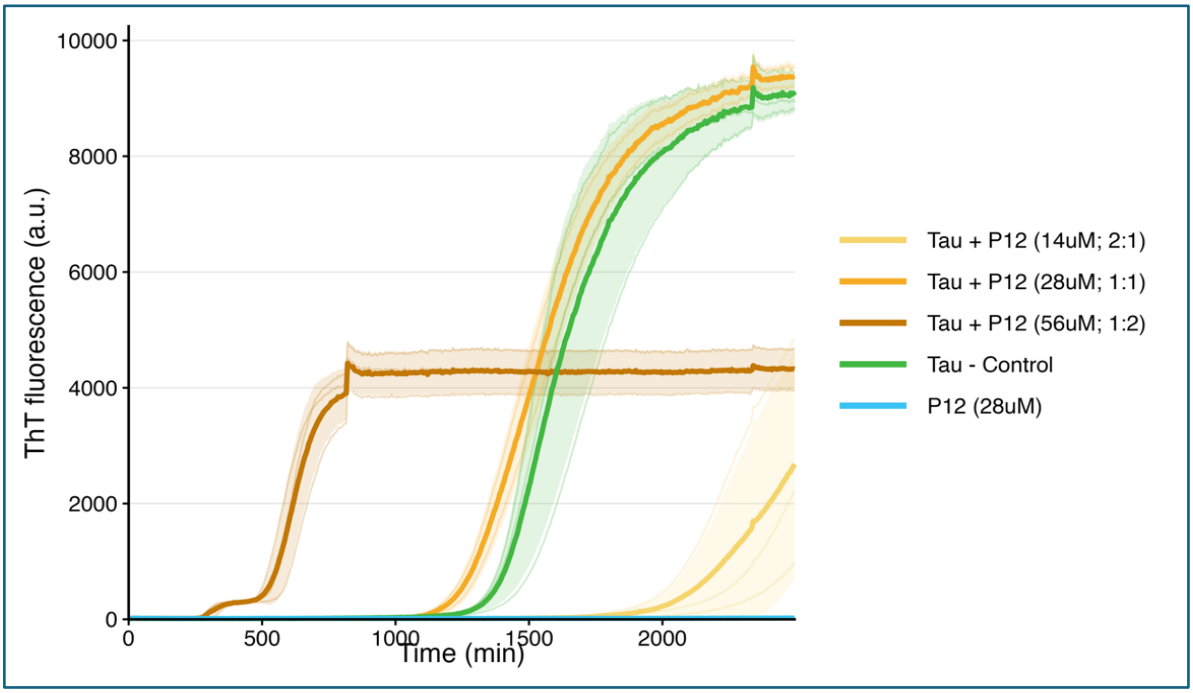


Figure 13. ThT fluorescence profiles of 28 µM tau(297–391) alone or in the presence of 14, 28, or 56 µM P12, corresponding to tau(297-391):P12 molar ratios of 2:1, 1:1, and 1:2, respectively. A P12-only control at 28 µM was included. Fluorescence intensity is shown as a function of incubation time, with individual replicate traces displayed for each condition. Bold lines represent mean ThT fluorescence profiles, with individual replicates shown in lighter shades.

This qualitative change prompted a third titration covering a broader range of P12 concentrations, from 28 to 168 µM. Within this higher concentration range, increasing P12 concentrations progressively shortened the lag phase preceding the main ThT fluorescence transition, revealing a clear concentration-dependence contrary to what was observed in previous experiments (Figure 14.).

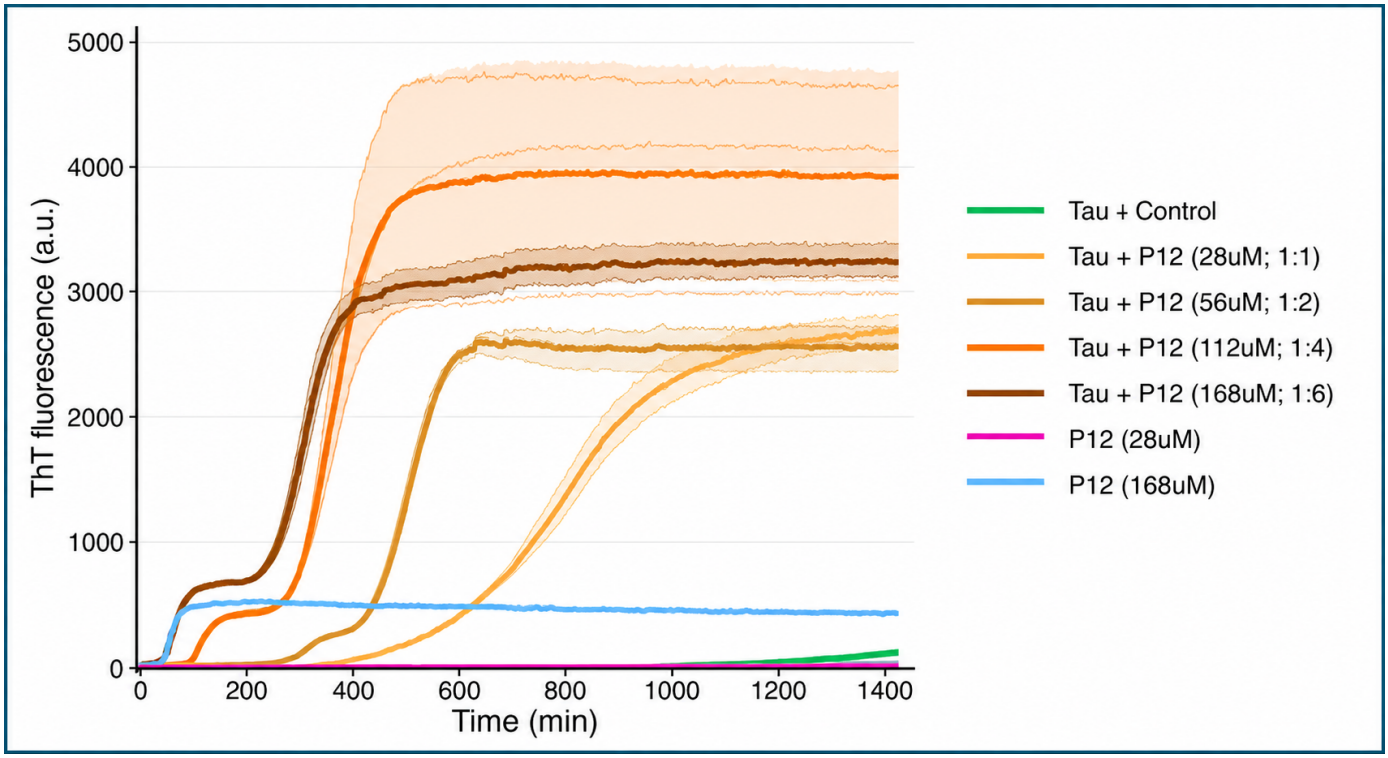


Figure 14. Effect of increasing P12 concentrations on tau(297–391) aggregation kinetics. ThT fluorescence profiles of 28 µM tau(297–391) alone or in the presence of 28, 56, 112, or 168 µM P12. P12-only controls at 28 and 168 µM were included. Bold lines represent mean ThT fluorescence profiles, with individual replicates shown in lighter shades.

The corresponding profiles were also highly reproducible between replicate reactions. However, from 56 µM P12 onwards, the curves consistently displayed a biphasic profile, comprising an early, lower-amplitude ThT-positive transition followed by the larger and progressively accelerated later transition.

In the tau(297-391)-containing reaction with 168 µM P12, the early fluorescence transition closely overlapped with the ThT-positive response observed in the 168 µM P12-only controls. The P12-only response showed that, at this concentration, P12 could independently form ThT-reactive assemblies under NaCl conditions tested. This temporal correspondence suggests that the first event could be predominantly associated with the formation of P12-derived ThT-reactive assemblies rather than with the main tau(297-391)-associated aggregation transition. The second main event nevertheless occurred substantially earlier as the P12 concentration increased, demonstrating that the presence of P12, altered the subsequent aggregation behavior of the tau(297-391)-containing system.

Although these kinetic profiles did not demonstrate a direct seeding mechanism, they raised the possibility that P12 first forms ThT-reactive assemblies that subsequently facilitate tau(297-391) aggregation. This hypothesis was therefore investigated more directly by testing whether preformed P12 assemblies could seed tau(297-391).

4.3.2. Preformed P12 assemblies promote tau(297-391) aggregation

The early ThT-positive event observed at high P12 concentrations raised the possibility that P12 assemblies formed before the major tau(297-391)-associated transition and subsequently facilitated tau(297-391) aggregation. To

investigate this hypothesis, P12 seeds were subsequently added to tau(297-391) at final concentrations of 0.5, 1, 2, or 4 µM, expressed as P12 monomer equivalents, and the formation of ThT-reactive material was monitored over time.

Tau(297-391)-containing reactions supplemented with preformed P12 assemblies developed clear ThT-positive responses, whereas tau(297-391)-only control reactions remained ThT-negative over the same observation period (Figure 15).

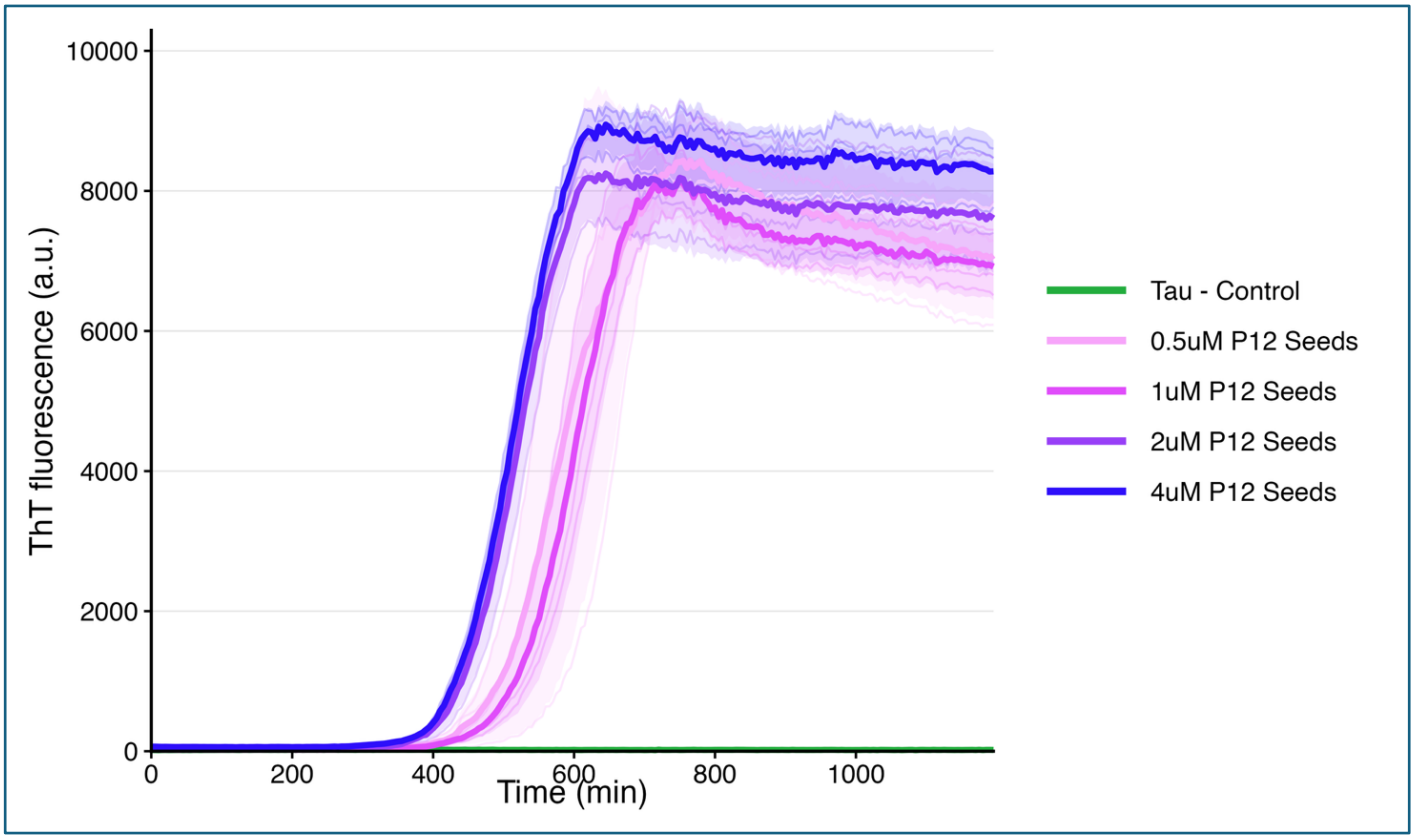


Figure 15. Preformed P12 assemblies promote a ThT-positive response in tau(297–391) reactions. Tau(297–391) was incubated with preformed P12 assemblies at final concentrations of 0.5, 1, 2, or 4 µM, expressed as P12 monomer equivalents. Tau(297-391)-only reactions served as controls. Bold lines represent mean ThT fluorescence profiles, with individual replicates shown in lighter shades. All P12-seeded conditions developed a clear ThT-positive response, whereas the tau(297-391)-only control remained ThT-negative over the observation period.

Earlier fluorescence increases were observed under all the tested conditions, particularly at P12 seed concentrations of 2 and 4 µM. However, variability between replicates and the absence of a consistent pattern across intermediate concentrations prevented the identification of a clear concentration-dependent effect.

4.4. TEM reveals fibrillar assemblies with limited suitability for further structural investigation

4.4.1. Morphological characterization of NaCl-derived fibrils

Although seeded NaCl conditions provided a clear kinetic readout by ThT fluorescence, this assay does not describe the morphology of the resulting assemblies. Endpoint samples containing 28 µM tau(297-391) alone or 28 µM tau(297-391) co-incubated with 14 µM P12 were therefore examined by negative-stain transmission electron microscopy.

Tau(297-391)-only samples contained abundant fibrillar material organized predominantly into large, dense clusters (Figure 16). These assemblies were composed of long, relatively straight fibrils displaying extensive lateral association, overlap, and bundling. Individual fibrils were often difficult to distinguish within the most densely packed regions, and no clear or regularly recurring twisted morphology was apparent in the fields examined.

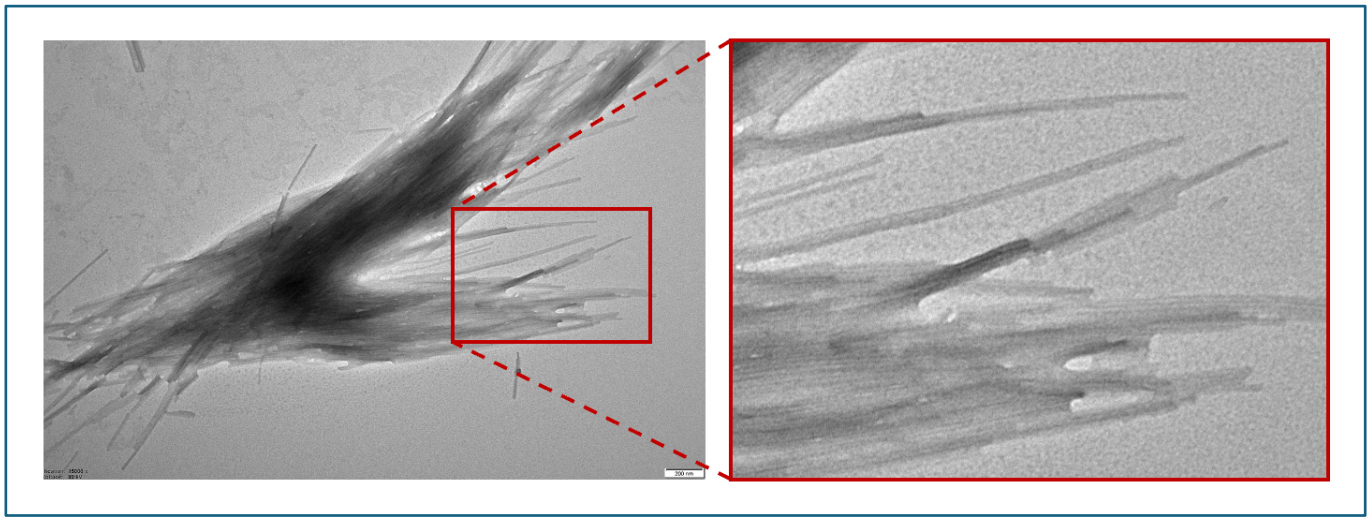


Figure 16. Negative-stain TEM analysis of tau(297–391) fibrils formed under seeded NaCl conditions. Tau(297–391)-only samples displayed abundant long, relatively straight fibrils organized into dense bundles with extensive lateral association and overlap. The enlarged view highlights individual non-twisted fibrils within the clustered material.

Samples containing both tau(297-391) and P12 displayed a more heterogeneous organization (Figure 17). Some regions resembled the tau(297-391)-only samples, with relatively straight fibrils arranged into dense laterally associated bundles. Other regions showed a less aligned and more interconnected network-like organization. Within these heterogeneous clusters, occasional fibrils displayed an apparent twisted or undulating profile, as illustrated at higher magnification in Figure 17.

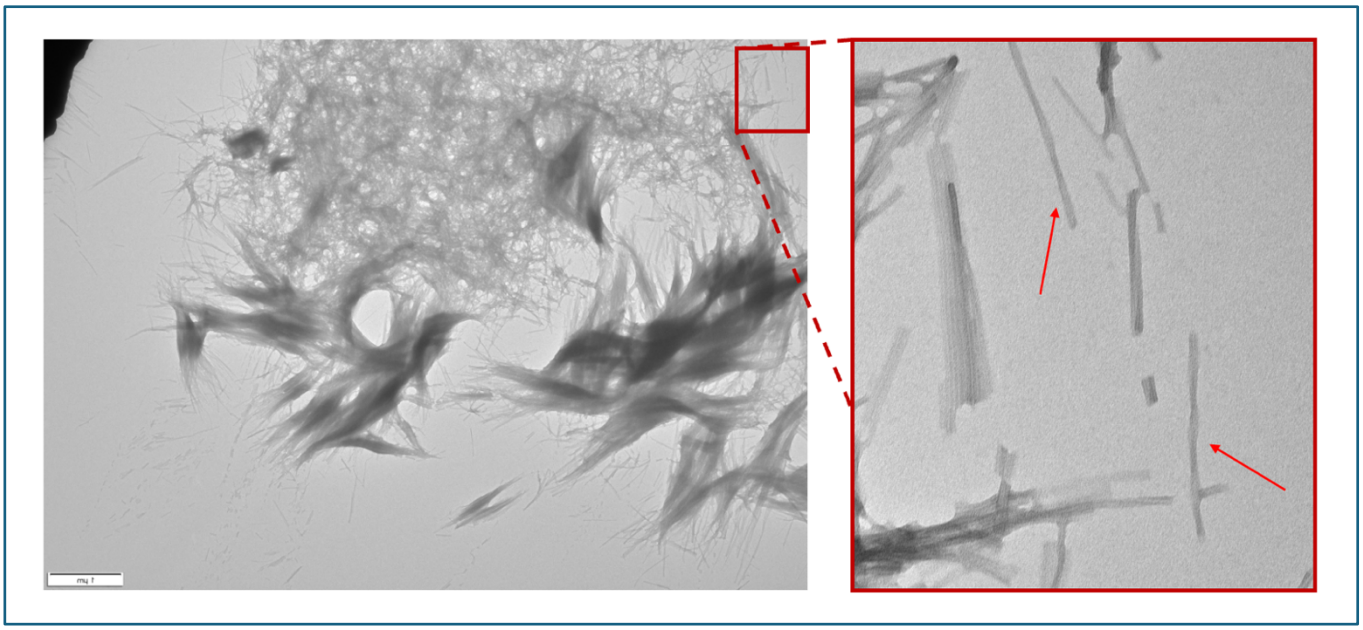


Figure 17. Negative-stain TEM analysis of tau(297–391) fibrils formed in the presence of P12 under seeded NaCl conditions. Samples displayed a heterogeneous organization, combining dense bundles of relatively straight fibrils with less aligned, interconnected fibrillar networks. The enlarged view highlights fibrils showing an apparent twisted or undulating morphology (red arrows).

These observations suggested that the presence of P12 may influence the organization or morphology of fibrillar assemblies generated under NaCl-containing conditions. However, the apparent difference remained qualitative and was not observed uniformly throughout the tau(297-391)–P12 sample.

Overall, NaCl conditions generated abundant fibrillar material. However, tau(297-391)-only assemblies were predominantly organized into straight, densely bundled clusters and lacked the regular helical twist required for helical reconstruction by cryo-EM. Although the tau(297-391)–P12 sample contained more heterogeneous clusters and occasional apparently twisted fibrils, the prevalence and structural significance of these features could not be determined from negative-stain TEM alone. Thus, while the NaCl condition provided a suitable experimental framework for monitoring aggregation kinetics, it did not provide a well-defined structural reference for evaluating the consequences of tau(297-391)–P12 co-incubation.

At this stage, it could not be assumed that one fibril morphology was intrinsically more informative than another. However, because the structural component of this study was framed in the context of Alzheimer's disease, paired helical filaments represented a particularly relevant reference state. As PHFs constitute the predominant Tau filament morphology in Alzheimer's disease, reproducing this assembly state with tau(297-391) would provide an interesting model for assessing P12-dependent morphological changes. This rationale prompted the re-evaluation and optimization of $MgCl_2$-based aggregation conditions, as aggregates grown in the presence of this salt had previously displayed periodic width modulation and crossover features resembling those of PHFs. [40; 53].

4.4.2. Published $MgCl_2$-based PHF-like conditions initially fail in the current system

Published aggregation conditions reported to generate PHF-like tau(297-391) fibrils were first reproduced in the current experimental system. These initial protocols were then complemented by systematic variations in tau(297-391) concentration, $MgCl_2$ concentration, temperature, agitation, and reaction vessel. The full set of experimental conditions tested is summarized in Figure 18, together with the principal morphological outcome observed for each condition. Following incubation, each sample was examined by negative-stain TEM to assess fibril formation and morphology. The corresponding negative-stain TEM micrographs are provided in Supplementary Figure S4.

Reference or experimental condition	Tau(297–391) concentration	Buffer	pH	$MgCl_2$ or other additive	Reducing agent	Shaking conditions	Temperature	Reaction vessel / format
Al-Hilaly et al., 2017	100 µM	10 mM phosphate buffer	7.4	None	10 mM DTT	700 rpm	37 °C	Plate in plate reader
Lövestam et al., 2022, condition without added salt	400 µM	10 mM phosphate buffer	7.4	None	10 mM DTT	Orbital shaking at 200 rpm	37 °C	Plate in plate reader
Lövestam et al., 2022, condition 4a	400 µM	10 mM phosphate buffer	7.4	200 mM $MgCl_2$	10 mM DTT	Orbital shaking at 200 rpm	37 °C	Plate in plate reader
This study – plate-based condition	200 µM	10 mM phosphate buffer	7.4	200 mM $MgCl_2$	10 mM DTT	Orbital shaking at 200 rpm	37 °C	Plate in plate reader
This study – variation 1	200 µM	10 mM phosphate buffer	7.4	200 mM $MgCl_2$	10 mM DTT	Orbital shaking at 200 rpm	37 °C	Eppendorf tube
This study – variation 2	200 µM	10 mM phosphate buffer	7.4	200 mM $MgCl_2$	10 mM DTT	Orbital shaking at 220 rpm	37 °C	Glass vial
This study – variation 3	200 µM	10 mM phosphate buffer	7.4	200 mM $MgCl_2$	10 mM DTT	Static incubation	37 °C	Glass vial
This study – reproduction of Lövestam condition 4a	400 µM	10 mM phosphate buffer	7.4	200 mM $MgCl_2$	10 mM DTT	Orbital shaking at 200 rpm	37 °C	Eppendorf tube

Figure 18. Summary of tau(297–391) aggregation conditions tested for the generation of PHF-like fibrils. Published conditions from Al-Hilaly et al. (2017) and Lövestam et al. (2022) were reproduced and subsequently modified by varying tau(297-391) concentration, $MgCl_2$ concentration, agitation conditions, and reaction vessel. Buffer composition, pH, reducing conditions, temperature, and incubation format are indicated for each condition.

Contrary to expectations, none of the initially tested conditions produced a clear and homogeneous population of fibrils satisfying these PHF-like criteria described in section 3.4.2. Instead, TEM revealed substantial morphological heterogeneity. Several conditions generated broad ribbon-like assemblies without a clearly resolved periodic twist. In some cases, these assemblies displayed an apparent twist, but their crossover distances were substantially longer than the approximately 80 nm periodicity expected for PHF-like fibrils. Their appearance was therefore more consistent with the lateral association or bundling of straighter fibrils into twisted ribbon-like structures than with individual paired helical filaments.

Other conditions produced long straight fibrils arranged into parallel stacks or dense bundles, while some samples contained irregular fibrillar material or poorly defined aggregates. Although occasional local twisting was observed, none of the conditions reproducibly generated fibrils displaying the crossover distances characteristic of the PHF-like morphology described in Section 3.4.2.

4.5. Buffer chemistry explains and resolves the failure to generate PHF-like fibrils

4.5.1. Phosphate/$MgCl_2$ incompatibility alters the aggregation environment

Despite their documented use, $MgCl_2$-based conditions failed to generate PHF-like fibrils in our hands. This led to a closer examination of the chemical environment established during sample preparation. Aggregation mixtures containing both phosphate buffer and $MgCl_2$ frequently developed visible turbidity and, in some cases, a precipitate after the components were combined.

To evaluate the stability of these conditions, four phosphate/$MgCl_2$-containing formulations were prepared, and their pH was monitored over three days. After mixing, three formulations were adjusted to pH 8.0, whereas the fourth was adjusted to pH 7.5. The pH of each complete reaction mixture was measured once every 24 h. Despite their different starting values, all four formulations underwent progressive acidification, with an overall decrease of approximately one pH unit over the monitoring period (Figure 19). Thus, adjustment of the initial pH was insufficient to maintain a stable aggregation environment over the timescale of fibril formation.

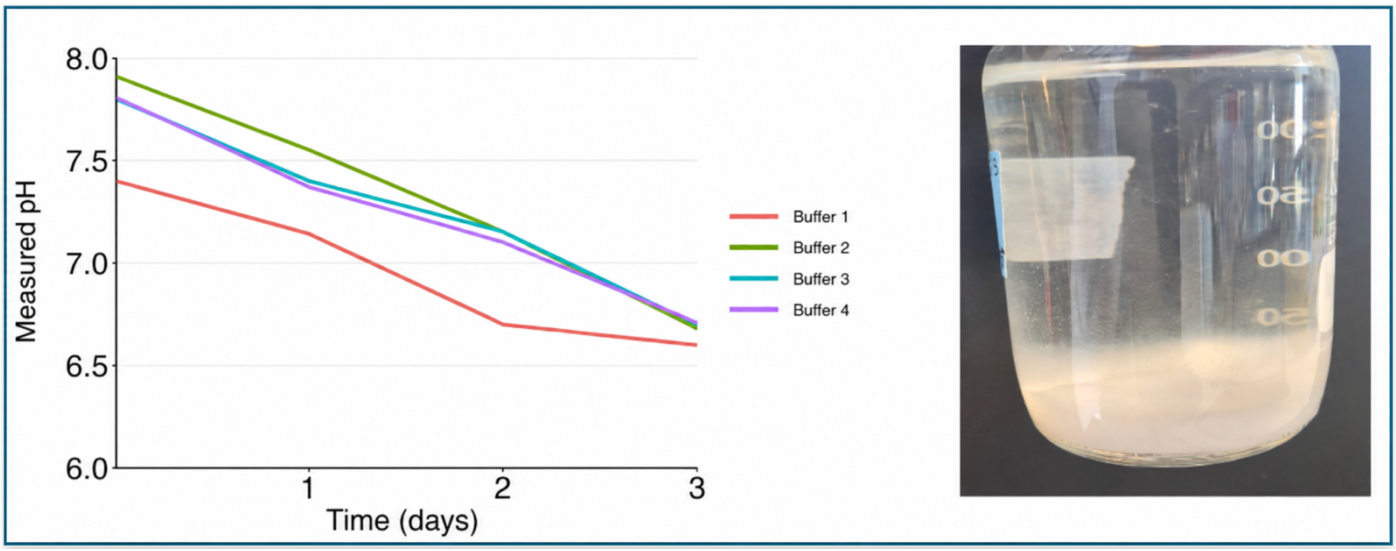


Figure 19. pH instability and visible precipitation in phosphate/$MgCl_2$-containing aggregation conditions. Left, evolution of the measured pH of four formulations over three days following component mixing. Buffer 1 was initially adjusted to pH 7.5, whereas buffers 2–4 were adjusted to pH 8.0. All formulations showed progressive acidification, reaching approximately pH 6.6–6.7 after three days. Right, representative photograph showing the turbidity and precipitate observed 3 days after combining phosphate buffer and $MgCl_2$. The chemical identity of the precipitate was not experimentally determined.

Several poorly soluble magnesium phosphate species may form in aqueous solution, depending on pH, ion concentrations, ionic strength, and equilibration time. [55] Because the precipitated material was not chemically characterized, its composition could not be assigned to a specific phase. Nevertheless, theoretical solubility calculations indicated that precipitation was plausible under the concentrations used and predicted substantial depletion of soluble phosphate (Supplementary Note 2).

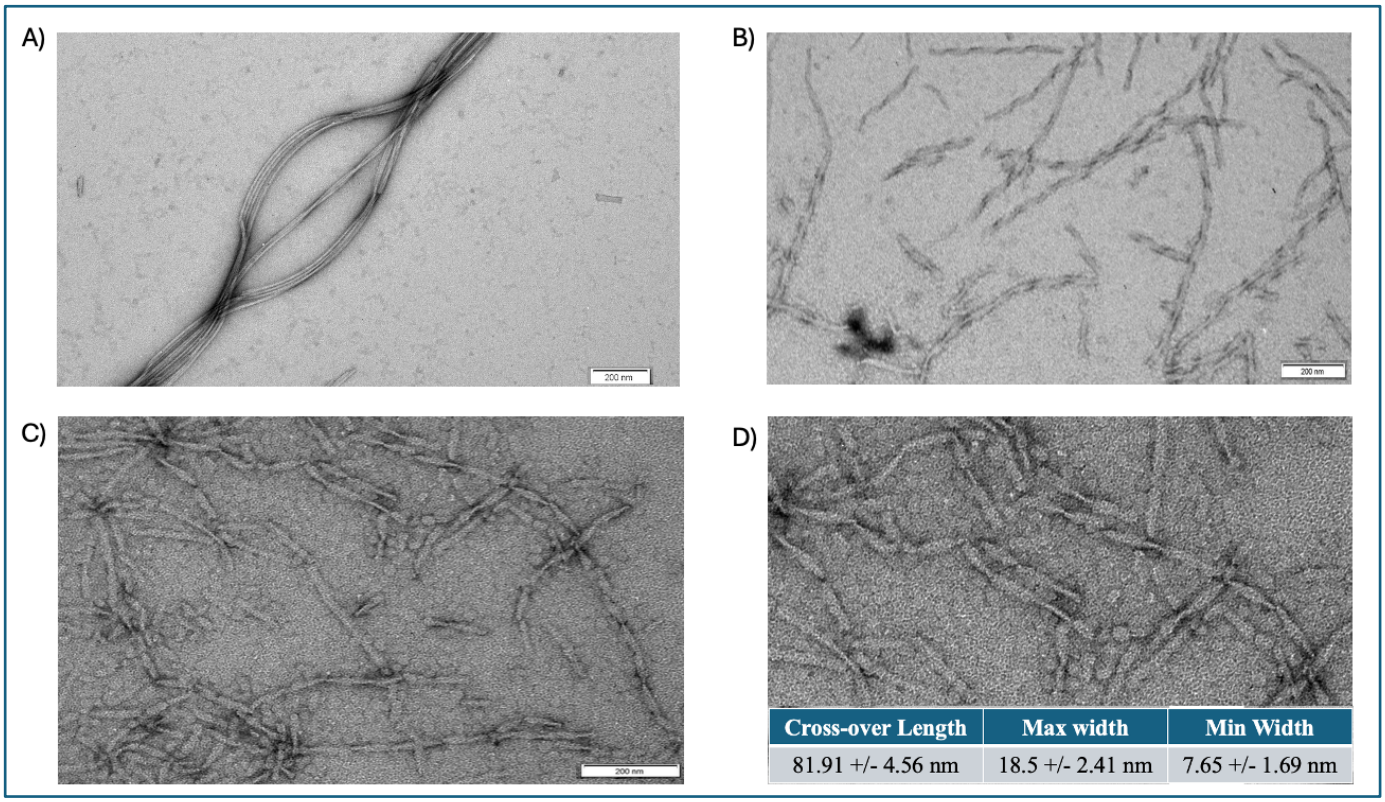
Together, these results indicated that the phosphate/$MgCl_2$ mixture did not maintain a stable reaction environment. This instability was particularly relevant because the initial ThT screening showed reduced or undetectable tau(297–391) aggregation at pH 6.4 and 5.8. Optimization strategies were therefore evaluated to improve the reaction conditions while retaining $MgCl_2$.

4.5.2. Buffer optimization restores PHF-like Tau fibril morphology

In addition to the buffer composition, the tau(297–391) sample was considered a potential source of acidification, as redissolution of the lyophilized protein at this concentration range (200-400 µM) could alter the pH of the final reaction mixture.

Two modifications were evaluated while maintaining $MgCl_2$ and DTT concentrations at 200 mM and 10 mM, respectively: replacement of the phosphate buffer with 20 mM HEPES and desalting of the tau(297–391) stock solution before aggregation.

Under both modified conditions, negative-stain TEM revealed fibrils with a clearly resolved periodic modulation in width, in contrast to the broad ribbons, stacked straight fibrils, and irregular assemblies observed under the initial conditions (Figure 20). The measured fibril widths and crossover distances were compatible with PHF-like morphology.



Cross-over Length	Max width	Min Width
81.91 +/- 4.56 nm	18.5 +/- 2.41 nm	7.65 +/- 1.69 nm

Figure 20. Improved control of the aggregation environment restores PHF-like tau(297–391) fibril morphology. (A) Representative negative-stain TEM image of the non-PHF-like assemblies generated under the initial phosphate/$MgCl_2$ condition. **(B)** Fibrils obtained after replacement of phosphate with HEPES. **(C)** Fibrils obtained using tau(297–391) desalted before incubation. **(D)** Higher-magnification views of representative PHF-like fibrils, with minimum and maximum widths and crossover length indicated. Crossover length and widths were measured from 17 individual crossover events (n = 17).

These results established $MgCl_2$-containing conditions capable of reproducibly producing PHF-like tau(297-391) fibrils and provided a disease-associated morphological reference system for subsequent experiments.

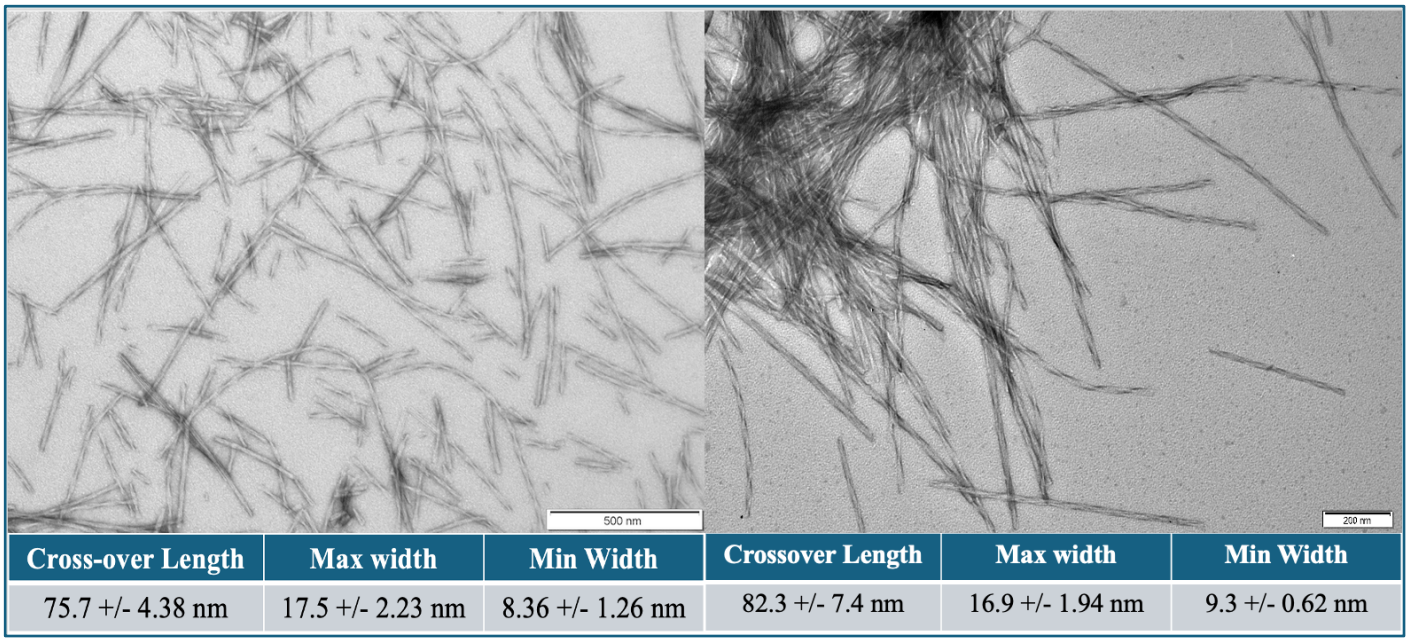
4.6. Optimized $MgCl_2$ conditions provide a PHF-like context for reassessing P12 effects

4.6.1. Stepwise adaptation of the optimized conditions to lower tau(297–391) concentration

The replacement of phosphate with HEPES was first validated under the initial high-concentration fibrillation conditions of 400 µM tau(297-391). Negative-stain TEM confirmed that the HEPES/$MgCl_2$ system supported the formation of

fibrils displaying a periodic modulation in width and dimensions compatible with the previously defined PHF-like morphological criteria.

We next investigated whether the tau(297-391) concentration could be progressively reduced without losing this morphology. As an intermediate step, the optimized conditions were tested at 100 µM tau(297-391). After 4 days of incubation, negative-stain TEM revealed fibrillar assemblies retaining a resolved periodic twist and morphometric features compatible with a PHF-like morphology (Figure 21, left).



Cross-over Length	Max width	Min Width	Crossover Length	Max width	Min Width
75.7 +/- 4.38 nm	17.5 +/- 2.23 nm	8.36 +/- 1.26 nm	82.3 +/- 7.4 nm	16.9 +/- 1.94 nm	9.3 +/- 0.62 nm

Figure 21. Stepwise adaptation of the optimized $MgCl_2$-based protocol to lower tau(297–391) concentrations. (A) Representative negative-stain TEM images of fibrils generated at 100 µM tau(297–391) under the optimized conditions. *n* = 86. **(B)** Representative fibrils generated at 28 µM tau(297–391) in 20 mM HEPES, pH 7.4, 200 mM $MgCl_2$, and 2 mM TCEP. Higher-magnification panels show the periodic width modulation of representative fibrils. Minimum and maximum widths and crossover distances are indicated where applicable. *n* = 42. Scale bars: 500 nm in A and 200 nm in B.

The protocol was then adapted to 28 µM tau(297-391) and the use of 1 µM seeds. Because these fibrillation reactions extended over several days and required reducing conditions to be maintained throughout the incubation, the reducing agent initially used, DTT, was replaced with TCEP.

The resulting low-concentration formulation contained 28 µM tau(297-391), 1 µM tau(297-391) seeds, 20 mM HEPES at pH 7.4, 200 mM $MgCl_2$, and 2 mM TCEP. Negative-stain TEM showed that this condition also generated fibrils displaying clearly resolved periodic crossover distances and width modulation corresponding to the PHF-like reference range (Figure 21, right).

Accordingly, the 100 µM condition was selected for seed preparation, whereas the seeded 28 µM condition was used for subsequent experiments investigating the influence of P12.

4.6.2. Generation and TEM validation of fibril-derived tau(297-391) seeds

The 100 µM tau(297-391) fibril preparation characterized above and shown in Figure 21 A was selected for seed production. Following 4 days of incubation, mature fibrils from this preparation were subjected to sonication as described in Section 3.3.4. Negative-stain TEM revealed numerous fibrillar fragments shorter than the parental fibrils, although longer fibril fragments were also observed (Figure 22).

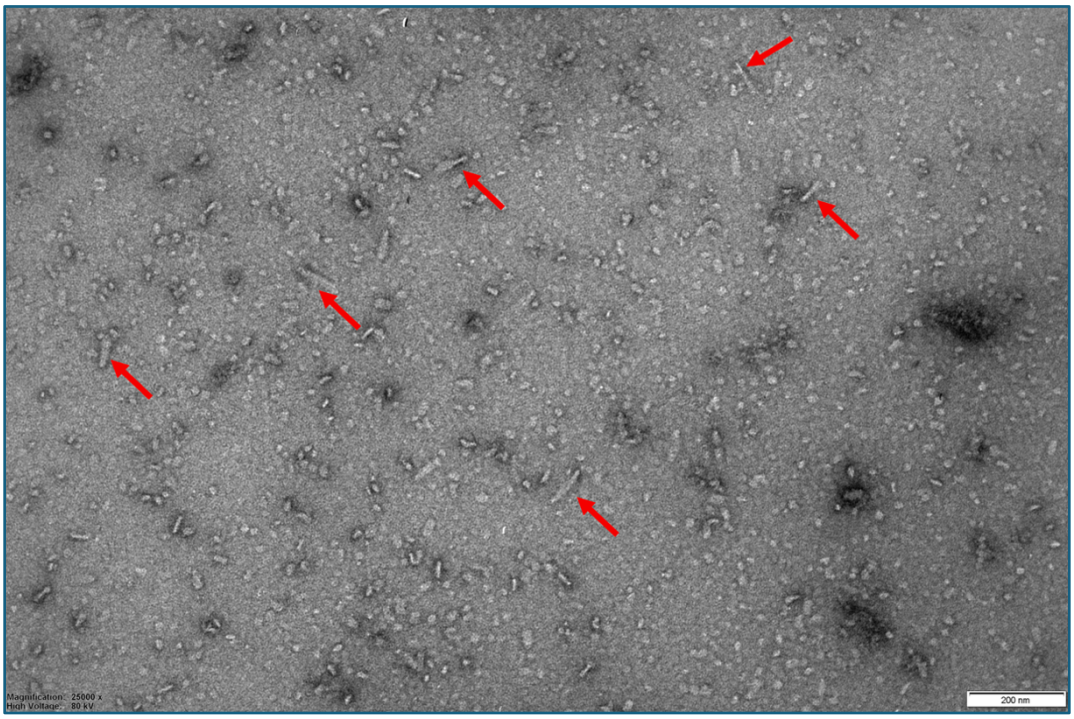


Figure 22. TEM imaging of seeds derived from PHF-like tau(297–391) fibrils. Representative negative-stain TEM image of the same preparation as shown above in the 100 µM tau(297-391) HEPES/$MgCl_2$ condition after sonication, showing the shorter fibrillar fragments used as seeds in subsequent aggregation assays. Scale bar: 200 nm.

Under the optimized $MgCl_2$-containing conditions, 100 µM tau(297–391) formed PHF-like fibrils. Subsequent fragmentation generated a preparation containing both shorter fibrillar fragments and longer fibrils, which was used to assess the effect of P12 on seeded tau(297–391) aggregation.

4.6.3. P12 alters tau(297-391) aggregation kinetics under optimized $MgCl_2$ conditions in a concentration-dependent manner.

Having established optimized $MgCl_2$ conditions that supported PHF-like tau(297-391) fibril formation, we next assessed whether P12 influenced tau(297-391) aggregation kinetics in this distinct physicochemical context. Reactions contained 28 µM tau(297-391) and increasing concentrations of P12 ranging from 7 to 56 µM, corresponding to tau(297-391):P12 molar ratios of 4:1, 2:1, 1:1, and 1:2. Tau(297-391)-only and concentration-matched P12-only controls were included, and aggregation was initiated using the fibril-derived tau(297-391) seed preparation described in Section 4.6.2.

Under the optimized conditions, the tau(297-391)-only control displayed a progressive increase in ThT fluorescence after an initial lag phase. Addition of P12 altered this kinetic profile at every concentration tested. Tau(297-391)–P12

reactions entered the fluorescence growth phase earlier than the tau(297-391)-only control and reached substantially higher fluorescence intensities by the end of the observation period (Figure 23).

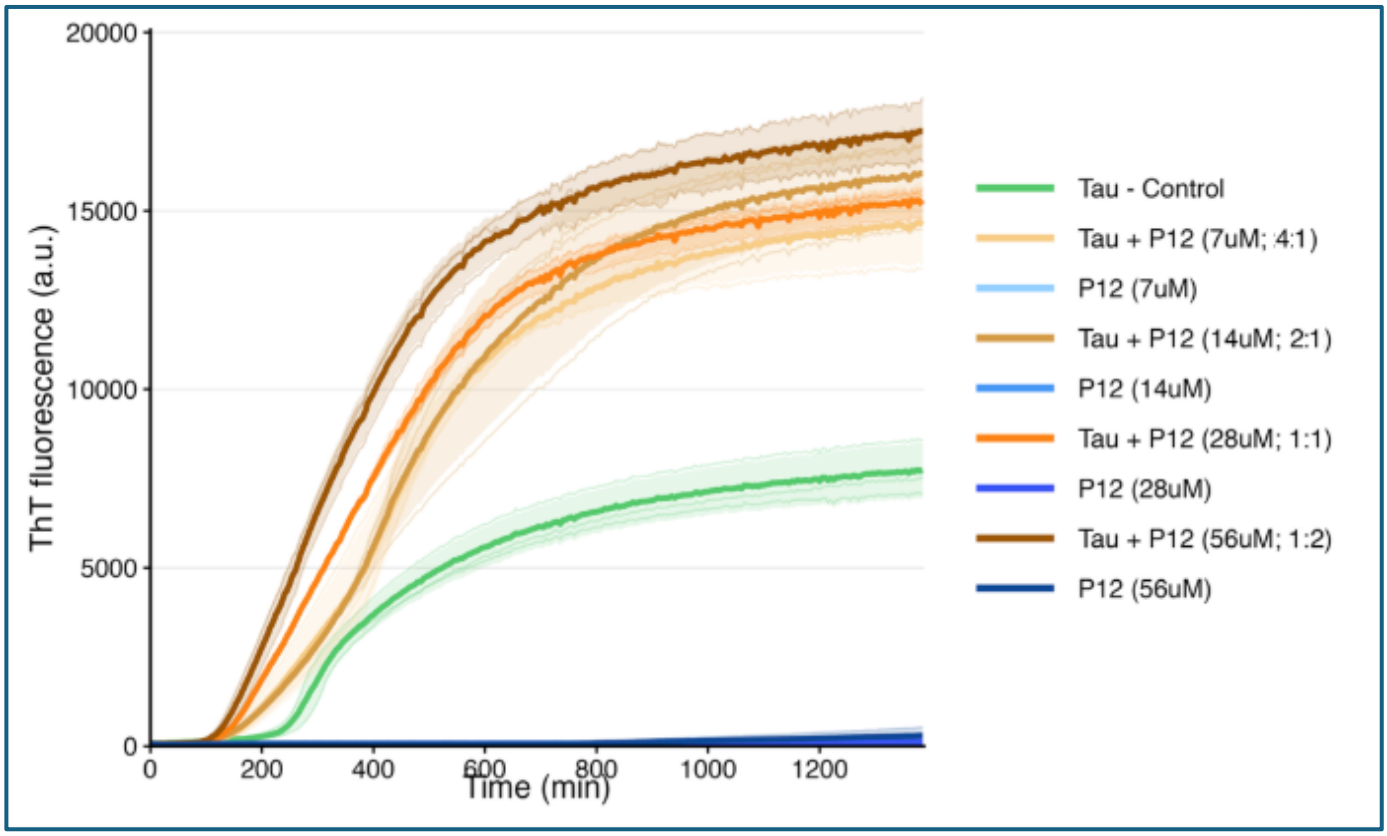


Figure 23. Concentration-dependent effect of P12 on seeded tau(297–391) aggregation under optimized $MgCl_2$ conditions. ThT fluorescence kinetics of 28 µM tau(297–391) incubated alone or with 7, 14, 28, or 56 µM P12. Reactions were performed in 20 mM HEPES, pH 7.4, 200 mM $MgCl_2$, and 2 mM TCEP, using the fibril-derived tau(297-391) seed preparation described in Section 3.3.4.. Individual replicate traces are shown as thin lines, and the corresponding mean profiles are shown as thicker lines.

Within the P12-containing conditions, the clearest concentration-dependent effect was observed during the growth phase. Higher P12 concentrations produced progressively steeper increases in ThT fluorescence, consistent with a faster accumulation of ThT-reactive assemblies once aggregation was initiated. By contrast, differences in the precise onset of fluorescence between the individual P12 concentrations were less clearly resolved and were therefore not interpreted as a robust concentration-dependent trend.

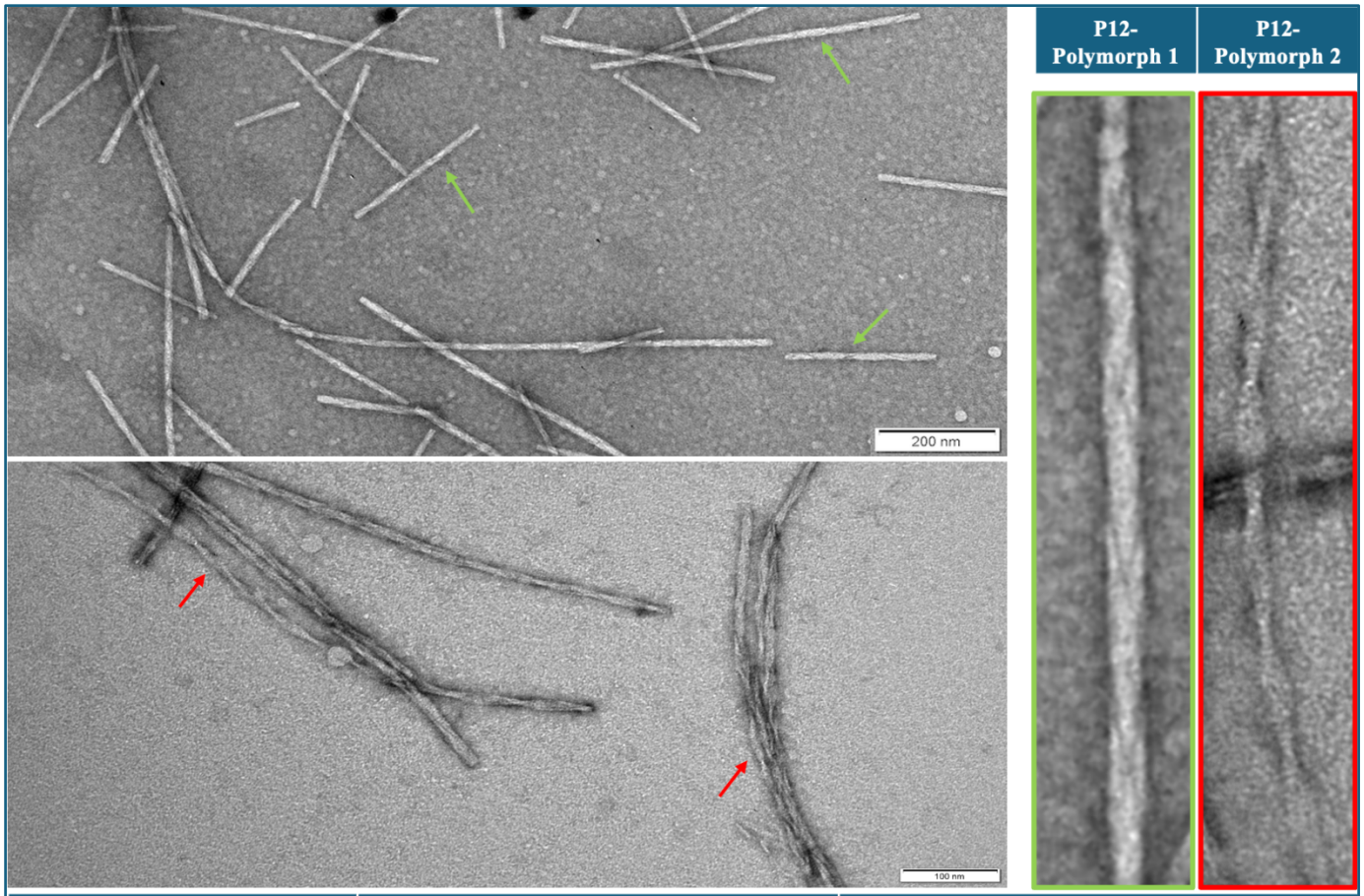
In contrast, none of the concentration-matched P12-only controls showed a detectable increase in ThT fluorescence during the experimental time window, indicating that the fluorescence transition observed in the co-incubation reactions could not be explained simply by an independent ThT-positive aggregation event of P12 under these conditions.

Overall, these results showed that P12 modified seeded tau(297-391) aggregation kinetics under the optimized $MgCl_2$ conditions in a concentration-dependent manner. To assess the morphology of the resulting assemblies, endpoint samples were subsequently examined by negative-stain TEM and compared with tau(297-391)-only and P12-only controls.

4.6.4. Morphological heterogeneity of tau(297-391), P12, and tau(297-391)–P12 assemblies under optimized $MgCl_2$ conditions

Endpoint samples containing 28 µM tau(297-391) alone, 56 µM P12 alone, or both components at the same respective concentrations were examined by negative-stain TEM under the optimized $MgCl_2$ conditions.

The P12-only preparation displayed two recurring fibrillar morphologies. One population consisted of long, thick, predominantly straight fibrils, whereas the other comprised narrower fibrils displaying periodic modulation in width, with crossover distances of approximately 50 nm (Figure 24).

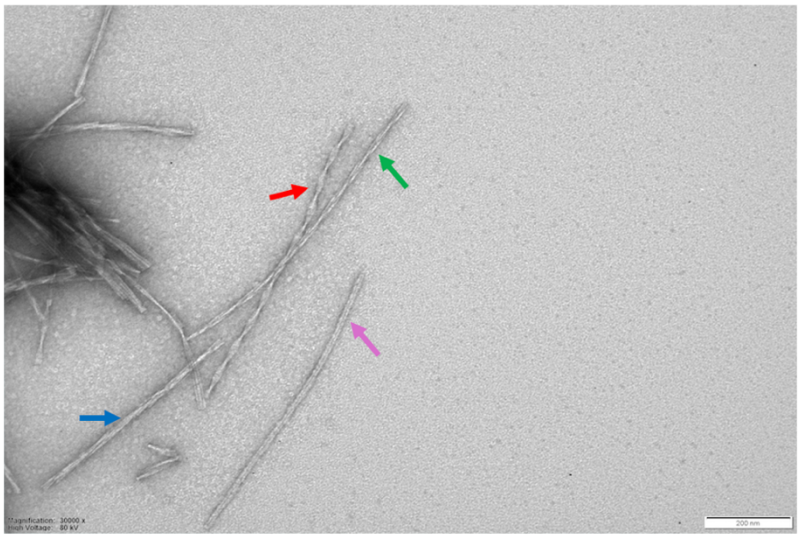


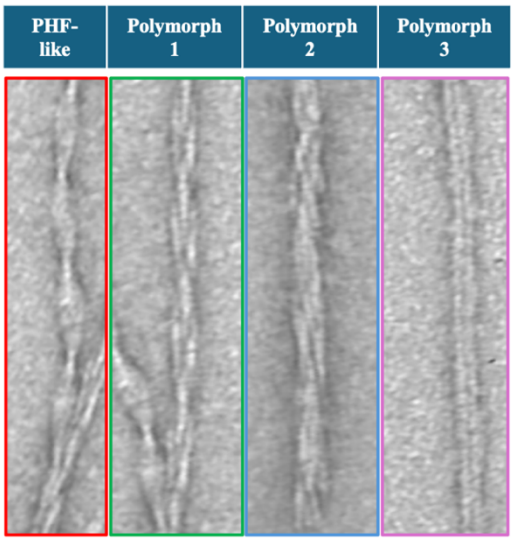
Parameter	P12-Polymorph 1	P12-Polymorph 2
Crossover	/	49.3 +/- 3.75 nm
Max width	15.7 +/- 0.53 nm	14.6 +/- 2.2 nm
Min width	/	6.1 +/- 0.9 nm

Figure 24. Negative-stain TEM characterization of P12 fibril morphologies. Green arrows indicate straight fibrils (Polymorph 1), while red arrows indicate periodically modulated fibrils (Polymorph 2). Representative enlargements and morphometric measurements are shown: fibril width for Polymorph 1 (n = 30) and crossover distance for Polymorph 2 (n = 14). Scale bar: 200 nm top and 100 nm bottom.

By comparison, the tau(297-391)-only sample displayed broader morphological diversity, with several recurring fibril classes distinguishable across the examined regions (Figure 25). These included periodically twisted fibrils with crossover distances within the PHF-like reference range, a second twisted morphology with crossover distances of approximately 100 nm (Polymorph 1), and thicker fibrils lacking an obvious periodic twist (Polymorph 2). Additional

structures consisted of laterally stacked fibrils or morphologies that could not be assigned unambiguously to a defined class (Polymorph 3).



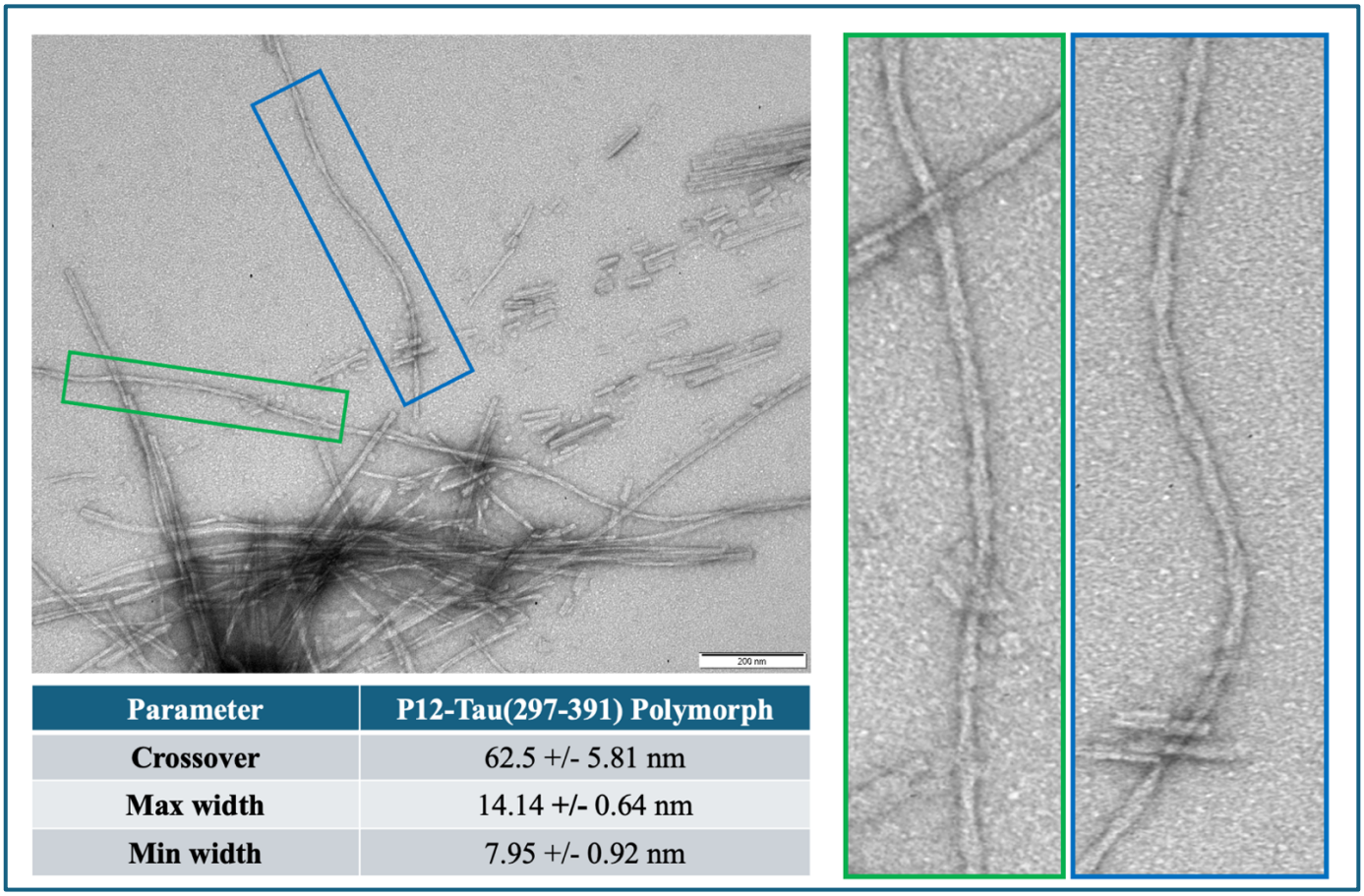


Parameter	PHF-like	Polymorph 1	Polymorph 2	Polymorph 3
Crossover	76.13 +/- 2.51 nm	103 +/- 12.4 nm	/	/
Max width	17.46 +/- 1.72 nm	16.98 +/- 1.1 nm	18.7 +/- 1.92 nm	7.15 +/- 0.5 nm
Min width	8.78 +/- 1.1 nm	9.8 +/- 1.2 nm	/	/

Figure 25. Negative-stain TEM characterization of tau(297–391) fibril morphologies. Colored arrows indicate PHF-like fibrils (red), Polymorph 1 (green), Polymorph 2 (blue), and Polymorph 3 (purple). Crossover distances were measured for PHF-like fibrils (n = 23) and Polymorph 1 (n = 9), while fibril widths were measured for Polymorphs 2 and 3 (n = 20 each). Representative enlargements and corresponding morphometric measurements are shown. Scale bar: 200 nm.

The tau(297–391)–P12 sample displayed several fibrillar morphologies resembling those observed in the individual controls. These included periodically twisted fibrils with crossover distances within the range defined for PHF-like tau(297–391) fibrils, twisted fibrils with crossover distances of approximately 100 nm, clusters of laterally associated straight fibrils, and long, thick fibril (Supplementary Figure S5).

In addition, a subset of fibrils displayed a less clearly defined and less regular periodic twist than the control morphologies. This population had a mean crossover distance of 62.5 ± 5.81 nm (n = 25 crossover measurements) (Figure 26). Fibrils with the approximately 50 nm crossover distance observed in the P12-only control were not identified in the screened samples and examined grid regions.



Parameter	P12-Tau(297-391) Polymorph
Crossover	62.5 +/- 5.81 nm
Max width	14.14 +/- 0.64 nm
Min width	7.95 +/- 0.92 nm

Figure 26. Negative-stain TEM images of a distinct fibril subset observed in the tau(297–391)–P12 co-incubation sample. The images highlight fibrils displaying an apparently distinct crossover periodicity that was not observed in either the tau(297–391)-only or P12-only control samples under the conditions examined. Minimum and maximum fibril widths and crossover distances are indicated where measurable (n = 25). Scale bar: 200 nm (left panel).

Although the twist remained visible along these fibrils, successive crossover distances were less uniform and displayed greater variability than in the corresponding control morphologies.

4.7. Preliminary cryo-EM evaluation of tau(297-391) and tau(297-391)–P12 fibrillar samples

4.7.1. Screening of grid supports and vitrification parameters using tau(297-391) fibrils

An initial grid-screening strategy was performed using a tau(297-391) fibril preparation. The objective was to identify a combination of grid support and vitrification parameters that provided sufficiently thin vitreous ice, retained an adequate fibril density within imageable regions, and minimized fibril stacking, bundling, and large-scale clustering.

Several experimental variables were evaluated, including grid support, the presence or absence of an additional carbon-based coating, blotting orientation, sample volume, relative humidity, temperature, and blotting time. The principal grid supports screened included UltrAuFoil, Lacey carbon, and Quantifoil grids (Figure 27). The vitrified grids were examined by cryo-EM to assess ice thickness, fibril density and distribution, localization within the grid holes, and the degree of separation between individual fibrils.

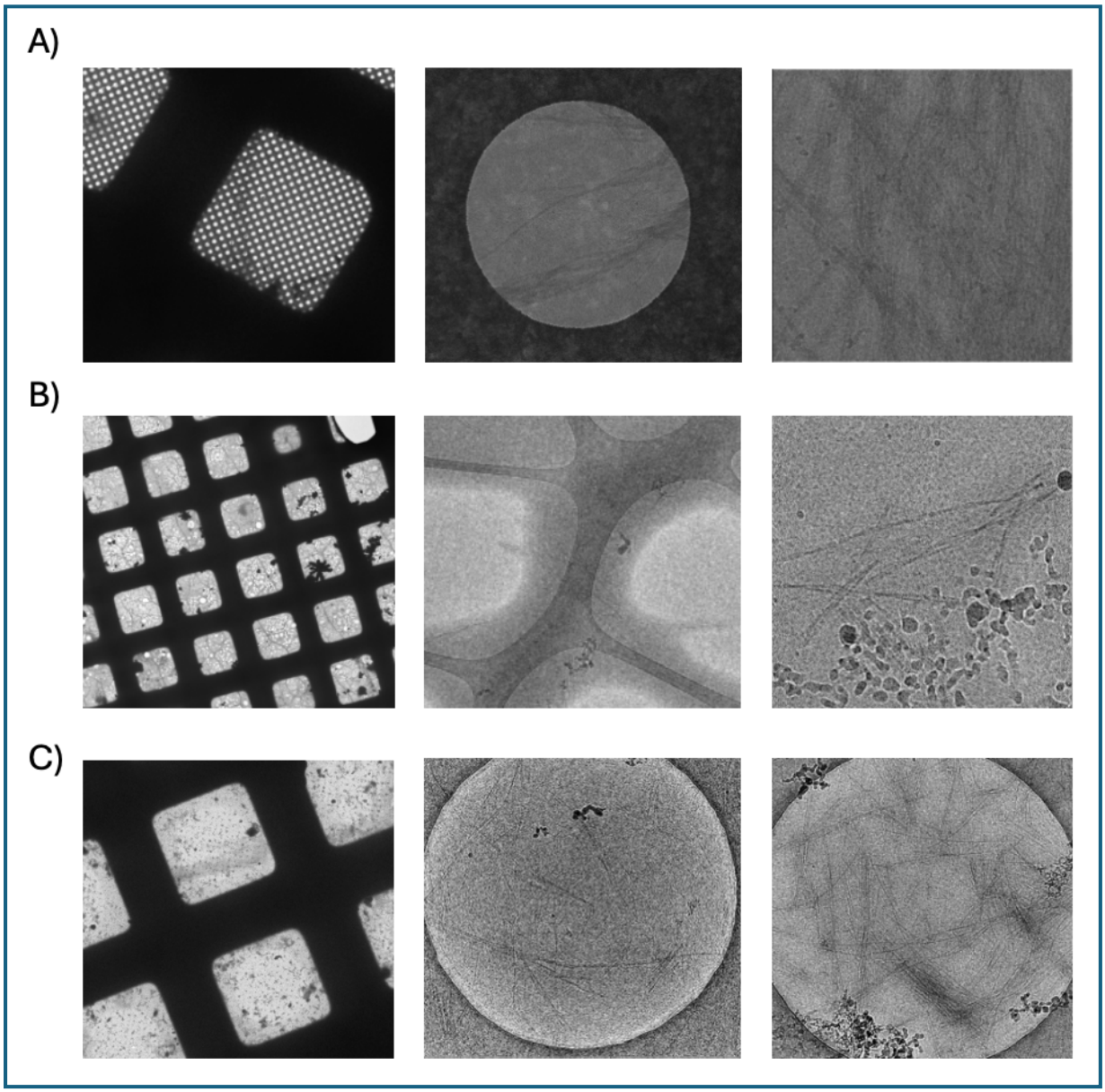


Figure 27. Screening of cryo-EM grid supports using tau(297–391) fibrils. (A) UltrAuFoil R2/2 Au 200-mesh grid showing uneven fibril distribution and densely clustered regions. **(B)** Lacey carbon 300-mesh copper grid showing comparatively well-dispersed fibrils at low overall density. Higher-magnification images in panels A and B were acquired at 100,000× magnification. **(C)** Quantifoil R2/1 300-mesh copper grid showing fibrils distributed within regions of suitable ice thickness.

UltrAuFoil R2/2 Au 200-mesh grids displayed a markedly uneven fibril distribution. Large accumulations of fibrillar material were observed in some regions, whereas other regions contained no detectable fibrils. Within the fibril-rich areas, the filaments were frequently stacked or densely clustered, making individual fibrils difficult to distinguish and limiting the number of regions potentially suitable for high-resolution data acquisition (Figure 27 A).

Lacey carbon 300-mesh copper grids produced a more homogeneous distribution of fibrillar material across the grid. Long fibrils were observed extending through regions containing sufficiently thin ice, and individual fibrils were generally less densely clustered than on the UltrAuFoil grids. However, the overall fibril density remained low, with relatively few fibrils present within imageable regions. (Figure 27 B).

Quantifoil R2/1 300-mesh copper grids initially displayed relatively thick ice across a substantial proportion of the grid. Nevertheless, regions with suitable ice thickness contained a comparatively high density of fibrils. In these areas, the filaments extended across the holes with limited clumping to allow individual fibrils to be visualized (Figure 27 C).

Among the supports tested, Quantifoil R2/1 therefore provided the most promising balance between fibril density and separation. This grid type was selected for further optimization using the tau(297-391)–P12 co-incubation sample.

4.7.2. Identification of a tau(297-391)–P12 grid suitable for future data collection

The grid conditions selected during the initial tau(297-391) fibril screening were subsequently applied to a freshly prepared tau(297-391)–P12 sample generated using the optimized $MgCl_2$-based aggregation protocol established above. The reaction contained 28 µM tau(297-391), 56 µM P12, 20 mM HEPES at pH 7.4, 200 mM $MgCl_2$, 2 mM TCEP and 20 µM ThT. The sample was vitrified after approximately 20 h of incubation, at a time point corresponding to the rising phase of the ThT fluorescence curve. The aggregation kinetics recorded for this sample are provided in the Supplementary Information (Supplementary Figure S6).

Quantifoil R2/1 300-mesh copper grids were evaluated with or without a graphene oxide coating. The coating was introduced as an additional support intended to improve fibril adsorption and retention during grid preparation. Four grids were prepared by combining the presence or absence of graphene oxide with blotting times of 3 or 4 s. The remaining vitrification parameters were maintained constant, using a 3 µL sample volume, front-side blotting, 95% relative humidity, and a 30 s waiting period between sample application and blotting.

Screening revealed substantial differences between the four grid preparations. Among the conditions tested, the graphene oxide-coated Quantifoil R2/1 grid prepared using a 3 s blotting time produced the most favorable fibril distribution. Fibrillar material was detected across numerous regions containing ice of suitable thickness. Although some filaments remained locally organized into small clusters, individual fibrils could frequently be distinguished within them (Figure 28 B).

Higher-magnification imaging revealed several fibrils with sufficiently clear outlines and limited overlap to permit morphological inspection (Figure 28 C). The observed fibril distribution and separation indicated that this grid represented the most promising candidate generated during the screening for subsequent data acquisition.

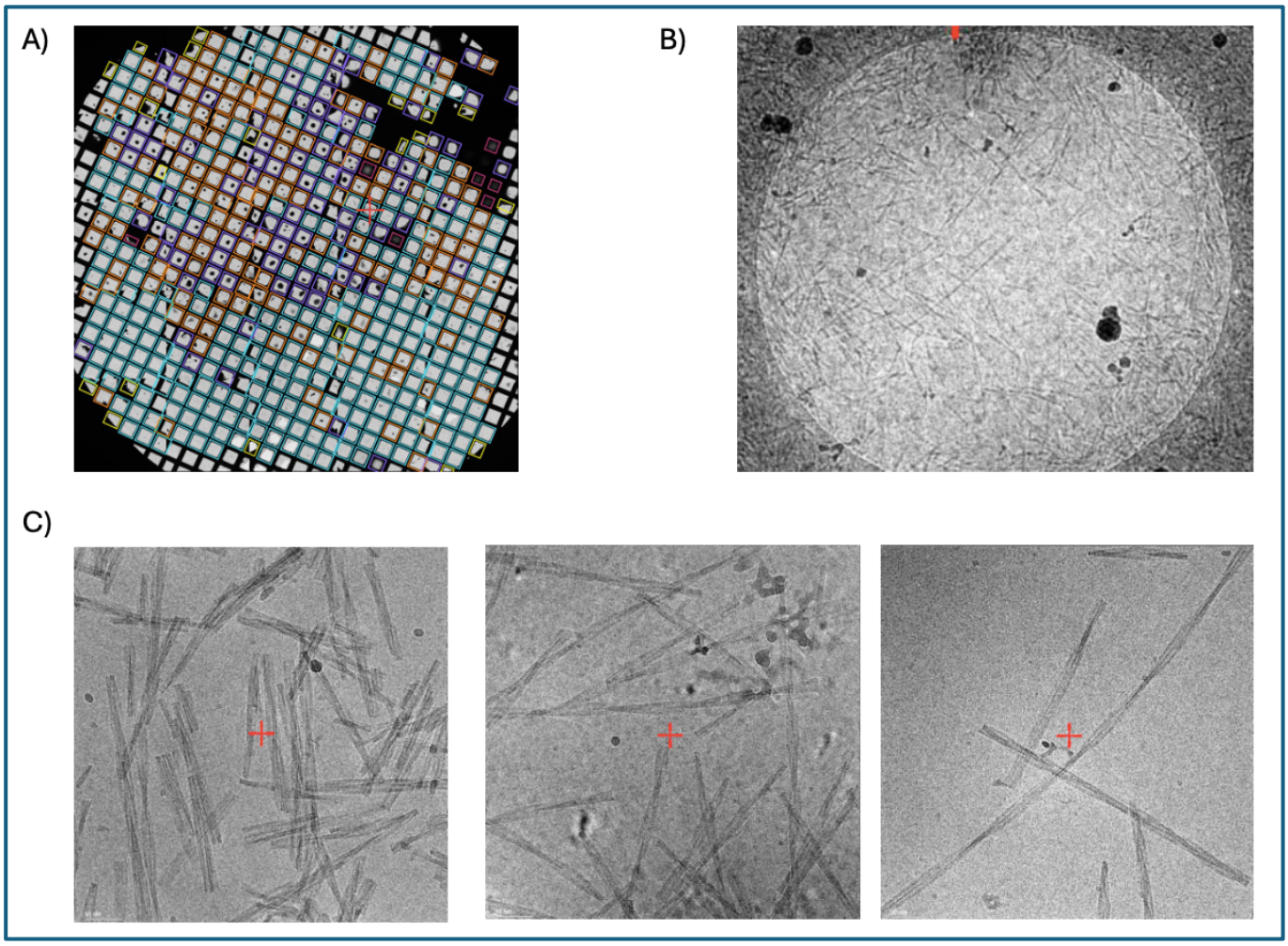


Figure 28. Cryo-EM imaging of the optimized tau(297–391)–P12 grid. (A) Atlas magnification tiling of the graphene oxide-coated Quantifoil R2/1 grid. **(B)** Representative grid region. **(C)** Images acquired at 100,000× magnification showing fibrillar material with varying degrees of dispersion and overlap.

Overall, the two-stage screening strategy identified a graphene oxide-coated Quantifoil R2/1 300-mesh copper grid, combined with a 3 s front-blotting step, as the most suitable condition tested for vitrification of the tau(297-391)–P12 fibril preparation.

4.8. Development of a dual-size nanogold strategy to investigate tau(297-391)–P12 spatial organization within fibrillar assemblies

4.8.1. Synthesis and functional validation of biotinylated P12 derivatives

To visualize P12 distribution in individual fibrillar structures, a biotin–streptavidin nanogold strategy was developed using biotinylated P12 derivatives and streptavidin-conjugated gold particles.

A series of biotinylated P12 derivatives was generated by Fmoc-based solid-phase peptide synthesis as described in section 3.2.2. The designs were based on the original P12 sequence and explored different strategies for biotin incorporation, including extensions containing additional residues derived from the native TRA2B sequence. Following synthesis, the products were analyzed by LC–MS to assess whether peptides with the expected molecular masses had

been obtained. The complete sequences and designs of the synthesized peptides, together with their calculated molecular masses, are presented in Supplementary Note S2, while the corresponding LC–MS spectra and experimentally determined molecular masses are provided in Supplementary Figure S7.

Among the derivatives tested, only two yielded LC–MS profiles compatible with successful synthesis of the intended biotinylated products. These corresponded to P12-Biotin and a second construct containing a four-residue extension derived from the native TRA2B sequence followed by biotin (hereafter termed P12-RSRG-Biotin). The remaining derivatives did not produce LC–MS profiles consistent with the expected products and were therefore excluded from further experiments.

Because the addition of biotin or sequence extensions could alter the aggregation behavior of P12, the two validated derivatives were first evaluated by ThT assay before being used as imaging probes. Each derivative was incubated at 56 µM with 28 µM tau(297–391) under the previously established aggregation conditions, while the corresponding peptide-only controls were analyzed in parallel at the same peptide concentrations (Figure 29).

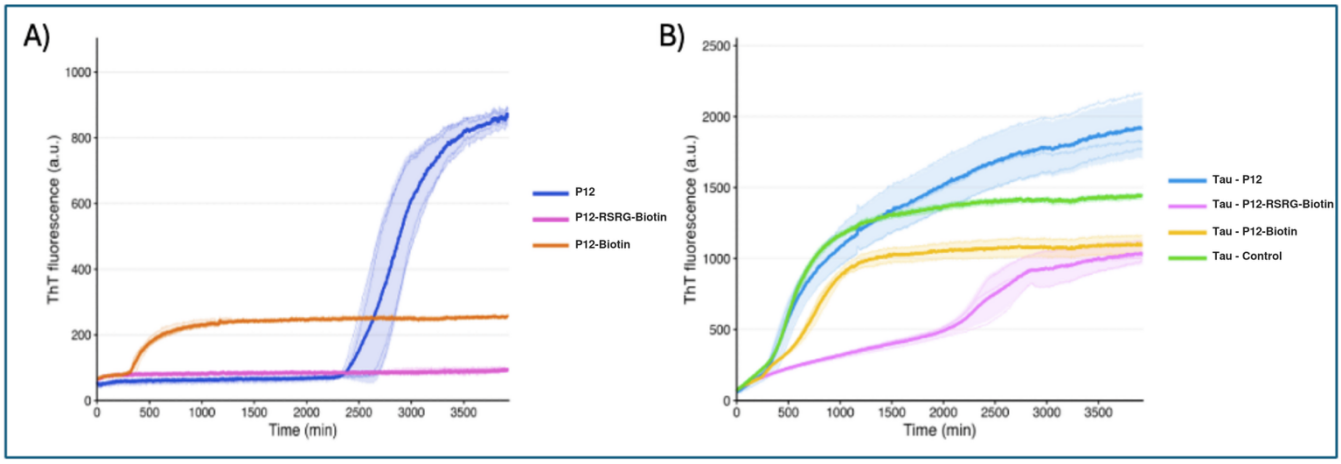


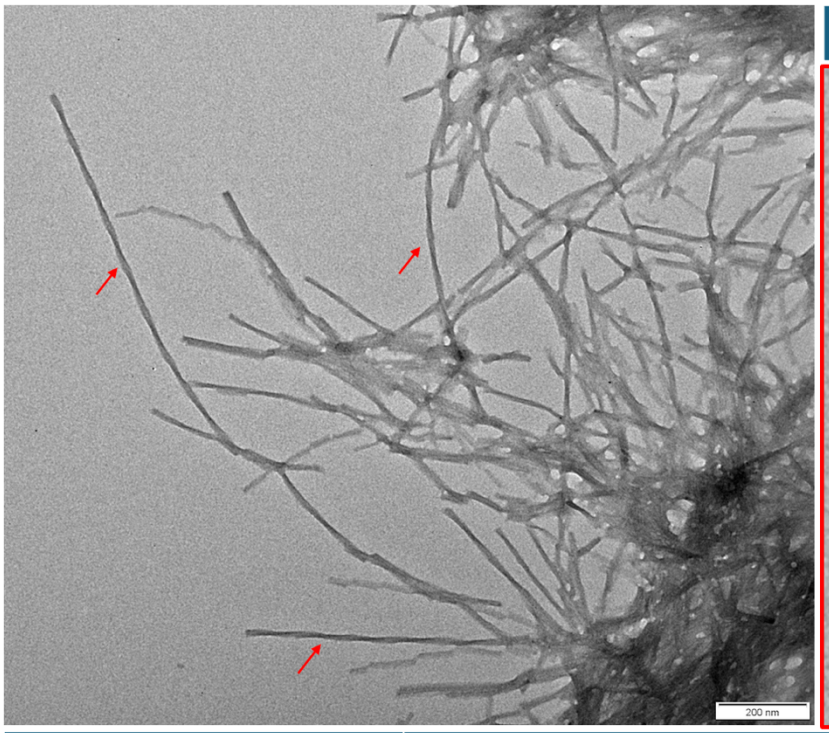
Figure 29. ThT fluorescence assay of P12 and biotinylated P12 derivatives. (A) ThT fluorescence profiles of P12, P12-Biotin, and P12-RSRG-Biotin alone. **(B)** Corresponding profiles in the presence of tau(297–391), compared with the tau(297–391)-only control. Bold lines represent mean ThT fluorescence profiles, with individual replicates shown in lighter shades.

Both biotinylated derivatives remained compatible with altered ThT behavior in the presence of tau(297-391), although their individual profiles differed (Figure 29 B). For P12-Biotin, the peptide-only control displayed a clear ThT-positive transition, whereas the corresponding tau(297-391)–P12-Biotin co-incubation produced a distinct kinetic profile. Nevertheless, its co-incubation with tau(297-391) produced a ThT profile that differed from the corresponding tau(297-391)-only control, suggesting that the derivative may still influence the aggregation behavior of tau(297-391).

Among the validated constructs, P12-Biotin was selected for subsequent nanogold-labeling experiments. This derivative retained a suitable aggregation profile in the presence of tau(297-391) while introducing the smallest modification to the original P12 sequence, thereby providing the most direct probe for assessing the spatial relationship between P12 and tau(297-391) fibrillar assemblies.

4.8.2. Optimization of nanogold labeling for spatial analysis of tau(297-391)–P12-derived peptide fibrillar assemblies

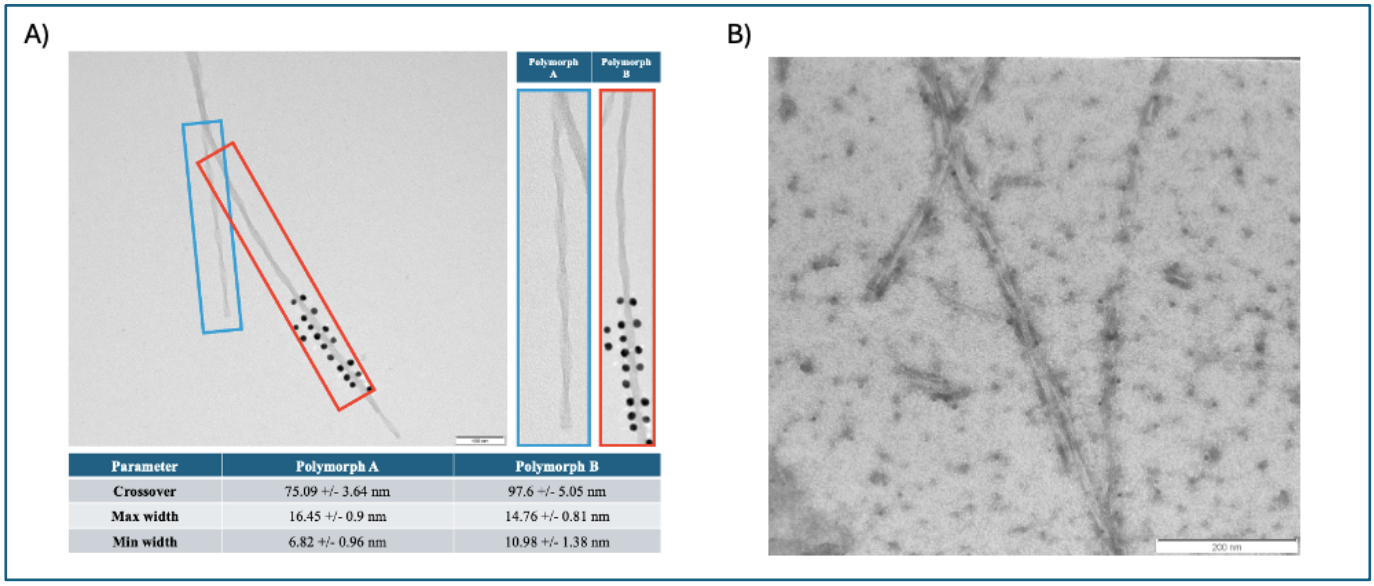
Following the selection of P12-Biotin as the most suitable probe, its fibrillar morphology was first examined independently to provide a reference for the subsequent labeling experiments. P12-Biotin was incubated alone at 56 µM under the optimized $MgCl_2$-based conditions, and the resulting sample was analyzed by negative-stain TEM. The preparation contained twisted fibrils displaying a crossover length of approximately 100 nm (Figure 30).



Parameter	P12-Biotin Polymorph 1
Crossover	102.36 +/- 5.8 nm
Max width	17.43 +/- 1.3 nm
Min width	10.35 +/- 1.1 nm

Figure 30. Negative-stain TEM characterization of P12-Biotin fibrils. Red arrows indicate twisted fibrils, with a representative enlargement shown on the right. Corresponding crossover lengths and maximum and minimum fibril widths are reported below (n = 15). Scale bar: 200 nm.

Tau(297–391) and P12-Biotin were then co-incubated at concentrations of 28 µM and 56 µM, respectively, under the same conditions. The resulting assemblies were incubated with 15 nm streptavidin-conjugated nanogold to assess the accessibility of the biotin and detect P12-Biotin on fibrillar material. TEM examination revealed 15 nm gold particles associated with a subset of fibrils (Figure 31). A substantial proportion of the labeled fibrils displayed periodic width modulation and crossover distances overlapping with those of a polymorph observed in both tau(297-391)-only and P12-Biotin-only samples. Because these morphologies could not be reliably distinguished, the presence of P12-Biotin on the labeled fibrils could be established, but whether these structures also contained tau(297-391) could not be determined.



Parameter	Polymorph A	Polymorph B
Crossover	75.09 +/- 3.64 nm	97.6 +/- 5.05 nm
Max width	16.45 +/- 0.9 nm	14.76 +/- 0.81 nm
Min width	6.82 +/- 0.96 nm	10.98 +/- 1.38 nm

Figure 31. Nanogold labeling of fibrillar material generated by tau(297–391)–P12-Biotin co-incubation. (A) Representative TEM image showing 15 nm streptavidin-conjugated nanogold particles associated with fibrillar material. Boxed regions are enlarged, and the corresponding morphometric measurements are summarized below. **(B)** Representative dual-size nanogold-labeling preparation displaying extensive background, which prevented reliable assignment of tau(297-391)- and P12-directed particles to individual fibrils. Scale bars: 100 nm (A) and 200 nm (B).

Having established that streptavidin–nanogold could detect P12-Biotin on fibrillar material, a dual-labeling strategy was subsequently tested to visualize P12 and tau(297-391) simultaneously. This approach combined streptavidin-conjugated nanogold targeting P12-Biotin with antibody-based nanogold labeling of tau(297-391) fibrils using a second distinguishable gold-particle size. Under the conditions tested, however, the dual-labeling preparations displayed extensive background labeling, with numerous gold particles distributed throughout the grid and surrounding the fibrillar material (Figure 31 B). This background prevented reliable assignment of individual particles to fibrils and therefore precluded interpretation of potential tau(297-391)–P12 colocalization. Further optimization of blocking, washing, reagent concentrations, and labeling conditions was therefore required before the dual-size strategy could be used to assess spatial association.

5. Discussion

Previous work from the SwitchLab identified TRA2B as a potential modulator of Tau pathology and showed that its dual aggregation-prone region, represented by P12, can modify tau(297-391) aggregation kinetics and enhance tau(297-391) seeding. However, these observations were obtained under aggregation conditions that predominantly generated short fibrillar fragments, limiting the possibility of investigating how P12 interacts with and potentially influences the organization of mature fibrils.

A major objective of the present study was therefore not simply to reproduce the previously observed kinetic effect, but to determine whether it persists under conditions supporting the formation of extended tau(297-391) fibrils suitable for morphological and structural investigation. Using a reductionist tau(297-391)/P12 system, P12-dependent modulation was observed both under NaCl conditions producing long, predominantly ribbon-like and laterally associated fibrils, and under optimized $MgCl_2$ conditions supporting PHF-like tau(297-391) morphologies. This extends the previous functional observations by showing that the influence of P12 is maintained across distinct fibrillar assembly conditions rather than being restricted to those producing short fragmented species. Within this framework, the present results support three main conclusions. First, P12 modifies the aggregation behavior of tau(297-391) in conditions compatible with the formation of extended fibrillar assemblies, although the manifestation of this effect depends strongly on P12 concentration and on the physicochemical environment. Second, the assembly state of P12 itself appears relevant, since preformed P12 assemblies were able to promote the emergence of a tau(297-391)-associated ThT response in NaCl conditions. Third, biochemical and imaging observations indicate that P12-derived material can partition with, and associate with, fibrillar material formed during tau(297-391)–P12 co-incubation. Nevertheless, the present data do not establish whether P12 is incorporated into the ordered tau(297-391) fibril core, associates predominantly with fibril surfaces or ends, or influences tau(297-391) assembly through transient interactions. The findings therefore support a model in which heterotypic interactions between P12 and tau(297-391) influence fibrillar assembly, while leaving the precise molecular organization of the resulting structures unresolved.

5.1. P12 is a condition-dependent modulator of tau(297-391) assembly

The clearest conclusion from the kinetic experiments is that P12 changes the behavior of the tau(297–391)-containing aggregation system. However, this effect cannot be described as a simple relationship in which increasing P12 concentrations uniformly accelerate every stage of tau(297-391) aggregation.

Under the initial NaCl-based conditions, reactions containing relatively low P12 concentrations more frequently developed detectable ThT responses than the corresponding tau(297–391)-only controls (Figure 12). Nevertheless, the timing and amplitude of these responses varied considerably between technical replicates, preventing the establishment of a reproducible concentration-dependent relationship. Such variability is compatible with the stochastic nature of amyloid nucleation and with the sensitivity of aggregation assays to differences in seed delivery, local sample conditions, and the availability of aggregation-competent species [19]. These observations therefore suggest that P12 may increase the likelihood of detectable assembly under the NaCl conditions, but they do not demonstrate a consistent shortening of the lag phase throughout the initial concentration range.

A subsequent titration performed under the same NaCl-based conditions, in which P12 was increased from 14 to 56 µM, suggested that the direction of the P12 effect may differ between lower and higher peptide concentrations. In particular, the 14 µM P12 condition was associated with a later fluorescence increase relative to tau(297–391) alone (Figure 13), whereas a higher concentration produced an earlier major transition. Although this observation may suggest an inhibitory effect of P12 at low concentration, additional independent biological replicates would be required before such a conclusion could be drawn. The data therefore support the possibility of different concentration-dependent regimes but do not establish a reproducible inhibitory effect.

Interpretation of the higher-concentration NaCl experiments, covering 28–168 µM P12, was further complicated by the appearance of an early ThT-positive transition in tau(297–391)–P12 reactions at all concentrations except 28 µM P12. At the highest P12 concentration, the close temporal correspondence between this early transition and the response observed for P12 alone suggested that the initial fluorescence increase arose predominantly from P12 self-assembly. This assignment should nevertheless be interpreted cautiously, because ThT reports the appearance of sufficiently ordered amyloid-like binding sites rather than the earliest stages of peptide association. P12-derived oligomeric or prefibrillar species may therefore already have been present before a distinct ThT transition became detectable. Consequently, at these higher concentrations, the system cannot be considered as containing exclusively soluble P12, and the resulting fluorescence profiles may instead reflect contributions from several P12 assembly states [56].

The optimized $MgCl_2$-based conditions provided a complementary context. Under these conditions, P12-containing reactions developed an earlier ThT response than tau(297-391)-only control, while increasing P12 concentrations were associated with progressively steeper fluorescence increases during the growth phase. Importantly, the most consistent concentration-dependent effect concerned the rate of signal increase after aggregation had begun, rather than a clearly resolved progressive shortening of the lag phase between each individual P12 concentration. In contrast to the NaCl experiments, however, concentration-matched P12-only controls remained close to baseline during the observation period and no clearly separated early P12-associated transition was detected. The $MgCl_2$ profiles were therefore not confounded by an independently detectable, strongly ThT-positive P12 transition, although the presence of weakly ThT-reactive P12 assemblies cannot be excluded.

The differences between the NaCl- and $MgCl_2$-based experiments indicate that the effects of P12 depend on the experimental environment. Ionic composition can influence electrostatic screening, conformational equilibria, intermolecular interactions, fibril stability, and polymorph selection, all of which may modify the behavior of an amyloid-forming system [28; 31]. However, comparison between these conditions does not identify which individual parameter is responsible for the observed differences, nor can an earlier fluorescence increase, or a steeper growth phase be assigned directly to a specific microscopic process. Together, the kinetic experiments therefore identify P12 as a condition-dependent modulator of the tau(297–391)-containing aggregation system while leaving unresolved whether the relevant P12 species is soluble, assembled, or a combination of both.

5.2. The assembly state of P12 may contribute to promotion of tau(297-391) aggregation

To test whether preassembled P12 could functionally contribute to the tau(297–391)-containing aggregation response, independently prepared P12 assemblies were added to tau(297–391). Under these conditions, ThT-positive responses developed whereas the corresponding tau(297–391)-only reactions remained negative over the same observation period. Although no consistent quantitative relationship between P12 seed concentration and aggregation rate could be established, this experiment provides preliminary evidence that preparations containing preassembled P12 can promote the emergence of ThT-reactive material in a tau(297–391)-containing system. However, this result does not demonstrate that the assembled P12 species themselves were solely responsible for the effect, particularly if residual soluble peptide remained present in the seed preparation.

This result is particularly relevant because it expands the possible mechanism beyond a simple interaction between soluble P12 and soluble tau(297-391). An amyloid or amyloid-like assembly presents repetitive molecular surfaces and fibril ends that may differ substantially from those accessible in the monomeric peptide [57]. Several non-mutually exclusive mechanisms could therefore account for the observed effect. P12 assemblies could promote tau(297–391) aggregation by modifying the physicochemical environment surrounding the protein without acting as a direct structural template. For example, transient adsorption of tau(297–391) onto P12-derived surfaces could increase its local concentration, favor interactions between neighboring tau(297–391) molecules, or alter the conformational states available to the protein. These surfaces might also modify local electrostatic interactions or solvent exposure, thereby creating conditions more favorable for tau(297–391) self-association. Under this scenario, tau(297–391) aggregation would be facilitated by proximity to P12 assemblies but would not necessarily involve elongation from P12 fibril ends, incorporation of P12 into the resulting fibrils, or propagation of a P12-derived structural arrangement. Heterotypic cross-seeding nevertheless remains one possible interpretation, but the present data are insufficient to establish it [58]. The distinction may nevertheless be biologically relevant. Preliminary observations from SwitchLab indicate that TRA2B has its strongest effects in seeded Tau contexts, including enhancement of relatively weak Tau seeding activity. The current reductionist experiments provide a possible molecular parallel to this behavior: the aggregation state of one interacting partner may influence the threshold at which Tau becomes assembly competent. Although direct extrapolation from P12 to full-length TRA2B is premature, these results support the broader hypothesis that heterotypic amyloid interactions may depend not only on sequence identity but also on the physical state of the interaction partner.

5.3. P12 associates with fibrillar material, but its molecular location remains unresolved

Kinetic modulation alone does not establish whether P12 remains associated with the assemblies that form. The LC–MS solubility experiment therefore provided an important second level of evidence. Under seeded NaCl conditions associated with tau(297-391) aggregation, depletion of soluble tau(297-391) was accompanied by a smaller but concomitant depletion of P12. By comparison, conditions lacking a substantial ThT response retained much larger

soluble fractions of both components. These results indicate that P12 partitioning into sedimentable material is linked to conditions in which tau(297-391) assembly occurs.

This observation argues against a model in which P12 acts exclusively through a transient interaction and necessarily remains fully soluble throughout aggregation. However, co-depletion does not demonstrate molecular co-assembly. Tau(297-391) and P12 could become incorporated into the same fibrils, form separate aggregates that sediment under the same centrifugation conditions, associate through fibril surfaces or higher-order bundles, or partition into distinct non-fibrillar insoluble species. The solubility experiments therefore provide biochemical evidence of aggregation-associated P12 partitioning rather than direct proof of heterotypic fibril formation.

Negative-stain TEM added morphological information but also reinforced this ambiguity. Under the optimized $MgCl_2$ conditions, P12 alone was capable of forming fibrillar structures, including relatively thick straight fibrils and a population of narrower fibrils displaying a periodicity of approximately 50 nm. Tau(297-391) alone was itself polymorphic, containing PHF-like fibrils as well as laterally associated straight fibrils and other morphologies. Consequently, the heterogeneity observed in tau(297-391)–P12 co-incubation samples cannot be interpreted simply by assigning every fibril to one component.

Nevertheless, one observation was particularly intriguing. In addition to morphologies overlapping with the tau(297-391)- and P12-only controls, the co-incubation sample contained a recurring fibrillar population with a comparatively irregular periodic modulation and a mean crossover distance of approximately 62 nm. This periodicity was intermediate between the approximately 50 nm population observed for P12 alone and the approximately 75–80 nm PHF-like Tau reference. Such an intermediate morphology is compatible with the possibility that the presence of P12 modifies the distribution of accessible fibrillar states. It does not, however, establish the existence of a hybrid tau(297-391)–P12 fibril. The same morphology could arise from an alternative tau(297–391) polymorph, a distinct P12 polymorph, or from an indirect influence of one component on the assembly pathway of the other without stable co-incorporation into the same fibril.

The nanogold experiments were designed to move beyond this compositional uncertainty. Streptavidin-conjugated nanogold particles could be detected on fibrillar material formed using P12-Biotin, demonstrating that the labeled P12 derivative was physically associated with at least a subset of fibrillar structures. This represents a more direct localization of P12-derived material than either LC–MS or conventional TEM. However, the dual-size experiment intended to identify P12 and tau(297-391) simultaneously on the same fibrils displayed substantial nonspecific background, preventing reliable assignment of the two gold populations to the same continuous fibrils. Therefore, the present nanogold data demonstrate localization of P12-Biotin on fibrillar material, but not definitive tau(297-391)–P12 colocalization.

Interpretation is further complicated by the fact that P12-Biotin did not behave identically to unmodified P12. Although it remained capable of participating in a ThT-positive tau(297–391)-containing reaction, its transition occurred earlier and its overall fluorescence amplitude was considerably lower than that observed with native P12. In addition, TEM analysis revealed a recurring fibrillar morphology in P12-Biotin samples that was not observed in the corresponding

unmodified P12 preparations, further suggesting that the biotin modification can alter the assembly behavior and accessible fibrillar states of the peptide. P12-Biotin should therefore be regarded primarily as a localization probe rather than as a fully neutral substitute for unmodified P12.

Taken together, LC–MS, TEM and nanogold provide increasingly direct evidence that P12 becomes associated with the fibrillar phase of the system. However, they stop short of defining its molecular position. P12 could reside on fibril surfaces, bind to fibril ends, remain in flexible peripheral regions or become incorporated within the same fibrils as tau(297-391). Incorporation into the ordered amyloid core remains a substantially stronger claim and cannot be established by the current data.

5.4. The reaction environment shapes tau(297-391) fibril morphology and the manifestation of the P12 effect

A second major outcome of this study concerns the strong dependence of tau(297-391) fibril morphology on the effective aggregation environment. This aspect initially emerged as a technical difficulty when published $MgCl_2$-based conditions failed to reproducibly generate the expected PHF-like morphology in our hands. However, the subsequent identification and correction of the underlying solution conditions transformed this observation into a broader mechanistic point relevant to amyloid polymorphism.

The initial NaCl conditions illustrate the distinction between efficient aggregation and formation of a structurally relevant fibril morphology. These conditions generated robust ThT responses and abundant fibrillar material, making them suitable for investigating kinetic modulation by P12. Yet tau(297-391)-only samples were dominated by long, relatively straight fibrils arranged in dense lateral bundles rather than by a substantial population of PHF-like structures. Thus, a condition that performs well in a kinetic aggregation assay does not necessarily produce the fibrillar architecture most relevant to the structural question being asked.

This distinction became even clearer during attempts to reproduce published tau(297-391) PHF-forming protocols. Despite testing several literature-derived combinations of tau(297-391) concentration, $MgCl_2$ concentration, agitation and vessel geometry, the initial preparations predominantly generated broad ribbons, bundled straight fibrils or irregular assemblies. Because tau(297-391) has previously been shown to generate PHF-like and Alzheimer-fold-related fibrils under defined conditions [50; 51; 59], the repeated discrepancy suggested that an unrecognized variable rather than an intrinsic inability of the construct was redirecting assembly.

The incompatibility observed between phosphate and $MgCl_2$ provided one plausible explanation. Visible turbidity and precipitation indicated that the nominal buffer composition did not necessarily correspond to the effective chemical environment experienced by tau(297–391). Magnesium–phosphate precipitation could alter the free concentrations of both species and compromise phosphate buffering [55], while the experimentally observed pH changes indicated that reactions nominally prepared near pH 7.4 could in practice experience substantially more acidic conditions. This was

particularly relevant because the initial screening had already shown strongly reduced or undetectable tau(297–391) aggregation at lower pH values.

Protein preparation may have provided an additional source of variability. The tau(297–391) used in this study was purified by RP-HPLC in the presence of TFA and subsequently lyophilized. Residual counterions or the protonation state of the preparation could therefore have influenced the final reaction environment upon redissolution, particularly at the relatively high tau(297–391) concentrations used in PHF-forming protocols [60]. This contribution was not directly quantified and should therefore remain a working explanation rather than a demonstrated mechanism. Nevertheless, the independent recovery of PHF-like morphology after either replacing phosphate with HEPES or desalting tau(297–391) before aggregation strongly supports the broader conclusion that control of the effective solution environment was critical.

These findings are consistent with the general concept of amyloid polymorphism introduced earlier in this thesis. A protein sequence does not encode a single defined fibrillar structure; instead, the structural outcome emerges from the interaction between sequence-encoded propensities and the molecular environment encountered during assembly [28; 31]. Small changes in pH, ionic composition, counterions or protein preparation may alter the relative accessibility or stability of competing assembly pathways. The difficulty in reproducing apparently similar literature conditions therefore does not necessarily imply poor reproducibility of the original observations. Even when the reported concentrations are the same, differences in protein preparation or in the actual chemical conditions of the solution may be sufficient to change the fibrils that form, particularly in an amyloid system that is highly sensitive to its environment.

The recovery of fibrils displaying the expected width modulation and crossover range provided an experimentally useful PHF-like reference for subsequent tau(297-391)–P12 comparisons. However, morphology must remain distinct from molecular fold. Negative-stain TEM cannot resolve side-chain packing, β-sheet registry or protofilament architecture. Consequently, even fibrils with crossover distances and widths closely matching published PHF-like values cannot be described as adopting the Alzheimer Tau fold without high-resolution structural confirmation [53].

5.5. A working mechanistic model for the tau(297-391) –P12 interaction

The combined observations suggest that no single mechanism is currently sufficient to explain the behavior of the tau(297-391)–P12 system. Instead, P12 may influence tau(297-391) aggregation through several non-mutually exclusive interactions whose relative contributions depend on concentration, assembly state and physicochemical environment.

A first possible mechanism is that heterotypic interactions between P12 and tau(297-391) alter the conformational ensemble sampled by tau(297-391) before productive assembly. Through transient contacts involving their aggregation-prone regions, P12 could preferentially stabilize tau(297-391) conformations in which amyloid-forming segments are more accessible or more favorably oriented for intermolecular association. Rather than directly templating a specific fibril structure, such interactions could bias the conformational landscape of tau(297-391) towards aggregation-competent states, thereby increasing the probability of productive amyloid assembly. This mechanism would be compatible with the observed kinetic modulation without requiring P12 to remain permanently associated with the

mature fibril. However, the present experiments do not directly resolve tau(297-391) conformational states or demonstrate APR–APR contacts, and this interpretation therefore remains a mechanistic hypothesis.

A second mechanism becomes particularly relevant when P12 itself assembles. Under NaCl conditions, high concentrations of P12 produced an early ThT-positive event before the major tau(297-391)-associated transition, and independently preformed P12 assemblies were capable of promoting the emergence of a tau(297-391)-associated ThT response. P12 assemblies may therefore provide interaction surfaces that influence tau(297-391) aggregation. Whether this represents true structural cross-seeding or a less specific surface-assisted process remains unresolved.

A third possibility is that P12 remains associated with the fibrillar products. The aggregation-associated loss of soluble P12 and direct visualization of P12-Biotin on fibrillar material are consistent with such an association. Importantly, stable association does not necessarily imply incorporation into the ordered core. Amyloid fibrils present structurally diverse interaction sites, including growing ends, external fibril surfaces and higher-order interfaces between associated filaments [57]. Any of these locations could retain P12 while allowing it to influence fibril growth or organization. Such surface association also provides an alternative interpretation of some of the differences observed in ThT fluorescence between tau(297-391)-only and tau(297-391)–P12 reactions, since P12 bound to fibril surfaces could modify the accessibility or local environment of ThT-binding sites without necessarily reflecting a proportional change in amyloid mass [56]. More generally, part of the kinetic effect observed upon addition of P12 could also arise from non-specific physicochemical effects associated with increasing peptide concentration. An increased number of molecular encounters, or changes in the effective local concentration and collision dynamics of tau(297-391) molecules, could favor productive tau(297-391) assembly without requiring sequence-specific recognition of P12. Such a mechanism would therefore need to be distinguished experimentally from a genuine heterotypic tau(297-391)–P12 interaction. These alternative explanations further illustrate why ThT kinetics alone cannot define the molecular origin of the observed effect.

The sequence architecture of P12 provides a plausible molecular basis for these interactions. P12 contains the two APRs of TRA2B which have sequence similarity to the amyloid-forming regions of Tau, and previous work from the SwitchLab showed that the dual-APR-containing peptide has a stronger effect on tau(297-391) aggregation than shorter single-APR constructs or variants in which β-sheet propensity was disrupted by proline substitutions [47; unpublished data, SwitchLab]. These observations are consistent with an APR-dependent heterotypic recognition mechanism. Nevertheless, the current study did not directly map a physical interface between the TRA2B APRs and PHF6, PAM4 or another Tau APR segment. Direct APR–APR recognition therefore remains a mechanistically attractive hypothesis rather than a demonstrated molecular interaction.

Taken together, the present data favor a context-dependent model of heterotypic modulation rather than a single defined mechanism. The contribution of P12 appears to depend on its concentration, physical state and reaction environment, with different interaction modes potentially becoming relevant at different stages of tau(297–391) assembly. However, the current experiments do not establish which mechanism predominates, nor whether the observed effects are driven by specific APR–APR recognition. The central unresolved question is therefore how these heterotypic interactions are

organized at the molecular level and how they translate into the modulation of tau(297–391) assembly observed experimentally.

5.6. Biological relevance and limitations of the reductionist tau(297-391)/P12 system

The reductionist character of the tau(297-391)/P12 system is both its principal strength and its principal limitation. By isolating a restricted amyloid-forming region of Tau together with the dual-APR-containing region of TRA2B, the system removes many molecular variables and demonstrates that relatively small sequence elements are sufficient to reproduce measurable modulation of amyloid assembly. In this sense, the present results provide a molecular bridge between previous cellular observations of TRA2B-dependent enhancement of Tau seeding and a potential direct interaction encoded within the two protein sequences.

However, tau(297-391) cannot fully reproduce the behavior of full-length Tau (Tau-FL). The fragment retains important amyloid-forming regions and can generate PHF-like fibrils, but it lacks large N- and C-terminal regions, much of the physiological fuzzy coat, and many sites of post-translational modification. These regions influence Tau-FL conformational dynamics, interactions and accessibility of amyloid-forming sequences in the full-length protein [33; 36; 61]. An interaction readily accessible in tau(297-391) may therefore be weakened, enhanced or regulated differently in Tau-FL.

The same limitation applies on the TRA2B side. P12 isolates the dual-APR region but does not reproduce the complete structural and regulatory context of TRA2B. In the full protein, these regions form part of an RNA-recognition motif and their accessibility may be influenced by folding, RNA binding, neighboring domains, post-translational modifications or interaction partners [48]. Demonstrating that P12 influences tau(297-391) therefore supports the sufficiency of the isolated region under the tested conditions but does not establish that full-length TRA2B interacts with Tau-FL through an identical mechanism.

The peptide concentrations used in some experiments also require consideration. High P12 concentrations were intentionally explored to reveal concentration-dependent effects and to investigate the emergence of P12 self-assembly. These experiments are mechanistically informative but should not be interpreted as reproducing physiological intracellular concentrations of TRA2B-derived sequences.

Several methodological limitations also constrain mechanistic interpretation. ThT provides an indirect readout of amyloid formation and cannot identify the microscopic kinetic step modified by P12 [56]. Similarly, the fibril-derived seeds used in the study were heterogeneous and their concentrations were expressed as monomer equivalents rather than as particle or fibril-end concentrations. Because equal tau(297-391) monomer-equivalent concentrations do not correspond to equal numbers of seed particles or accessible fibril ends, this approximation limits quantitative comparisons between different seed preparations and, consequently, between experiments performed under otherwise identical conditions [63].

Negative-stain TEM provides valuable morphological information but samples only a fraction of a heterogeneous preparation and is sensitive to grid adsorption, orientation and staining. Consequently, crossover measurements distinguish recurring morphological classes but cannot establish molecular fold [53]. The approximately 62 nm population observed in tau(297-391)–P12 reactions should therefore be considered an interesting morphological signature rather than evidence for a novel heterotypic structure.

Cryo-EM screening addressed this limitation only partially. The optimization identified Quantifoil conditions that provided a useful balance between fibril density, separation and ice thickness, and a tau(297-391)–P12 sample suitable for future data acquisition was obtained. Consequently, cryo-EM presently demonstrates structural feasibility rather than a P12-dependent change in tau(297-391) architecture.

Taken together, these limitations define the scope within which the present findings should be interpreted. The tau(297–391)/P12 system demonstrates that the isolated amyloid-forming region of Tau and the dual-APR region of TRA2B are sufficient to generate measurable changes in assembly behavior and fibrillar association under controlled *in vitro* conditions. However, the biological relevance of this mechanism will ultimately depend on whether comparable interactions can be reproduced in the context of full-length Tau and TRA2B, where additional sequence regions, post-translational modifications and cellular partners may substantially reshape the interaction landscape. The value of the present reductionist system therefore lies primarily in identifying a tractable molecular interaction framework that can now be tested in progressively more complete biological contexts.

5.7. Future directions: discriminating between the remaining mechanistic models

The most informative next experiments should be those capable of distinguishing between the remaining molecular models rather than simply reproducing the kinetic phenotype observed in this study.

A first priority is to determine whether P12 and tau(297–391) are present on the same individual fibrils. The dual-size nanogold strategy developed here provides a direct route to address this question, but the current level of background must first be reduced through optimization of blocking conditions, reagent concentrations, incubation times and washing steps. Tau(297–391)-only, P12-Biotin-only, omission-of-primary-antibody and streptavidin controls should be processed under identical conditions to establish the specificity of each labeling arm. In future experiments, P12-Biotin should also be used as a minor tracer population mixed with an excess of unmodified P12, rather than as a complete replacement for native P12. This tracer-like strategy would reduce the influence of the biotin modification on the overall aggregation behavior while still allowing P12-derived material to be localized by nanogold labeling. Reliable detection of both distinguishable particle sizes along the same continuous fibrils would substantially strengthen the evidence for stable tau(297–391)–P12 association.

A second priority is the high-resolution comparison of tau(297–391) and tau(297–391)–P12 fibrils generated under otherwise identical optimized $MgCl_2$ conditions. The cryo-EM grid-screening performed in this study provides a starting point for full data collection. Initial two-dimensional classification could determine whether reproducible fibrillar

populations can be identified and compared between the two conditions. If sufficiently homogeneous populations are obtained, helical reconstruction could potentially establish whether the presence of P12 is associated with changes in tau(297–391) protofilament fold or packing. The identification of additional ordered density in tau(297–391)–P12 fibrils would provide particularly informative evidence for a structural contribution of P12. Conversely, the absence of a clearly defined additional density could not exclude an interaction, since P12 could remain flexible, heterogeneous, substoichiometric or predominantly associated with fibril surfaces, or manifest only as locally less well-resolved or more structurally heterogeneous regions within the reconstruction.

Finally, the reductionist mechanism identified in the tau(297-391)/P12 system should progressively be tested in more complete biological contexts. Full-length TRA2B represents the most direct next step, followed by systems containing longer Tau constructs or full-length Tau. Determining whether the molecular behaviors observed with P12 are retained in the context of the complete proteins would be essential for connecting the present structural and biophysical observations with the cellular and *in vivo* effects previously established for TRA2B.

Together, these experiments would provide a logical progression from functional modulation to spatial localization, high-resolution structural characterization and, ultimately, biological validation. This progression would help determine whether the effects observed in the reductionist tau(297-391)–P12 system reflect stable molecular association, a direct influence on fibril architecture or a more transient mechanism of heterotypic modulation.

5.8. General conclusion

Taken together, the present study supports the view that a molecular interaction partner can reshape the assembly behavior of an amyloid-forming protein without requiring demonstrated incorporation into its ordered fibril core. The TRA2B-derived peptide P12 modified tau(297-391) aggregation in a concentration, assembly-state, and environment dependent manner. Preformed P12 assemblies were able to promote a tau(297-391)-associated aggregation response, while biochemical and imaging observations further indicated that P12-derived material partitions with and can associate with fibrillar structures.

At the structural level, tau(297-391)–P12 co-incubation was associated with a possible modulation of polymorph selection, including a recurring periodic population distinct from the principal morphologies observed in either control. However, neither negative-stain TEM nor the current nanogold and cryo-EM data establish whether P12 enters the ordered tau(297-391) amyloid core or changes the underlying tau(297-391) fold. The available evidence is therefore most consistent with a set of non-mutually exclusive mechanisms involving transient interactions, assembly-mediated promotion, peripheral fibril association and possible modulation of polymorph selection. Resolving these alternatives will require direct tau(297-391)–P12 colocalization and high-resolution structural characterization.

In this sense, the answer to the question posed in the title of this thesis "**Can molecular partners reshape amyloid assembly?"** is already supported at the level of assembly behavior: the presence and physical state of P12 alter the way the tau(297-391) system evolves. Whether this reshaping extends to the precise molecular architecture of the tau(297-391) fibril itself remains the central structural question opened by this work.

6. Artificial intelligence tools utilization declaration

During the preparation of this Master's thesis, generative artificial intelligence tools, primarily ChatGPT (OpenAI), were used as supporting tools in several aspects of the work.

Language refinement and writing assistance: AI tools were used to improve English phrasing, correct grammar and spelling, refine scientific terminology, reduce repetition, and enhance the overall clarity and readability of the manuscript.

Literature exploration and experimental support: ChatGPT was used to assist in identifying potentially relevant scientific literature, exploring established laboratory protocols, troubleshooting experimental procedures, and considering possible optimization strategies for specific assays.

Schematic figure development: AI tools were used only to assist in the creation of schematic illustrations needed for the figure. These illustrations were reviewed, selected, and adapted by the author before inclusion in the thesis.

7. Bibliography

[1] GBD 2021 Nervous System Disorders Collaborators. Global, regional, and national burden of disorders affecting the nervous system, 1990–2021: a systematic analysis for the Global Burden of Disease Study 2021. The Lancet Neurology. 2024;23(4):344–381. doi: 10.1016/S1474-4422(24)00038-3.

[2] Toader C, Tataru CP, Munteanu O, Serban M, Covache-Busuioc RA, Ciurea AV, et al. Decoding neurodegeneration: a review of molecular mechanisms and therapeutic advances in Alzheimer's, Parkinson's, and ALS. International Journal of Molecular Sciences. 2024;25(23):12613. doi: 10.3390/ijms252312613.

[3] Otzen D, Riek R. Functional amyloids. Cold Spring Harbor Perspectives in Biology. 2019;11(12):a033860. doi: 10.1101/cshperspect.a033860.

[4] Maji SK, Perrin MH, Sawaya MR, Jessberger S, Vadodaria K, Rissman RA, et al. Functional amyloids as natural storage of peptide hormones in pituitary secretory granules. Science. 2009;325(5938):328–332. doi: 10.1126/science.1173155.

[5] Louros N, Schymkowitz J, Rousseau F. Mechanisms and pathology of protein misfolding and aggregation. Nature Reviews Molecular Cell Biology. 2023;24(12):912–933. doi: 10.1038/s41580-023-00647-2.

[6] Dill KA, MacCallum JL. The protein-folding problem, 50 years on. Science. 2012;338(6110):1042–1046. doi: 10.1126/science.1219021.

[7] Uversky VN. A decade and a half of protein intrinsic disorder: biology still waits for physics. Protein Science. 2013;22(6):693–724. doi: 10.1002/pro.2261.

[8] Henzler-Wildman K, Kern D. Dynamic personalities of proteins. Nature. 2007;450(7172):964–972. doi: 10.1038/nature06522.

[9] Jahn TR, Radford SE. Folding versus aggregation: polypeptide conformations on competing pathways. Archives of Biochemistry and Biophysics. 2008;469(1):100–117. doi: 10.1016/j.abb.2007.05.015.

[10] Fink AL. Protein aggregation: folding aggregates, inclusion bodies and amyloid. Folding & Design. 1998;3(1):R9–R23. doi: 10.1016/S1359-0278(98)00002-9.

[11] Housmans JAJ, Wu G, Schymkowitz J, Rousseau F. A guide to studying protein aggregation. The FEBS Journal. 2023;290(3):554–583. doi: 10.1111/febs.16312.

[12] Chiti F, Dobson CM. Protein misfolding, functional amyloid, and human disease. Annual Review of Biochemistry. 2006;75:333–366. doi: 10.1146/annurev.biochem.75.101304.123901.

[13] Knowles TPJ, Vendruscolo M, Dobson CM. The amyloid state and its association with protein misfolding diseases. Nature Reviews Molecular Cell Biology. 2014;15(6):384–396. doi: 10.1038/nrm3810.

[14] Taylor AIP, Staniforth RA. General principles underpinning amyloid structure. Frontiers in Neuroscience. 2022;16:878869. doi: 10.3389/fnins.2022.878869.

[15] Beerten J, Schymkowitz J, Rousseau F. Aggregation prone regions and gatekeeping residues in protein sequences. Current Topics in Medicinal Chemistry. 2012;12(22):2470–2478. doi: 10.2174/1568026611212220003.

[16] Fernandez-Escamilla AM, Rousseau F, Schymkowitz J, Serrano L. Prediction of sequence-dependent and mutational effects on the aggregation of peptides and proteins. Nature Biotechnology. 2004;22(10):1302–1306. doi: 10.1038/nbt1012.

[17] Buck PM, Kumar S, Singh SK. On the role of aggregation prone regions in protein evolution, stability, and enzymatic catalysis: insights from diverse analyses. PLOS Computational Biology. 2013;9(10):e1003291. doi: 10.1371/journal.pcbi.1003291.

[18] Goldschmidt L, Teng PK, Riek R, Eisenberg D. Identifying the amylome, proteins capable of forming amyloid-like fibrils. Proceedings of the National Academy of Sciences of the United States of America. 2010;107(8):3487–3492. doi: 10.1073/pnas.0915166107.

[19] Michaels TCT, Šarić A, Habchi J, Chia S, Meisl G, Vendruscolo M, et al. Chemical kinetics for bridging molecular mechanisms and macroscopic measurements of amyloid fibril formation. Annual Review of Physical Chemistry. 2018;69:273–298. doi: 10.1146/annurev-physchem-050317-021322.

[20] Grigolato F, Arosio P. The role of surfaces on amyloid formation. Biophysical Chemistry. 2021;270:106533. doi: 10.1016/j.bpc.2020.106533.

[21] Visser BS, Lipiński WP, Spruijt E. The role of biomolecular condensates in protein aggregation. Nature Reviews Chemistry. 2024;8(9):686–700. doi: 10.1038/s41570-024-00635-w.

[22] Labbadia J, Morimoto RI. The biology of proteostasis in aging and disease. Annual Review of Biochemistry. 2015;84:435–464. doi: 10.1146/annurev-biochem-060614-033955.

[23] Eisenberg D, Jucker M. The amyloid state of proteins in human diseases. Cell. 2012;148(6):1188–1203. doi: 10.1016/j.cell.2012.02.022.

[24] Jahn TR, Makin OS, Morris KL, Marshall KE, Tian P, Sikorski P, et al. The common architecture of cross-β amyloid. Journal of Molecular Biology. 2010;395(4):717–727. doi: 10.1016/j.jmb.2009.09.039.

[25] Fitzpatrick AWP, Debelouchina GT, Bayro MJ, Clare DK, Caporini MA, Bajaj VS, et al. Atomic structure and hierarchical assembly of a cross-β amyloid fibril. Proceedings of the National Academy of Sciences of the United States of America. 2013;110(14):5468–5473. doi: 10.1073/pnas.1219476110.

[26] Nelson R, Sawaya MR, Balbirnie M, Madsen AØ, Riekel C, Grothe R, et al. Structure of the cross-β spine of amyloid-like fibrils. Nature. 2005;435(7043):773–778. doi: 10.1038/nature03680.

[27] Sawaya MR, Sambashivan S, Nelson R, Ivanova MI, Sievers SA, Apostol MI, et al. Atomic structures of amyloid cross-β spines reveal varied steric zippers. Nature. 2007;447(7143):453–457. doi: 10.1038/nature05695.

[28] Tycko R. Amyloid polymorphism: structural basis and neurobiological relevance. Neuron. 2015;86(3):632–645. doi: 10.1016/j.neuron.2015.03.017.

[29] Shi Y, Zhang W, Yang Y, Murzin AG, Falcon B, Kotecha A, et al. Structure-based classification of tauopathies. Nature. 2021;598(7880):359–363. doi: 10.1038/s41586-021-03911-7.

[30] Petkova AT, Leapman RD, Guo Z, Yau WM, Mattson MP, Tycko R. Self-propagating, molecular-level polymorphism in Alzheimer's β-amyloid fibrils. Science. 2005;307(5707):262–265. doi: 10.1126/science.1105850.

[31] Gallardo R, Ranson NA, Radford SE. Amyloid structures: much more than just a cross-β fold. Current Opinion in Structural Biology. 2020;60:7–16. doi: 10.1016/j.sbi.2019.09.001.

[32] Ulamec SM, Brockwell DJ, Radford SE. Looking beyond the core: the role of flanking regions in the aggregation of amyloidogenic peptides and proteins. Frontiers in Neuroscience. 2020;14:611285. doi: 10.3389/fnins.2020.611285.

[33] Wegmann S, Medalsy ID, Mandelkow E, Müller DJ. The fuzzy coat of pathological human Tau fibrils is a two-layered polyelectrolyte brush. Proceedings of the National Academy of Sciences of the United States of America. 2013;110(4):E313–E321. doi: 10.1073/pnas.1212100110.

[34] Bejanin A, Schonhaut DR, La Joie R, Kramer JH, Baker SL, Sosa N, et al. Tau pathology and neurodegeneration contribute to cognitive impairment in Alzheimer's disease. Brain. 2017;140(12):3286–3300. doi: 10.1093/brain/awx243.

[35] Goedert M, Spillantini MG, Jakes R, Rutherford D, Crowther RA. Multiple isoforms of human microtubule-associated protein tau: sequences and localization in neurofibrillary tangles of Alzheimer's disease. Neuron. 1989;3(4):519–526. doi: 10.1016/0896-6273(89)90210-9.

[36] Jeganathan S, von Bergen M, Brutlach H, Steinhoff H-J, Mandelkow E. Global hairpin folding of tau in solution. Biochemistry. 2006;45(7):2283–2293. doi: 10.1021/bi0521543.

[37] Despres C, Byrne C, Qi H, Cantrelle F-X, Huvent I, Chambraud B, et al. Identification of the Tau phosphorylation pattern that drives its aggregation. Proceedings of the National Academy of Sciences of the United States of America. 2017;114(34):9080–9085. doi: 10.1073/pnas.1708448114.

[38] Seidler PM, Boyer DR, Rodriguez JA, Sawaya MR, Cascio D, Murray K, et al. Structure-based inhibitors of tau aggregation. Nature Chemistry. 2018;10(2):170–176. doi: 10.1038/nchem.2889.

[39] Louros N, Wilkinson M, Tsaka G, Ramakers M, Morelli C, Garcia T, et al. Local structural preferences in shaping tau amyloid polymorphism. Nature Communications. 2024;15(1):1028. doi: 10.1038/s41467-024-45429-2.

[40] Fitzpatrick AWP, Falcon B, He S, Murzin AG, Murshudov G, Garringer HJ, et al. Cryo-EM structures of tau filaments from Alzheimer's disease. Nature. 2017;547(7662):185–190. doi: 10.1038/nature23002.

[41] Zhang W, Falcon B, Murzin AG, Fan J, Crowther RA, Goedert M, et al. Heparin-induced tau filaments are polymorphic and differ from those in Alzheimer's and Pick's diseases. eLife. 2019;8:e43584. doi: 10.7554/eLife.43584.

[42] Kosik KS, Joachim CL, Selkoe DJ. Microtubule-associated protein tau (tau) is a major antigenic component of paired helical filaments in Alzheimer disease. Proceedings of the National Academy of Sciences of the United States of America. 1986;83(11):4044–4048. doi: 10.1073/pnas.83.11.4044.

[43] Drummond E, Pires G, MacMurray C, Askenazi M, Nayak S, Bourdon M, et al. Phosphorylated tau interactome in the human Alzheimer's disease brain. Brain. 2020;143(9):2803–2817. doi: 10.1093/brain/awaa223.

[44] Kavanagh T, Halder A, Drummond E. Tau interactome and RNA binding proteins in neurodegenerative diseases. Molecular Neurodegeneration. 2022;17(1):66. doi: 10.1186/s13024-022-00572-6.

[45] Molliex A, Temirov J, Lee J, Coughlin M, Kanagaraj AP, Kim HJ, et al. Phase separation by low complexity domains promotes stress granule assembly and drives pathological fibrillization. Cell. 2015;163(1):123–133. doi: 10.1016/j.cell.2015.09.015.

[46] Banani SF, Lee HO, Hyman AA, Rosen MK. Biomolecular condensates: organizers of cellular biochemistry. Nature Reviews Molecular Cell Biology. 2017;18(5):285–298. doi: 10.1038/nrm.2017.7.

[47] Louros N, Ramakers M, Michiels E, Konstantoulea K, Morelli C, Garcia T, et al. Mapping the sequence specificity of heterotypic amyloid interactions enables the identification of aggregation modifiers. Nature Communications. 2022;13(1):1351. doi: 10.1038/s41467-022-28955-9.

[48] Tsuda K, Someya T, Kuwasako K, Takahashi M, He F, Unzai S, et al. Structural basis for the dual RNA-recognition modes of human Tra2-β RRM. Nucleic Acids Research. 2011;39(4):1538–1553. doi: 10.1093/nar/gkq854.

[49] Jiang Z, Tang H, Havlioglu N, Zhang X, Stamm S, Yan R, et al. Mutations in Tau gene exon 10 associated with FTDP-17 alter the activity of an exonic splicing enhancer to interact with Tra2β. Journal of Biological Chemistry. 2003;278(21):18997–19007. doi: 10.1074/jbc.M301800200.

[50] Lövestam S, Koh FA, van Knippenberg B, Kotecha A, Murzin AG, Goedert M, et al. Assembly of recombinant tau into filaments identical to those of Alzheimer's disease and chronic traumatic encephalopathy. eLife. 2022;11:e76494. doi: 10.7554/eLife.76494.

[51] Li X, Zhang S, Liu Z, Tao Y, Xia W, Sun Y, et al. Subtle change of fibrillation condition leads to substantial alteration of recombinant Tau fibril structure. iScience. 2022;25(12):105645. doi: 10.1016/j.isci.2022.105645.

[52] Sanchez JC, Pierson JA, Borcik CG, Rienstra CM, Wright ER. High-resolution Cryo-EM structure determination of α-synuclein—a prototypical amyloid fibril. Bio-protocol. 2025;15(3):e5171. doi: 10.21769/BioProtoc.5171.

[53] Glynn C, Chun JE, Donahue CC, Nadler MJS, Fan Z, Hyman BT. Reconstitution of the Alzheimer's Disease Tau Core Structure from Recombinant Tau297–391 Yields Variable Quaternary Structures as Seen by Negative Stain and Cryo-EM. Biochemistry. 2024;63(2):194–201. doi: 10.1021/acs.biochem.3c00425.

[54] Al-Hilaly YK, Pollack SJ, Vadukul DM, Citossi F, Rickard JE, Simpson M, et al. Alzheimer's Disease-like Paired Helical Filament Assembly from Truncated Tau Protein Is Independent of Disulfide Crosslinking. Journal of Molecular Biology. 2017;429(23):3650–3665. doi: 10.1016/j.jmb.2017.09.007.

[55] Warmadewanthi, Liu JC. Selective precipitation of phosphate from semiconductor wastewater. Journal of Environmental Engineering. 2009;135(10):1063–1070. doi: 10.1061/(ASCE)EE.1943-7870.0000054.

[56] Biancalana M, Koide S. Molecular mechanism of Thioflavin-T binding to amyloid fibrils. Biochimica et Biophysica Acta - Proteins and Proteomics. 2010;1804(7):1405–1412. doi: 10.1016/j.bbapap.2010.04.001.

[57] Törnquist M, Michaels TCT, Sanagavarapu K, Yang X, Meisl G, Cohen SIA, et al. Secondary nucleation in amyloid formation. Chemical Communications. 2018;54(63):8667–8684. doi: 10.1039/C8CC02204F.

[58] Ren B, Zhang Y, Zhang M, Liu Y, Zhang D, Gong X, et al. Fundamentals of cross-seeding of amyloid proteins: an introduction. Journal of Materials Chemistry B. 2019;7(46):7267–7282. doi: 10.1039/C9TB01871A.

[59] Al-Hilaly YK, Foster BE, Biasetti L, Lutter L, Pollack SJ, Rickard JE, et al. Tau (297–391) forms filaments that structurally mimic the core of paired helical filaments in Alzheimer's disease brain. FEBS Letters. 2020;594(5):944–950. doi: 10.1002/1873-3468.13675.

[60] Zapadka KL, Becher FJ, Gomes dos Santos AL, Jackson SE. Factors affecting the physical stability (aggregation) of peptide therapeutics. Interface Focus. 2017;7(6):20170030. doi: 10.1098/rsfs.2017.0030.

[61] Ye H, Han Y, Li P, Su Z, Huang Y. The Role of Post-Translational Modifications on the Structure and Function of Tau Protein. Journal of Molecular Neuroscience. 2022;72(8):1557–1571. doi: 10.1007/s12031-022-02002-0.

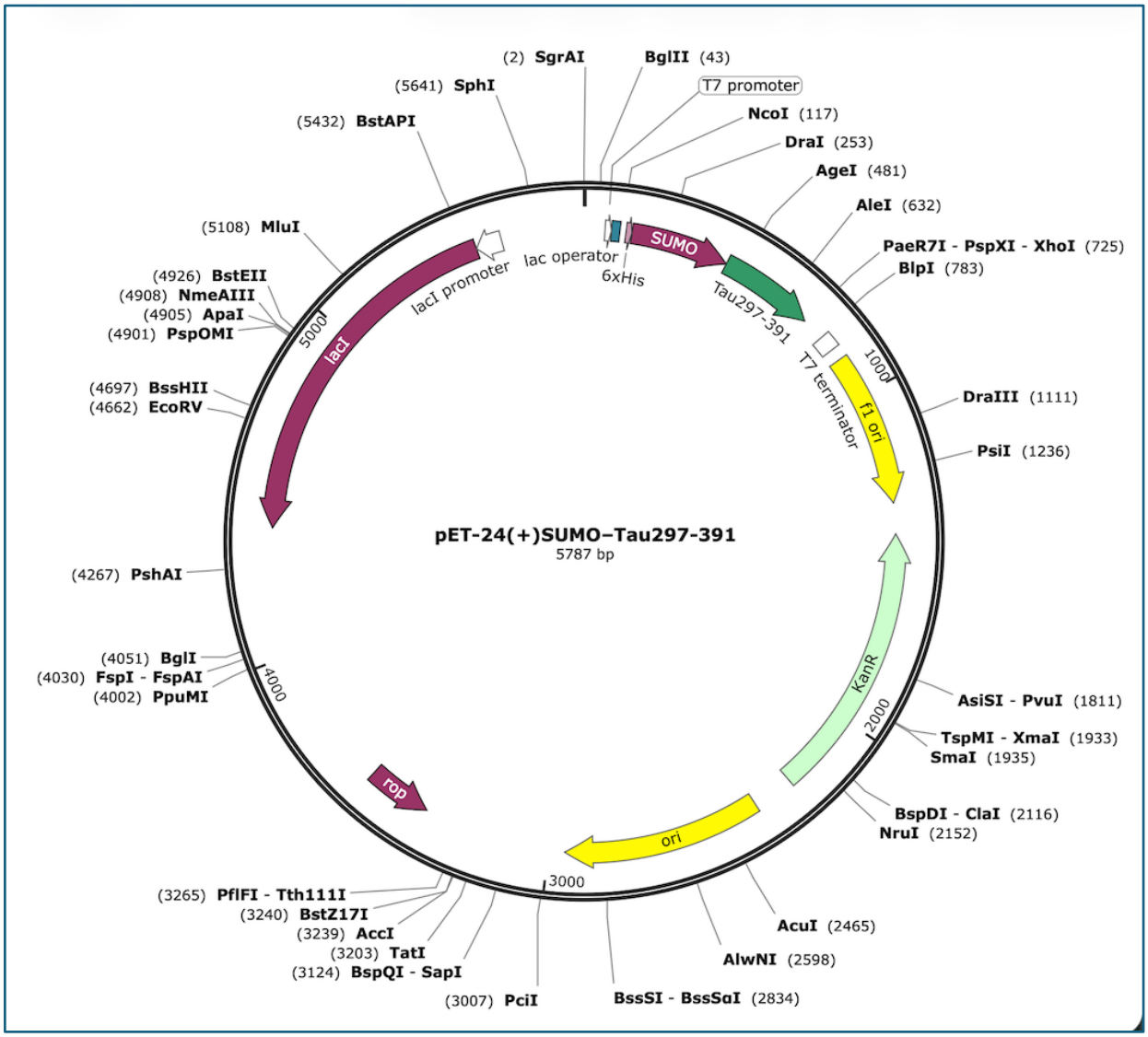
[62] Duan P, Dregni AJ, El Mammeri N, Hong M. Structure of the nonhelical filament of the Alzheimer's disease tau core. 2023;120(44):e2310067120. Proceedings of the National Academy of Sciences of the United States of America. doi: 10.1073/pnas.2310067120.

[63] Meyer V, Dinkel PD, Rickman Hager E, Margittai M. Amplification of Tau Fibrils from Minute Quantities of Seeds. *Biochemistry*. 2014;53(36):5804–5809. doi: 10.1021/bi501050g.

8. Supplementary Information

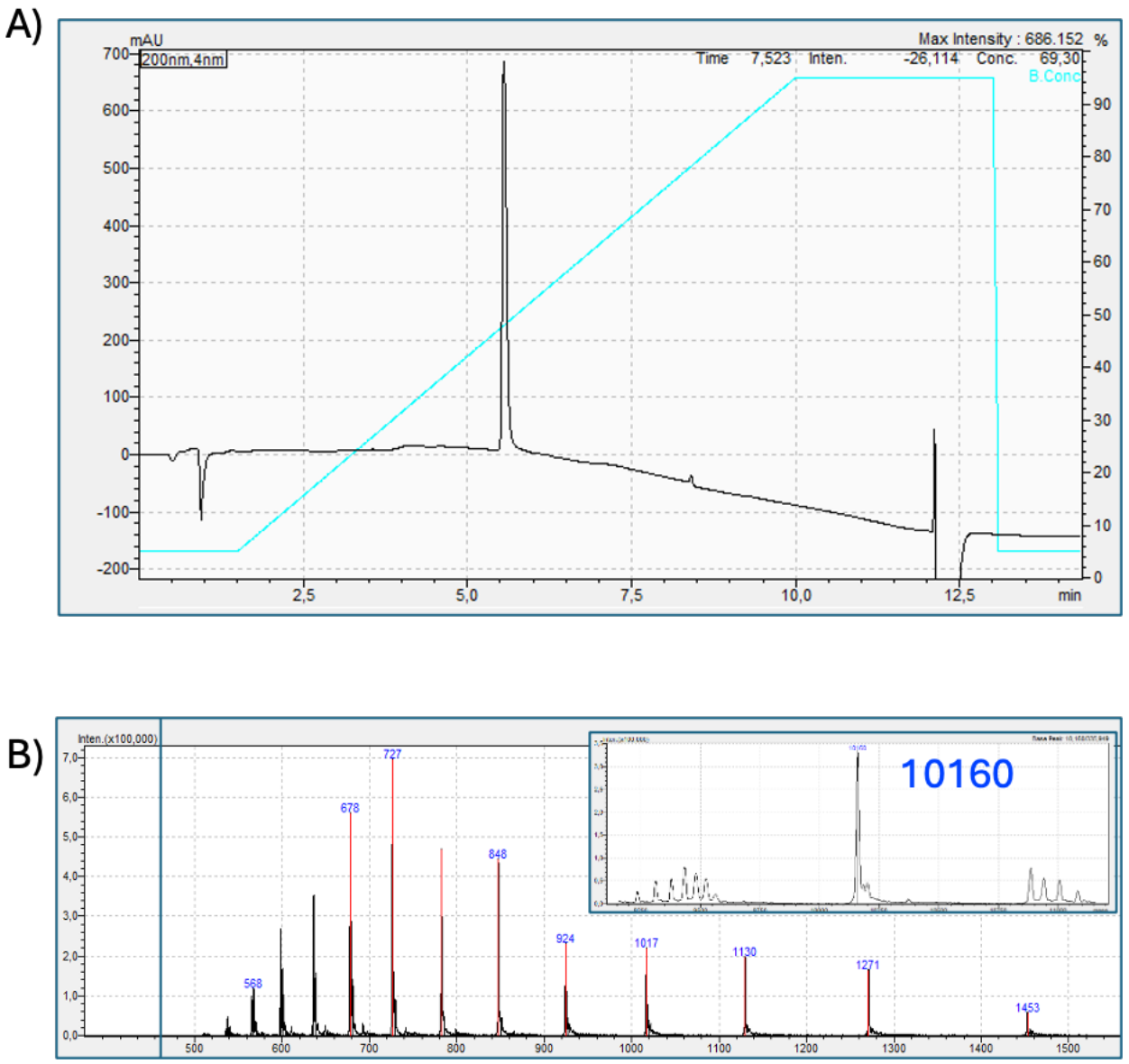
8.1. Supplementary Figures

Supplementary Figure S1



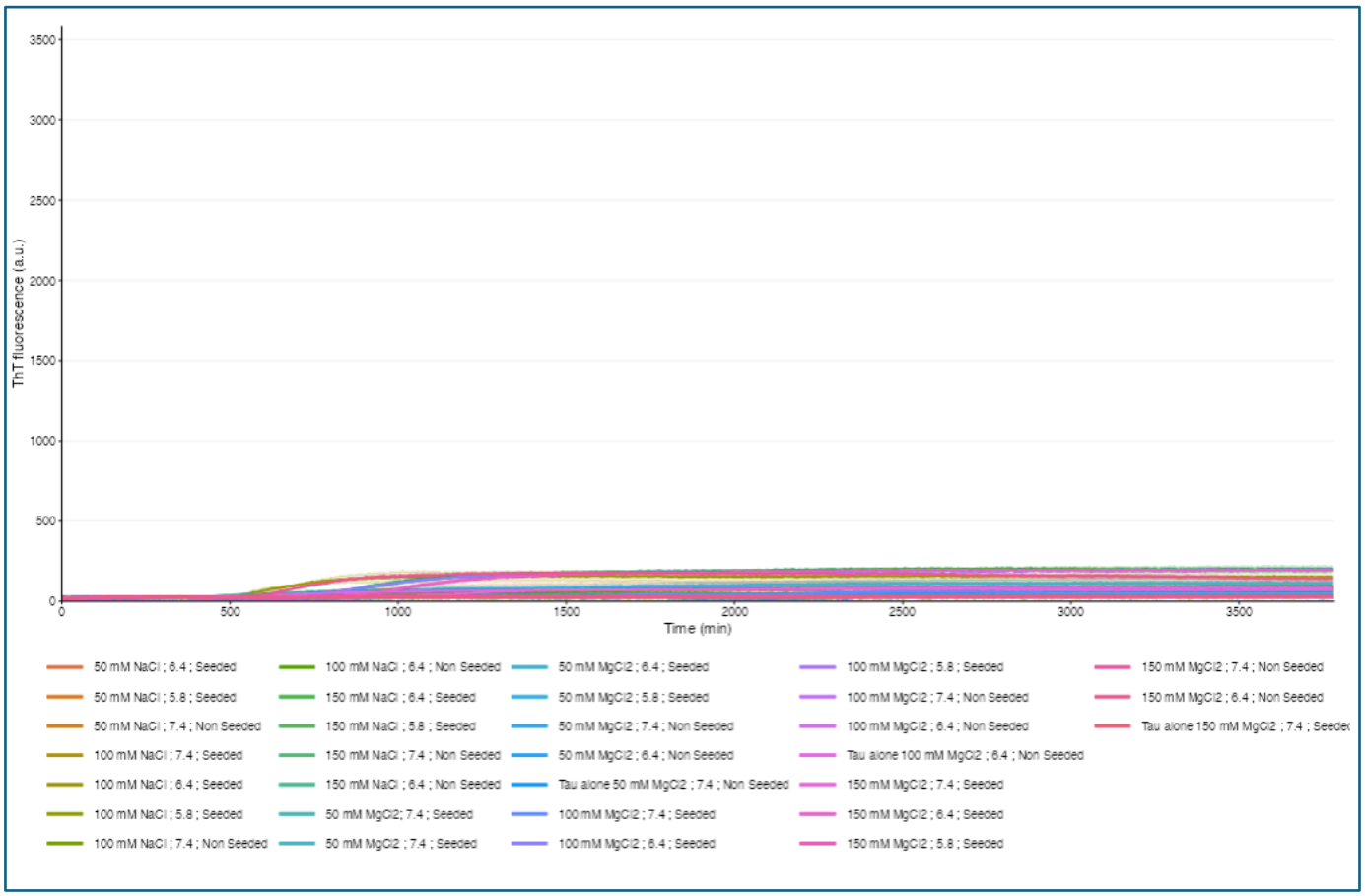
Supplementary Figure S1. Plasmid map of the pET-24(+)-SUMO-tau(297–391) expression construct. The 5,787-bp construct encodes Tau residues 297–391 fused N-terminally to a 6×His-tagged SUMO domain under the control of a T7 promoter and lac operator. The pET-24(+) backbone contains the *lacI* repressor gene, kanamycin-resistance marker (*KanR*), bacterial origin of replication (*ori*), f1 origin, and T7 transcription terminator. Relevant restriction sites are indicated around the plasmid map.

Supplementary Figure S2



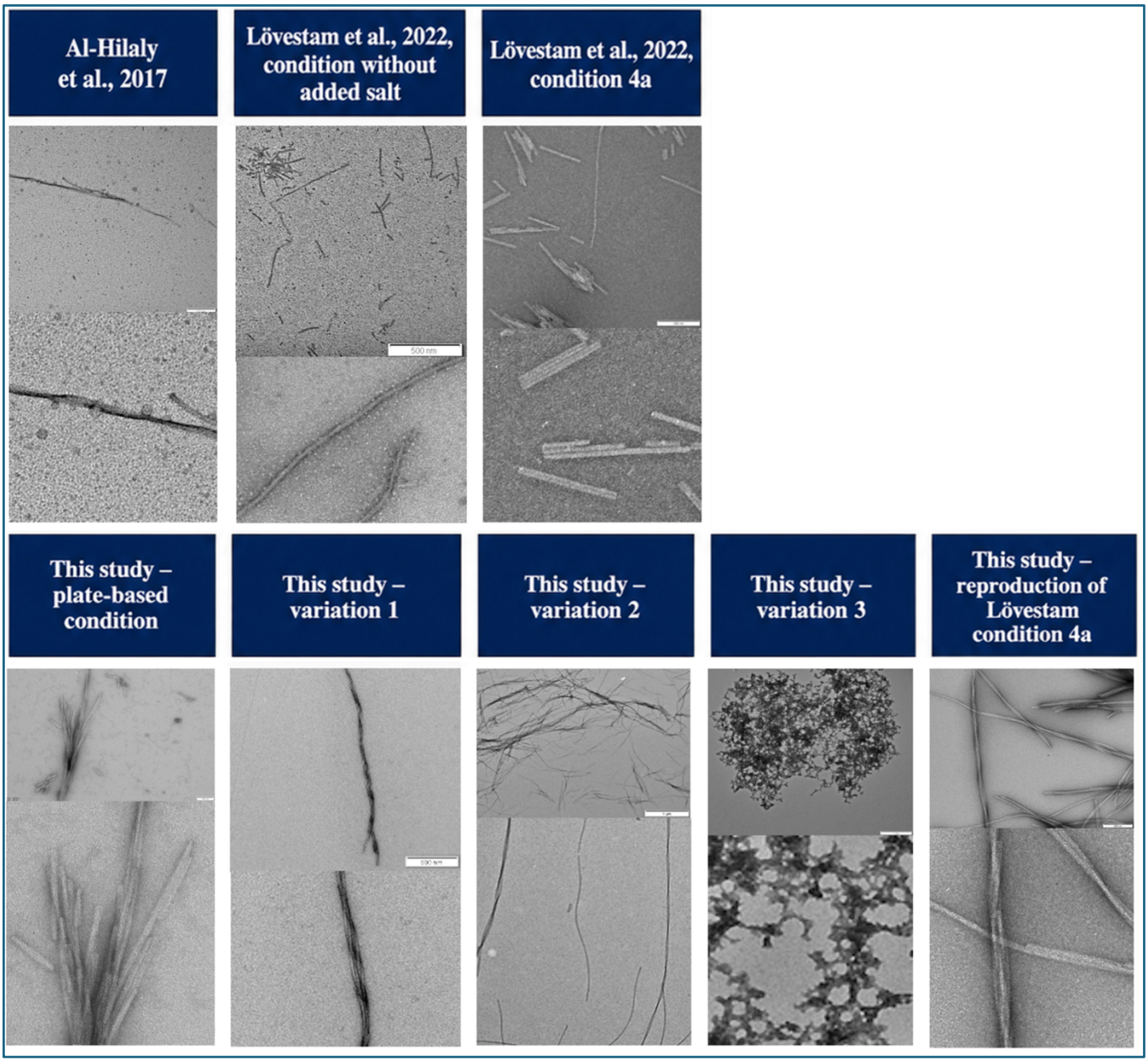
Supplementary Figure S2. LC–MS analysis of purified tau(297-391) fraction indicated by the green dashed boundaries in Figure 9. (A) Analytical LC chromatogram of the pooled tau(297–391) fraction. (B) Corresponding mass spectrum.

Supplementary Figure S3



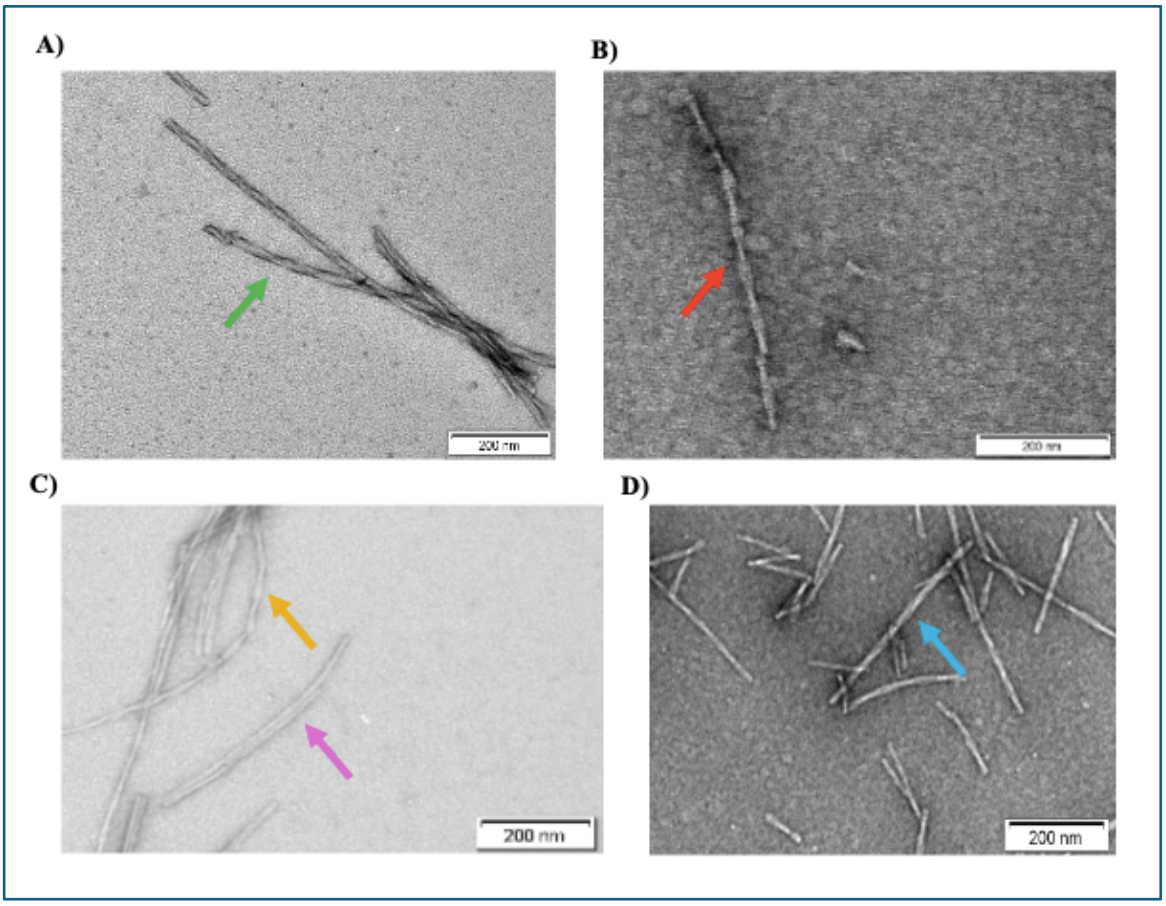
Supplementary Figure S3. ThT fluorescence profiles from the initial aggregation-condition screening of the tau(297–391)/P12 system. ThT kinetics are shown for all combinations of NaCl or $MgCl_2$ (50, 100, and 150 mM), pH 5.8, 6.4, or 7.4, and seeded or non-seeded conditions tested using 28 µM tau(297–391) and 7 µM P12 that did not produce a clearly defined aggregation transition. Seeded reactions contained 1 µM preformed tau(297-391) seeds.

Supplementary Figure S4.



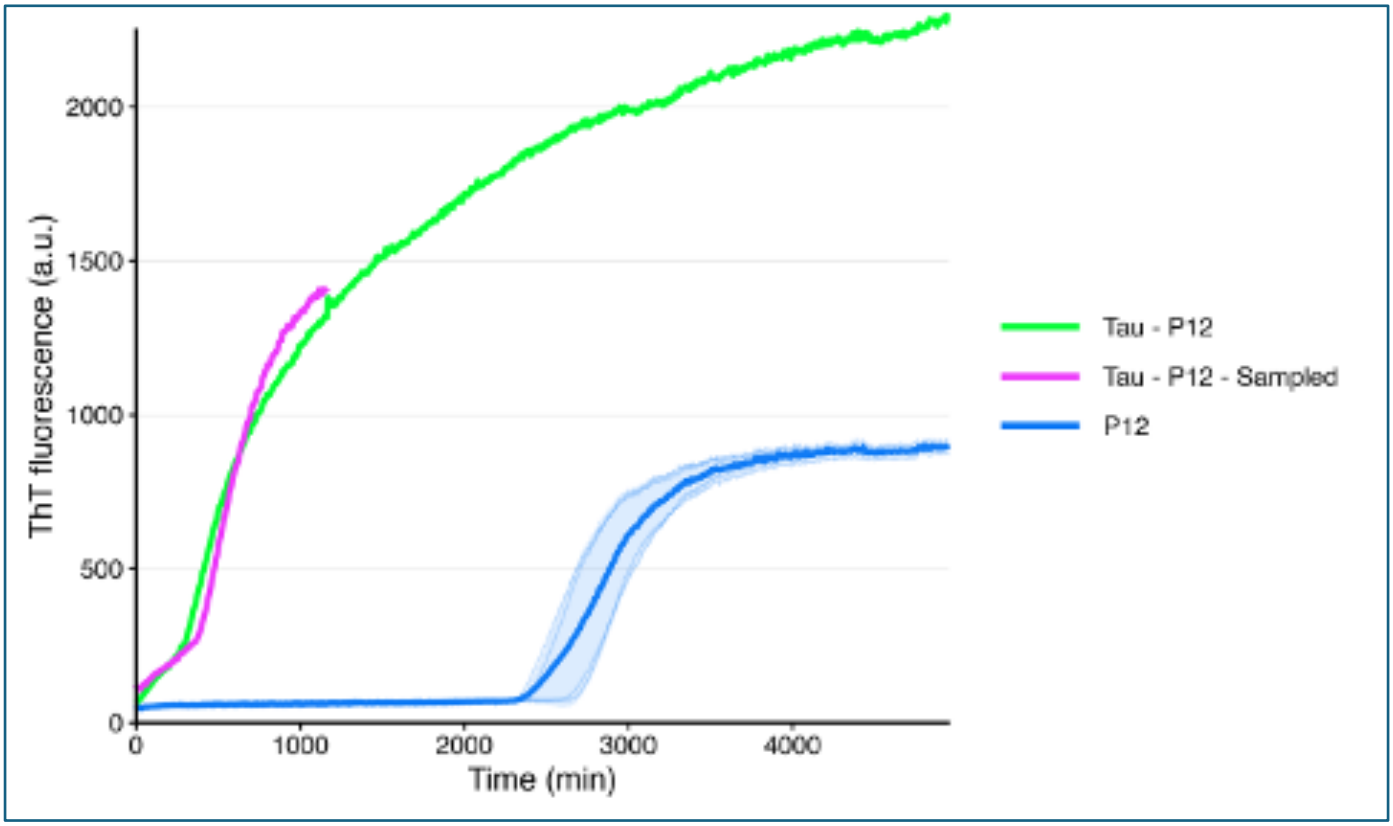
Supplementary Figure S4. Negative-stain TEM analysis of tau(297–391) fibrils generated under published and experimentally modified aggregation conditions. Representative micrographs are shown for conditions adapted from Al-Hilaly et al. (2017) and Lövestam et al. (2022), as well as for the plate-based condition and subsequent experimental variations tested in this study. The images illustrate the range of fibrillar morphologies obtained under the different conditions summarized in Figure 18.

Supplementary Figure S5



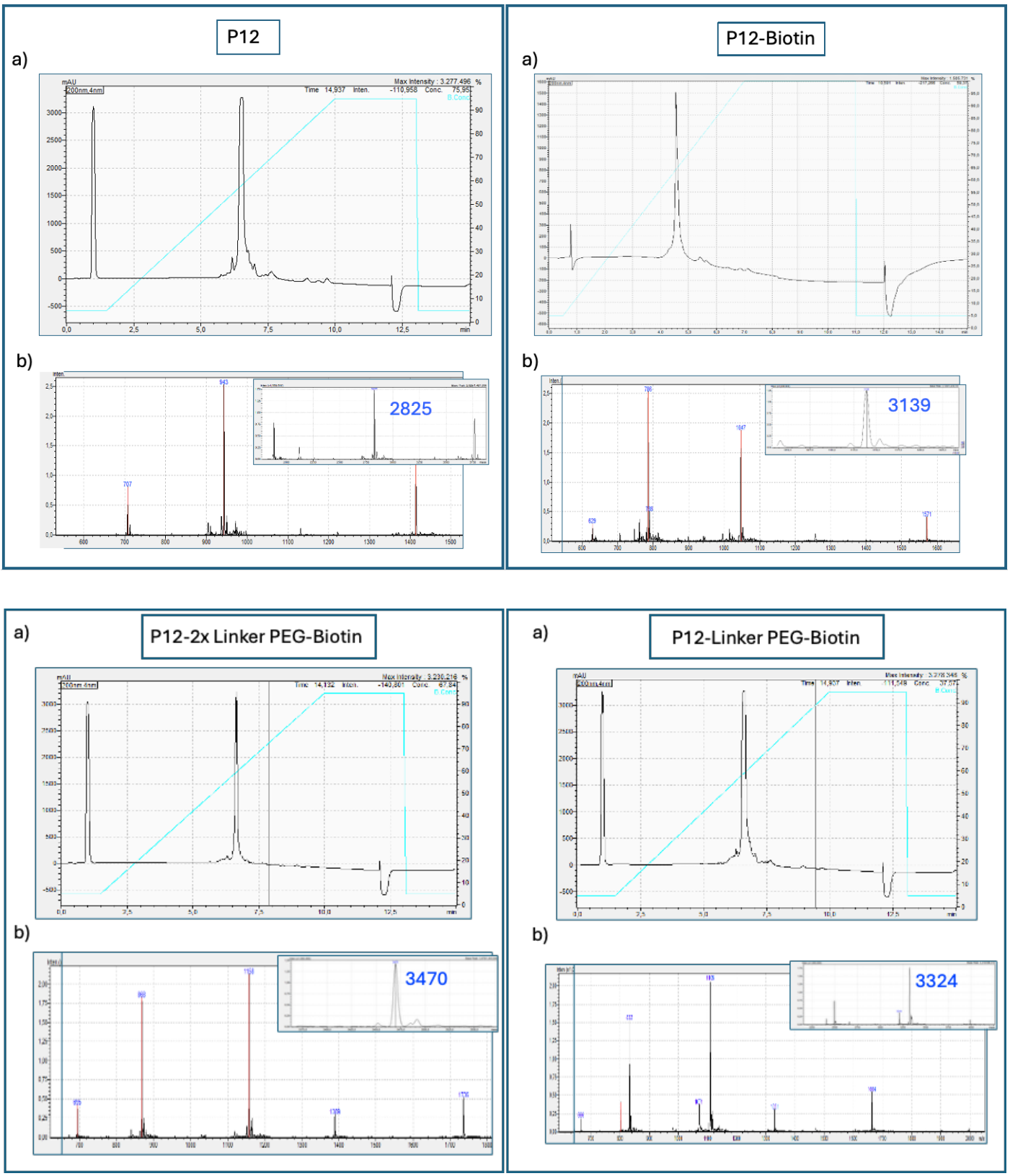
Supplementary Figure S5. Negative-stain TEM characterization of fibrillar morphologies observed in tau(297–391)–P12 co-incubation samples. (A) Periodically twisted fibrils with a crossover distance of approximately 100 nm (green arrow). **(B)** PHF-like fibril (red arrow). **(C)** Periodically twisted fibril with an intermediate crossover distance of approximately 62 nm (yellow arrow) and laterally associated fibrils (purple arrow). **(D)** Long, straight fibrils (blue arrow). Scale bars: 200 nm.

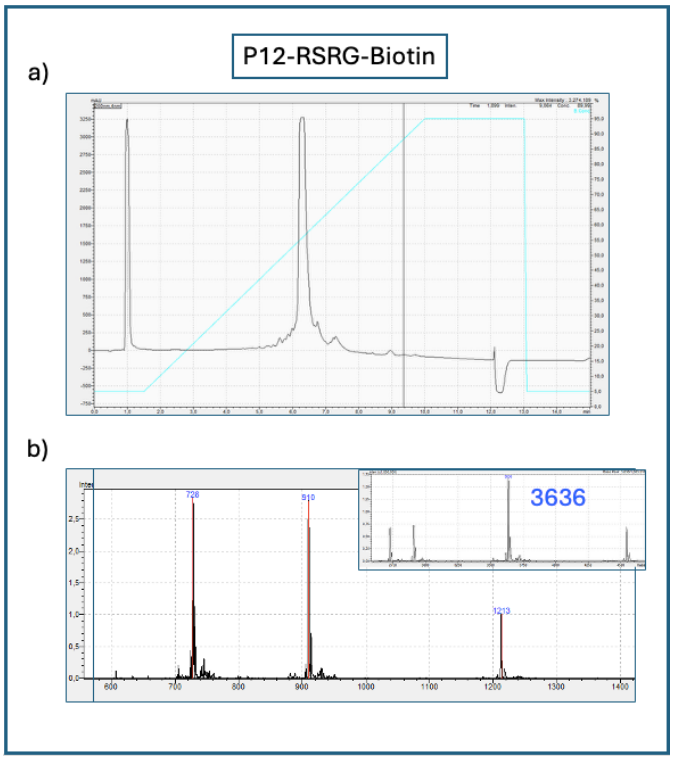
Supplementary Figure S6.



Supplementary Figure S6. ThT fluorescence monitoring of the tau(297–391)–P12 sample used for cryo-EM grid preparation. Aggregation kinetics of the tau(297–391)–P12 co-incubation (green) and the P12-only control (blue) were monitored by ThT fluorescence. The tau(297–391)–P12 reaction selected for cryo-EM sampling is shown in magenta and was removed from the assay during the rising phase of the ThT signal for grid preparation.

Supplementary Figure S7





Supplementary Figure S7. Analytical LC–MS characterization of P12-derived peptide constructs. Representative LC–MS analyses of P12 and the different modified P12 constructs. For each construct, **(a)** the analytical LC chromatogram and **(b)** the corresponding mass spectrum are shown. The inset displays the deconvoluted mass profile, with the molecular mass assigned to the major detected species indicated in blue. Calculated and experimentally determined molecular masses for all constructs are summarized in Supplementary Table S2.

8.2. Supplementary Tables

Supplementary Table S1.

Solution	Component	Final concentration / amount
Lysis buffer (supplemented Buffer A)	HEPES	50 mM
	NaCl	1 M
	Imidazole	25 mM
	TCEP	1 mM
	$MgCl_2$	0.5 mM
	Glycerol	10% (v/v)
	Triton X-100	0.1% (v/v)
	Benzamidine	1 mM
	Roche protease inhibitor cocktail	1 tablet per 50 mL
	RNase A	a pinch
	DNase	0.1%
Buffer A	HEPES	50 mM
	NaCl	1 M
	Imidazole	25 mM
	TCEP	1 mM
Buffer B	HEPES	50 mM
	NaCl	1 M
	Imidazole	500 mM
	TCEP	1 mM
Dialysis buffer	HEPES	50 mM
	NaCl	200 mM
	Imidazole	25 mM
	TCEP	1 mM

Supplementary Table S1. Composition of buffers used for cell lysis and purification of recombinant tau(297–391). Concentrations correspond to the final working concentrations of each component. IMAC buffers A and B were used for column equilibration, washing and gradient elution, whereas the dialysis buffer was used during ULP1-mediated removal of the 6×His–SUMO tag.

Supplementary Table S2.

Construct's label	Construct Sequence	Construct Final Expectation	Expected Final mass (Da)	Mass Check on LC-MS (Da)	LC-MS outcome
P12-Biotin	DLREVFSKYGPIADYSIVYDQQSR	DLREVFSKYGPIADYSIVYDQQSR-Biotin	3140	3139	Confirmed (valid)
P12-RSRG-Biotin	DLREVFSKYGPIADYSIVYDQQSRRSRG	DLREVFSKYGPIADYSIVYDQQSRRSRG-Biotin	3637,59	3636	Confirmed (valid)
P12-Linker PEG-Biotin	DLREVFSKYGPIADYSIVYDQQSR-PEG2	DLREVFSKYGPIADYSIVYDQQSR-PEG2-Biotin	3383,49	3328	Not confirmed (discarded)
P12-2x Linker PEG_Biotin	DLREVFSKYGPIADYSIVYDQQSR-PEG2-PEG2	DLREVFSKYGPIADYSIVYDQQSR-PEG2-PEG2-Biotin	3543,98	3474	Not confirmed (discarded)
P12	DLREVFSKYGPIADYSIVYDQQSR	DLREVFSKYGPIADYSIVYDQQSR	2828	2825.5	Confirmed (valid)

Supplementary Table S2. Design and LC–MS validation of P12 and biotinylated P12-derived constructs. The intended sequence and final design of each construct are presented together with the theoretical and experimentally determined molecular masses. Sequence extensions and PEG2 linkers are shown in red, whereas biotin modifications are shown in green. Constructs for which the LC–MS-derived mass was consistent with the expected product were considered confirmed and retained for subsequent experiments; constructs yielding an inconsistent mass were not confirmed and were discarded. Molecular masses are expressed in daltons (Da).

Supplementary Table S3.

Batch Number	Total Mass (mg)	Yield (mg·L ¹)
Batch 1	21.5	2.15
Batch 2	14	1.75
Batch 3	17	1.7
Batch 4	13.5	1.68
Batch 5	24.7	2.05
Batch 6	18.4	1.84
Batch 7	23.4	1.95
Batch 8	17.8	1.78
Batch 9	19.2	1.92

Supplementary Table S3. Production yield of independent recombinant tau(297–391) purification batches. Total mass corresponds to the dry mass of tau(297–391) recovered after lyophilization. Protein yield was calculated by normalizing the recovered mass to the initial volume of bacterial culture and is expressed in $mg \cdot L^{-1}$.

8.3. Supplementary Notes

Supplementary Note S1.

Fusion protein (6xHis-SUMO-tau(297-391)):

**MGHHHHHHMSDSEVNQEAKPEVKPEVKPETHINLKVSDGSSEIFFKIKKTTPLRRLMEAFAKRQGKEMDSL
RFLYDGIRIQADQTPEDLDMEDNDIIEAHREQIGG**IKHVPGGGSVQIVYKPVDLSKVTSKCGSLGNIHHKPGGGQ
VEVKSEKLDFKDRVQSKIGSLDNITHVPGGGNKKIETHKLTFRENAKAKTDHGAE

Sequence length:	201
Molecular weight:	22420.32 (Da)
Theoretical pI:	7.27
Ext. coefficient:	2980 ($M^{-1}\cdot cm^{-1}$)

Cleaved tau(297-391):

IKHVPGGGSVQIVYKPVDLSKVTSKCGSLGNIHHKPGGGQVEVKSEKLDFKDRVQSKIGSLDNITHVPGGGNKKIET
HKLTFRENAKAKTDHGAE

Sequence length:	95
Molecular weight:	10165.57 (Da)
Theoretical pI:	9.59
Ext. coefficient:	1490 ($M^{-1}\cdot cm^{-1}$)

Supplementary Note S1. Amino acid sequences and predicted physicochemical properties of the 6×His–SUMO–tau(297–391) fusion protein and cleaved tau(297–391). The 6×His tag and SUMO sequences are shown in green, whereas tau(297–391) is shown in black. Sequence length, molecular weight, theoretical isoelectric point and extinction coefficients at 280 nm were calculated using ExPASy ProtParam. The asterisk denotes the stop codon.

Supplementary Note S2

Calculation parameters. $C_{\mathrm{P}} = 10$ mM; $[\mathrm{Mg}^{2+}]_0 = 0.200$ M; pH = 7.4; $\mathrm{p}K_{a,1} = 2.2$, $\mathrm{p}K_{a,2} = 7.2$, and $\mathrm{p}K_{a,3} = 12.3$.

1. Phosphate speciation at pH 7.4

For phosphoric acid, the fractional population N_i of each protonation state is defined by

$$N_0 = \frac{[\mathrm{H}^+]^3}{\Sigma}, \quad N_{-1} = \frac{[\mathrm{H}^+]^2 K_1}{\Sigma}, \quad N_{-2} = \frac{[\mathrm{H}^+] K_1 K_2}{\Sigma}, \quad N_{-3} = \frac{K_1 K_2 K_3}{\Sigma}, \tag{1}$$

where

$$\Sigma = [\mathrm{H}^+]^3 + [\mathrm{H}^+]^2 K_1 + [\mathrm{H}^+] K_1 K_2 + K_1 K_2 K_3, \qquad [\mathrm{H}^+] = 10^{-7.4},$$

and $N_0 + N_{-1} + N_{-2} + N_{-3} = 1$ (100%). At $C_{\mathrm{P}} = 10$ mM, the calculated concentrations are:

Species	Calculation	Concentration	Eq.
$\mathrm{H_3PO_4}$	$\frac{(10^{-7.4})^3}{\Sigma}$ (10 mM)	**24 nM**	(2)
$\mathrm{H_2PO_4^-}$	$\frac{(10^{-7.4})^2\, 10^{-2.2}}{\Sigma}$ (10 mM)	**3.9 mM**	(3)
$\mathrm{HPO_4^{2-}}$	$\frac{10^{-7.4}\, 10^{-2.2}\, 10^{-7.2}}{\Sigma}$ (10 mM)	**6.1 mM**	(4)
$\mathrm{PO_4^{3-}}$	$\frac{10^{-2.2}\, 10^{-7.2}\, 10^{-12.3}}{\Sigma}$ (10 mM)	**77 nM**	(5)

The principal aqueous phosphate equilibrium at pH 7.4 is therefore

$$\mathrm{H_2PO_4^- + H_2O \rightleftharpoons HPO_4^{2-} + H_3O^+}. \tag{6}$$

---

2. Solubility equilibria following $MgCl_2$ addition

The solubility products used in the calculation were $K_{\mathrm{sp}} = 1.6 \times 10^{-6}$ for $\mathrm{MgHPO_4 \cdot 3H_2O}$ and $K_{\mathrm{sp}} = 6.3 \times 10^{-26}$ for $\mathrm{Mg_3(PO_4)_2 \cdot 8H_2O}$. At $[\mathrm{Mg}^{2+}] = 0.200$ M and pH 7.4, the corresponding ionic products are

$$Q_{\mathrm{MgHPO_4}} = [\mathrm{Mg}^{2+}][\mathrm{HPO_4^{2-}}] = 0.200(6.1 \times 10^{-3}) = \mathbf{1.23 \times 10^{-3}} > 1.6 \times 10^{-6}, \tag{7}$$

$$Q_{\mathrm{Mg_3(PO_4)_2}} = [\mathrm{Mg}^{2+}]^3[\mathrm{PO_4^{3-}}]^2 = 0.200^3(7.7 \times 10^{-8})^2 = \mathbf{4.77 \times 10^{-17}} > 6.3 \times 10^{-26}. \tag{8}$$

Both ionic products exceed their respective K_{sp} values. Because phosphate (10 mM) is limiting relative to Mg^{2+} (200 mM), the calculation predicts that phosphate precipitates predominantly as $\mathrm{MgHPO_4 \cdot 3H_2O}$. Removal of $\mathrm{HPO_4^{2-}}$ shifts equilibrium (6) to the right, releasing $\mathrm{H_3O^+}$ and acidifying the solution.

3. Estimated extent of phosphate precipitation

At a final pH of 7.4, let x denote the phosphate concentration precipitated as $\mathrm{MgHPO_4 \cdot 3H_2O}$, with all concentrations expressed in $\mathrm{mol\,L^{-1}}$:

$$K_{\mathrm{sp}} = 10^{-5.8} = [\mathrm{Mg}^{2+}][\mathrm{HPO_4^{2-}}] = [\mathrm{Mg}^{2+}]\, C_{\mathrm{P}}\, N_{-2},$$

$$(0.200 - x)(0.010 - x)\left(\frac{10^{-7.4}\, 10^{-2.2}\, 10^{-7.2}}{\Sigma}\right) = 10^{-5.8}. \tag{9}$$

$$x = 9.99 \times 10^{-3}\ \mathrm{M} = 9.99\ \mathrm{mM}$$

The calculation predicts precipitation of 99.9% of the initial 10 mM phosphate.

Supplementary Note S2. Theoretical calculation of phosphate speciation and Mg^{2+}-dependent precipitation. Phosphate speciation was calculated for a 10 mM phosphate buffer at pH 7.4 using pK_a values of 2.2, 7.2, and 12.3. Under these conditions, $H_2PO_4^-$ and HPO_4^{2-} were the predominant soluble species, with calculated concentrations of 3.9 and 6.1 mM, respectively. Following the addition of 200 mM $MgCl_2$, the calculated ionic products exceeded the reported solubility products of $MgHPO_4 \cdot 3H_2O$ and $Mg_3(PO_4)_2 \cdot 8H_2O$. Solving the $MgHPO_4$ solubility equilibrium predicted the precipitation of approximately 9.99 mM phosphate, corresponding to 99.9% of the initial phosphate concentration. The associated shift in phosphate equilibrium would release protons and could therefore contribute to acidification of the reaction mixture. The equilibrium framework, constants, and numerical values presented here are based on the calculations reported in the Supporting Information of Duan et al. [62]. The equations and accompanying explanations were reformatted for presentation in the present thesis.